ABSTRACT

Title: A CERAMIC DAMAGE MODEL FOR ANALYSES OF
            MULTI-LAYERED CERAMIC-CORE SANDWICH
            PANELS UNDER BLAST WAVE PRESSURE
            LOADING

            Keejoo Lee, Ph.D., 2005

Directed By: Professor Sung W. Lee,
               Department of Aerospace Engineering

A damage model for ceramic materials is developed and incorporated into the geometrically nonlinear solid shell element formulation for dynamic analyses of multi-layered ceramic armor panels under blast wave pressure loading. The damage model takes into account material behaviors observed from multi-axial dynamic tests on Aluminum Nitride (AlN) ceramic. The ceramic fails in a brittle or gradual fashion, depending upon the hydrostatic pressure and applied strain-rate. In the model, the gradual failure is represented by two states: the initial and final failure states. These states are described by two separate failure surfaces that are pressure-dependent and strain-rate-dependent. A scalar damage parameter is defined via using the two failure surfaces, based on the assumption that the local stress state determines material damage and its level. In addition, the damage model accounts for the effect of existing material damage on the new damage.

The multi-layered armor panel of interest is comprised of an AlN-core sandwich with unidirectional composite skins and a woven composite back-plate. To accommodate the material damage effect of composite layers, a composite failure model in the open literature is adopted and modified into two separate failure models to address different failure mechanisms of the unidirectional and woven composites. In addition, the effect of strain-rates on the material strengths is incorporated into the composite failure models.

For finite element modeling, multiple eighteen-node elements are used in the thickness direction to properly describe mechanics of the multi-layered panel. Dynamic analyses of a multi-layered armor panel are conducted under blast wave pressure loadings. The resulting dynamic responses of the panel demonstrate that dynamic analyses that do not take into account material damage and failure significantly under-predict the peak displacement. The under-prediction becomes more pronounced as the blast load level increases. Numerical analyses also indicate that the multi-layered armor design, while tailored for penetration resistance, performs poorly against blast shock wave. An alternative design is proposed and its performance is compared with the original design. Computational modeling of the fundamental material behaviors of ceramics would help expanding the use of ceramics to other structural applications, via enabling designers to efficiently explore design options.

A CERAMIC DAMAGE MODEL FOR ANALYSES OF MULTI-LAYERED
CERAMIC-CORE SANDWICH PANELS UNDER BLAST WAVE PRESSURE
LOADING

By

Keejoo Lee

Dissertation submitted to the Faculty of the Graduate School of the
University of Maryland, College Park, in partial fulfillment
of the requirements for the degree of
Doctor of Philosophy
2005

Advisory Committee:
Professor Sung W. Lee, Chair
Professor Norman M. Wereley
Professor Alison B. Flatau
Professor Amr M. Baz
Professor Abhijit Dasgupta

Dedication

To my wife, Joohee Yum, for her love and support.

Also to my parents, Soonihl Lee and Heesook Kim, for their endless encouragement.

Acknowledgements

I would like to express my gratitude and appreciation to my advisor, Professor Sung W. Lee for his guidance and mentorship throughout my graduate study. I would also like to thank Professors Baz, Dasgupta, Flatau and Wereley for reading the dissertation and making positive suggestions.

I give my special thanks to Dr. Ki C. Kim at the Army Research Laboratory for introducing this interesting subject.

My thanks must go to Dr. Hun Park and Dr. Jihan Kim for the invaluable technical discussions I had with them. I am very grateful to my office mate, Suzanne Ruddy, for her hospitality.

I am also very grateful to fellow Ph.D. students, Suneel Sheikh and Falcon Rankins whose friendship, knowledge and hospitability have spported, enlightened and entertained me.

Table of Contents

List of Tables

List of Figures

xii

Nomenclature

Vectors and matrices

$\mathbf{a}_3$ — Unit vector through thickness

$\boldsymbol{\alpha}$ — Assumed strain coefficient vector

$\delta\boldsymbol{\alpha}$ — Virtual assumed strain coefficient vector

$\mathbf{B}(\xi,\eta,\varsigma)$ — Matrix that relates $\mathbf{q}_e$ to linear part of $\overline{\boldsymbol{\varepsilon}}$

$\mathbf{C}_{deg}$ — Degraded stiffness matrix for composite materials

$\mathbf{C}_e$ — Elastic stiffness matrix for intact materials

$\overline{\boldsymbol{\varepsilon}}$ — Displacement-dependent engineering strain vector

$\overline{\mathbf{e}}$ — Linear displacement-dependent strain vector

$\Delta\overline{\mathbf{e}}$ — Incremental linear displacement-dependent strain vector

$\delta\overline{\mathbf{e}}$ — Virtual strain vector for linear part of displacement-dependent strain

$\delta\overline{\boldsymbol{\varepsilon}}$ — Virtual displacement-dependent engineering strain vector

$\boldsymbol{\varepsilon}$ — Displacement-independent assumed strain vector

$\Delta\boldsymbol{\varepsilon}$ — Incremental form of assumed strain vector

$\delta\boldsymbol{\varepsilon}$ — Virtual displacement-independent assumed strain vector

$\mathbf{f}(\mathbf{q})$ — Vector of nonlinear functions that represent internal forces corresponding to $\mathbf{q}$

$\mathbf{K}$ — Global stiffness matrix

$\mathbf{K}_e$ — Element stiffness matrix

$\mathbf{K}_e^{18}$ — Element stiffness matrix for 18-node solid shell element

$\mathbf{M}$ — Global mass matrix

$\mathbf{M}_e$ — Element mass matrix

$\mathbf{N}(\xi,\eta,\varsigma)$ — Matrix of shape functions

$\mathbf{P}(\xi,\eta,\varsigma)$ — Matrix of assumed strain shape functions

$\mathbf{Q}$ — Global applied load vector

$\mathbf{q}$ — Global degree of freedom vector

$\dot{\mathbf{q}}$	Global velocity vector
$\ddot{\mathbf{q}}$	Global acceleration vector
$\delta\mathbf{q}$	Virtual global degree of freedom vector
$\mathbf{q}_e$	Element degree of freedom vector for 9-node solid shell element
$\mathbf{q}_n$	Displacement vector at $t = t_n$
$\dot{\mathbf{q}}_n$	Velocity vector at $t = t_n$
$\ddot{\mathbf{q}}_n$	Acceleration vector at $t = t_n$
$\mathbf{q}_e^{18}$	Element degree of freedom vector for 18-node solid shell element
$\boldsymbol{\sigma}$	Stress vector
$\Delta\boldsymbol{\sigma}$	Incremental stress vector
$\mathbf{S}$	Elastic compliant matrix
$\mathbf{T}$	Transformation matrix from $\mathbf{q}_e^{18}$ to $\mathbf{q}_e$
$\mathbf{u}$	Displacement vector in a solid
$\delta\mathbf{u}$	Virtual displacement vector in a solid
$\ddot{\mathbf{u}}$	Acceleration vector in a solid
$\mathbf{u}_{bot}$	Displacement vector in the bottom surface of a solid
$\mathbf{u}_{top}$	Displacement vector in the top surface of a solid
$\mathbf{u}_o$	Displacement vector in the shell mid-surface
$\mathbf{u}_z$	Displacement vector in the $\mathbf{a}_3$ direction
$\Delta\mathbf{u}$	Displacement vector in an incremental form
$^{(i)}\mathbf{u}$	Displacement vector at the known state
$\mathbf{x}$	Position vector in a solid
$\mathbf{x}_{bot}$	Position vector in the bottom surface of a solid
$\mathbf{x}_{top}$	Position vector in the top surface of a solid
$\mathbf{x}_o$	Position vector in the shell mid-surface

Scalars

A	Material constant for transverse strength vs. strain-rate model
$a_1,\ldots,a_9$	Material constants for the general yield function
α	Material parameter, slope for the shear strength vs. pressure curve
α_p	Exponential coefficient for Friedlander pressure function
B_1	Material constant for the coefficient β
B_2	Exponential constant for the coefficient β
β	Shear strength at zero hydrostatic pressure
β_{SC}	Shear correction factor
D	Scalar quantity that stands for degree of damage
d	Distance to the current stress point in the principal stress plane for ceramic damage model
D_T	Damage parameter for tensile failure mode
D_T^*	Trial damage parameter for tensile failure mode
D_C	Damage parameter for compressive failure mode
D_C^*	Trial damage parameter for compressive failure mode
D_C^o	Damage parameter for compressive failure mode at the previous equilibrium
d_i	Distance to the initial failure surface for ceramic damage model
d_c	Distance to the final failure surface for ceramic damage model
e	Failure index for composite failure criteria
$^{(i)}\bar{\varepsilon}_{ij}$	Green strain tensor at the known state
$\Delta\bar{e}_{ij}$	Low-order Green strain tensor in an incremental form
$\dot{\varepsilon}$	Strain rate in the loading direction
$\dot{\varepsilon}_{ref}$	Reference strain-rate in the loading direction
$\bar{\varepsilon}_{ij}$	Green strain tensor

E_1, E_2, E_3	Elastic moduli for orthotropic materials
E_f	Longitudinal modulus of fibers
P_o	Lateral confining pressure for the triaxial test
P	Hydrostatic pressure
P_{th}	Threshold pressure for ceramic damage model
P_{trial}	Trial pressure to determine the uniaxial compressive strength
$f(\boldsymbol{\sigma})$	Pressure-dependent initial failure surface function
$f_2(\boldsymbol{\sigma})$	Pressure-independent initial failure surface function
G_{12}, G_{23}, G_{31}	Shear moduli for orthotropic materials
$g(\boldsymbol{\sigma})$	Pressure-dependent final failure surface function
$g_2(\boldsymbol{\sigma})$	Pressure-independent final failure surface function
$\Delta \bar{h}_{ij}$	High-order Green strain tensor in an incremental form
I_1	First invariant of the stress
J_2	Second invariant of the deviatoric stress
k	Material constant for Von Mises criterion
k_i	Material constant for pressure-independent initial failure surface
k_o	Material constant for pressure-independent final failure surface
L	Length for flat panel
L_{arch}	Arch length for curved panel
$N_i(\xi, \eta)$	Shape function corresponding to i-th node
v_{12}, v_{23}, v_{31}	Major Poisson's ratio for orthotropic materials
v_f	Fiber volume fraction
P_{br}	Brittle pressure that determines the failure modes
$P(t)$	Time-varying Friedlander pressure function
P_m	Initial magnitude of pressure wave at $t = 0$ for Friedlander function
ρ	Material density

$\sigma_I, \sigma_{II}, \sigma_{III}$	Principal stresses
SC_{12}	In-plane shear strength of unidirectional ply
t	Thickness of a solid
t_p	Time when pressure completely dies out
Δt	Incremental time step
$|\tau|$	Shear strength for ceramics
τ_f	Limit shear strength beyond the threshold pressure
X	Uniaxial tensile strength for ceramics
X_t	Tensile strength of unidirectional ply in the fiber direction
X_c	Compressive strength of unidirectional ply in the fiber direction
ξ, η, ς	Parental coordinates in solid shell element
Y	Uniaxial compressive strength for ceramics
Y_t	Tensile strength of unidirectional ply in the transverse direction
Y_c	Compressive strength of unidirectional ply in the transverse direction or Compressive strength in the axial direction of the triaxial test
Y_{QS}	Quasi-static uniaxial compressive strength
δW	Virtual work due to the applied load

Chapter 1 Introduction

Ceramics have been used as armor materials because of their high effectiveness in absorbing kinetic energy under extreme loading conditions such as ballistic impacts. This is possible because they have very high compressive strengths. Ceramics exhibit significant compressive strength even when pulverized by a ballistic projectile. In addition, ceramic armors are lightweight, compared to conventional steel armors that are much heavier and more cumbersome. However, the brittleness of ceramics under tension has limited their use to applications that require little deformation such as the torso of war fighters.

1.1 *Motivation*

Computational modeling of the fundamental material behavior of ceramics would help expanding the use of ceramics to other structural applications, via enabling designers to efficiently explore many design options and reducing the time and cost of development.

One of the popular armor designs is to use a ceramic layer in multi-layered composite structures. For the multi-layered armor design, a ceramic layer is often

sandwiched by composite skins that provide the confinement over damaged ceramic fragments, and the ceramic-core sandwich armor is bonded to a composite back plate that provides structural integrity. Multi-layered ceramic armor designs are attractive because of their excellent performance against impact loadings. However, one of the important design considerations, survivability under blast wave loading caused by nearby explosions, has been often neglected in their design process. In contrast to the local deformation around the impact site under the impact loading, the multi-layered armor may go through a large deflection at the structural level under the time-dependent pressure loading. To investigate the structural response of the multi-layered armors undergoing a large deflection at a short time-span, a dynamic analysis, combined with the geometrically nonlinear formulation, is required.

As the multi-layered armors undergo large deformation, material damages and failures may affect their structural response and survivability. Unidirectional and woven composites used for skins and the back plate may experience material failures such as matrix crackings, fiber breakages and matrix/fiber shear failures and out-of-plane delaminations at local points. The material failure grows over the entire composite layer, and progressively degrades stiffness and strength of the composite layers. The ceramic layer may also go through material damages at local points. An analytical method to assess the effect of material damages on the structural behavior of the multi-layered armor, based on the appropriately defined failure criteria, is required. Also, an analytical method to degrade material stiffness corresponding to the detected material damages is needed. To build a design tool for multi-layered

2

armors, the analytical method that can efficiently represent the material damages effect on the structural response is required both for composite and ceramic layers.

For structures subjected to extreme conditions such as blasts, the effect of the high strain-rate on the material behavior is of great concern. Experiments indicate that material strengths increase in general as the applied loading rate goes up, for composites and ceramics. Accordingly, the effect of the strain-rate on the material strengths must be adequately incorporated into the analytical methods for the damage and failure assessment.

The previous works on the damage and failure models for ceramic and composite structures are briefly reviewed in the following section.

1.2 *Review of Previous works*

1.2.1 Ceramic Damage Models

Extensive, experimental researches on material properties of ceramics under high strain-rate environments have been conducted, primarily to evaluate the penetration resistance of ceramic armors. Most of the experiments were uniaxial such as bar impact (uniaxial stress) and plate impact (uniaxial strain) tests. Concurrently, numerical models to describe the damage and failure of ceramic specimen have been developed to simulate the impact experiments and penetration tests. Damage models for ceramics in the open literature can be classified into two groups: micromechanical models and phenomenological models.

For the micromechanical models, the damage of ceramic materials is estimated as microcracks nucleate and grow under multi-axial loading conditions.

Taylor, Chen and Kuszmaul (TCK) [1] developed a damage model for rocks exhibiting strain-rate-dependent inelastic behavior under tension via combining the theory of fracture mechanics for individual microcrack growth with statistical evaluation of microcrack distribution. A single scalar damage parameter that represents microcrack distribution within the material was introduced. The damage accumulation resulted in the degradation of the material moduli and the decrease of the material stiffness. However, in the TCK model, the compressive strength was assumed constant, independent of damage, pressure and strain-rate. Rajendran and Kroupa [2] modified the TCK model via adding the effect of the strain-rate and damage-dependent compressive strength, and conducted simulation of plate impact tests. They also showed that for brittle solids, plastic deformation is minimal and the strains are not accumulated upon unloading. However, this model was only useful to describe the tensile dominant damages under extremely high pressure (> 10 GPa). Addessio and Johnson [3] developed a microphysically based material model for the dynamic response of brittle materials that described crack opening under tension and crack sliding under compression. This model was validated for uni-axial strain cases only. Rajendran and Grove [4,5] introduced a new damage model that incorporated the effects of different damage processes under tension and compression using microcracking and plasticity, and successfully reproduced the measurements from shock wave tests. However, model parameters were indirectly determined via trial-and-error simulations to match several test results. Espinosa [6] developed a multi-plane microcraking model that allowed for anisotropic damage, and Zavattieri, Raghuram and Espinosa [7] extended the model into a multi-body contact model for

4

analyses of ceramic microstructures. In their model, microcracking at grain boundaries and subsequent opening and closing of the microcracks were simulated. In general, the micromechanical models reproduce measurements obtained from impact experiments on specimen reasonably well. However, the micromechanical models must assume randomly distributed initial cracks and their sizes, and they are computationally very expensive, generally not applicable to large-scale problems.

For the phenomenological models, an explicit function of time and effective stress is used to predict damage propagation, via calibrating coefficients of the function with other measured quantities. Johnson and Holmquist [8] developed the most popular ceramic damage models (JH-1 model). They improved the model (JH-2) and applied it to Boron Carbide ceramic [9]. Their models used two-surface strengths curves to model intact and completely failed states. The JH-2 model has been applied to several ceramics. Holmquist, Templeton and Bishnoi [10] applied the JH-2 model to Aluminum Nitride. Holmquist and Johnson [11] applied the JH-2 model to Silicon Carbide ceramic. However, the pressure-dependent strength curves were constructed based on bar and impact tests that were carried out for varieties of configurations, indicating that strength change may be caused by other factors such as geometry and boundary conditions. Fahrenthold [12] developed a continuum model based on the idea of complimentary energy density that used a second-order tensor to represent anisotropic damage. His model was used to calculate the depth of penetration for steel plates. Simha, Bless and Bedford [13,14] developed a damage model similar to Fahrenthold's model, inferred from bar and plate impact tests on AD-99.5 alumina. In their model, a stress-based damage evolution law was introduced, and it was assumed

that ceramics comminute at the Hugoniot Elastic Limit (HEL). The model was successfully used to predict the depth of penetration. These phenomenological models reported in the literature predominantly focused on predicting the material behavior of ceramic armors and their penetration resistance in the area of the impact site, but these models were often only applicable to the specific experiments they were based on [15]. The calibrated coefficients become invalid if any configuration changes such as geometry and boundary conditions are made. For example, uniaxial strain tests and uniaxial stress tests were dominantly used to calibrate the phenomenological models, but the models were used to predict the depth of penetration, which is a complex three-dimensional problem. Accordingly, there is a need for a constitutive model that can describe dynamic failure mechanisms of ceramics regardless of their configurations and loading rates.

Heard and Cline [16] performed tri-axial tests to quantify the pressure-dependency of BeO, Al_2O_3 and AlN ceramics. Their study was limited to quasi-static cases. Lankford [17] investigated the dynamic behavior of ceramics under high strain-rate condition. Lankford [18] later used the Split Hopkinson pressure bar under the hydrostatic confining pressure to quantify the failure behavior of ceramics under multi-axial compression. Recently, Chen [19] has developed a new experimental technique to apply the static and dynamic tri-axial load to a cylindrical specimen. Chen and Ravichandran [20,21] applied the experimental technique to Aluminum Nitride and Macro ceramics. In their study, the specimen was laterally confined via using a shrink-fit metal sleeve. The tri-axial tests indicated that the mechanical behavior of ceramics is pressure-dependent and strain rate-dependent. Sarva [22]

6

performed the tri-axial tests on SiC ceramic and showed that the compressive strength is pressure-dependent and strain rate-dependent. He also demonstrated that the membrane restraints on Al_2O_3 ceramic can significantly improve the ballistic efficiency. The recent advances in multi-axial experimental techniques may provide a viable alternative source for the ceramic damage model.

According to the above review of the previous damage models, the main characteristics of ceramics are pressure-dependent and strain-rate-dependent behaviors under compression. Many damage models have been developed to capture the characteristics of ceramics based on the uniaxial tests. However, their material parameters are sensitive to test configurations or the models are computationally very inefficient. Little work has been reported on the ceramic damage model that is based on the tri-axial experimental observation. Accordingly, there is a strong need for a ceramic damage model that reflects the multi-axial phenomena for analyses of ceramic structures under dynamic loading.

1.2.2 Composite Failure Models

There have been considerable amount of researches regarding the integrity of composite structures. Park [23] had a good and selective review on the subject. Based on the experimental observations and theoretical models in the literature, he has developed a comprehensive analytical methodology for composite structures under blast pressure loading, which was validated with experimental data. In his study, the viscoplastic formulation was incorporated into the geometrically nonlinear solid shell element formulation to account for the strain-rate effect on constitutive equations. In

addition, the effect of strain-rate on the material strengths was considered. However, it appears that the viscoplastic effect on the constitutive equations was not as significant as expected. Also, a composite failure model was developed to accommodate the progressive failure effect of woven composites. However, the failure model was based on the failure criteria for the unidirectional ply. Accordingly, there is a need for a separate failure model for woven composites.

1.2.3 Panels Subjected to Blast Shock Wave

Survivability under blast loading is one of the important considerations in armor designs, irrespective of their constituent materials. Slater [24] carried out a series of shock-tube tests on clamped glass fiber reinforced plastic composite panels for naval ship structures. In his study, it was shown that the clamping of the plate edge was necessary to obtain good blast resistance via substantially reducing the deflection compared to the simply-supported conditions. Yen, Cassin, Patterson and Triplett [25] developed composite failure criteria for dynamic analysis of composite structures subjected to mine blast loading conditions. The failure criteria were incorporated into an explicit dynamic analysis code (LS-DYNA [26]) to predict the progressive delamination in a composite sandwich panels. However, this study was limited to the unidirectional composite, and the predicted delamination was only validated in a qualitative manner. Meunier and Shenoi [27] developed an analytical method based on high-order shear deformation theory to investigate the dynamic behavior of PVC foam-core composite sandwich plates. In their study, damping of the sandwich plates was modeled using the viscoelastic properties of the PVC foam and

8

its temperature or frequency dependency. No work has been reported on the dynamic behavior of multi-layered ceramic-core composite sandwich panels under blast wave pressure loading. Accordingly, there is a need for an analytical methodology to determine dynamic response and integrity of the multi-layered ceramic-core sandwich panels.

1.3 *Objectives and Scopes*

The objective of this study has been to develop an analytical methodology that can efficiently determine the dynamic response of multi-layered ceramic-core sandwich panels under the dynamic loading such as blast shock wave, via accounting for the complex material damage effect. This study focuses on the development of a new ceramic damage model based on the multi-axial tests, and introduces separate failure models for unidirectional and woven composites, via modifying the existing models.

A constitutive model for Aluminum Nitride (AlN) ceramic is developed to represent the pressure-dependent and strain-rate-dependent behavior under dynamic loading. Based on the observations made from multi-axial dynamic tests on AlN, two failure surfaces that account for the brittle and gradual failures are proposed. The failure surfaces also represent the strain-rate-dependent behavior. A damage model is built out of these two failure surfaces under the assumption that the stress state dictates material damage and its level. In addition, the effect of the existing damage on the new damage is taken into account.

Two separate material models for the unidirectional and the woven composites are proposed to accommodate the different failure mechanisms. For the unidirectional composites, in-plane failure criteria for matrix cracking, fiber breakage and matrix/fiber shear failures, introduced by Hashin [28-29] and Chang et al [30-32], and later modified by Park [23] are adopted and used with modifications. For the woven composites, the unidirectional failure criteria are modified to take into account different failure mechanisms such as fiber breakages in the two perpendicular fiber directions. In the finite element analysis, material failure check is performed at every equilibrium state. For composites, the failure check is carried out at every integration point of elements throughout layers of laminates. Once failures are detected, the elastic stiffness of the virgin material is degraded into a reduced value. The stiffness reduction used by Hashin [33] and Padhi, Shenoi, Moy and Hawkins [34] is modified to address different failure modes in the present study.

The developed ceramic damage model and composite failure models are incorporated into the geometrically nonlinear assumed strain solid shell element formulation for dynamic analyses of multi-layered ceramic armor panels under the blast wave pressure loading conditions. To properly model the effect of multi-layered panels, multiples elements through the thickness are required. For this purpose, an eighteen-node version (SHELL18) of the assumed strain solid shell elements, which is equivalent to the nine-node version (SHELL9), is chosen. An eighteen-node element has nine nodes on the top and bottom surfaces and individual node has three translational degrees of freedom only, which facilitates stacking of elements through the thickness.

For structures designed to endure extreme conditions such as blasts, the effect of the high strain-rate on the material behavior is of great concern. Experiments indicate that material strengths increase in general as the applied loading rate goes up. Accordingly, the effect of the strain-rate on the material strengths is incorporated into the present failure models. The viscoplastic effect on the constitutive equations is ignored in the present study.

1.4 *Brief Descriptions on the Following Chapters*

In Chapter 2, a damage model for Aluminum Nitride (AlN) ceramic is developed based on observations from multi-axial static and dynamic experiments. In Chapter 3, two separate failure models for unidirectional and woven composites are introduced. Material degradation models are proposed to represent the progressive nature of the composite damage and failure. In Chapter 4, the nonlinear assumed strain solid shell element formulation for dynamic problems is described. In Chapter 5, various numerical tests are conducted to evaluate the effectiveness of the damage and failure models, introduced in Chapter 2 and Chapter 3, in describing the structural behavior of ceramic and composite panels under dynamic loading conditions. In addition, the structural behavior of a multi-layered composite armor with a ceramic layer under the blast wave pressure loading is investigated via conducting the finite element analysis. Subsequently, a modified armor design is proposed, and its structural performance is compared with that of the original design. In Chapter 6, conclusions are drawn and recommendations for future work are provided.

Chapter 2 Ceramic Damage Model

This chapter describes a damage model for ceramics that is consistent with pressure-dependent and strain-rate-dependent behaviors observed from multi-axial tests on Aluminum Nitride (AlN) ceramic. A couple of failure surfaces representing the experimentally observed behavior are introduced to describe the material damage. In addition, the damage model accounts for the effect of the existing material damage on the new damage. The effect of stress-induced damage appears as degraded material stiffness in the constitutive equations.

2.1 *Experimentally Observed Behaviors of Ceramics*

Ceramics show different material behaviors under tensile and compressive stresses. Under tension, experiments indicate that ceramics exhibit a linear elastic behavior and a sudden rupture [35]. Under compression, however, their failure tends to be more gradual and the initial failure does not mean a complete loss of the load carrying capability. Under certain conditions, ceramics fail in a brittle manner even under compression. For example, it is observed that in the uniaxial compression test, ceramics typically fail in a brittle fashion.

More precisely, material behaviors of ceramic materials are dependent on the hydrostatic pressure. As the pressure increases, the frictional force on the pressure-applied surface increases, hindering the grain boundaries from slipping between ceramic ingredients. As a result, the shear strength of the ceramic materials significantly increases. Accordingly, the shear strength has been often used as the only decisive measure of the failure in pressure-sensitive materials [36].

To investigate the effect of the confining pressure on the material behavior, triaxial compression tests can be used. Figure 2-1 shows a schematic illustration of the stress state in the triaxial test. The axial compressive strength is measured while a constant, confining pressure is applied in the lateral direction. For example, Chen [19] investigated the effect of the confining pressure on the failure mechanism of Aluminum Nitride (AlN) by conducting triaxial compressive tests under the quasi-static ($\dot{\varepsilon} = 4 \times 10^{-4}$ (1/sec)) and dynamic loading ($\dot{\varepsilon} = 5 \times 10^{2}$ (1/sec)) conditions. Table 1 lists the mechanical properties of AlN. The dynamic test was carried out using a modified Split-Hopkinson Pressure Bar while the static test was carried out on the multipurpose testing system. In his study, a special experimental technique was developed to achieve a moderate level of the confining pressure. As shown in Figure 2-1, an AlN specimen is inserted into a hollow cylindrical sleeve that has a slightly smaller diameter via thermally expanding the sleeve. As the temperature cools down, the sleeve pressurizes the specimen. The magnitude of the confining pressure is controlled via choosing different materials and changing the sleeve size. Figure 2-2 shows the compressive strength vs. the lateral pressure under the quasi-static and

dynamic loading conditions. In Figure 2-2, the straight lines are the least-square fits

of experimental data. It is observed that in the presence of lateral confinement, the

compressive strength of ceramics significantly increases irrespective of the applied

strain-rate.

For pressure-sensitive materials, the shear strength depends on the hydrostatic

pressure. One can obtain the shear strength, $|\tau|$ and the corresponding hydrostatic

pressure, P from the triaxial test data as

$$
\begin{aligned}
|\tau| &= (Y_c - P_o)/2 \\
P &= (Y_c + 2P_o)/3
\end{aligned}
\tag{2.1}
$$

where Y_c is the compressive strength in the axial direction and P_o is the lateral

confining pressure in the other two directions. In the triaxial test, the axial strength Y_c

is measured at a given strain-rate with increasing the lateral pressure P_o. Figure 2-3

shows the shear strength vs. the hydrostatic pressure for the quasi-static and dynamic

loading conditions. According to the least-square fits shown as lines in Figure 2-3, it

appears that the shear strength is linearly proportional to the pressure under the static

loading condition. The linear dependency has been observed in other pressure-

dependent materials such as rocks and concretes [37]. In addition, it appears that the

shear strength is also linearly proportional to the pressure under the dynamic loading

condition. Accordingly, the shear strength is written as a linear function of the

hydrostatic pressure on the shearing plane for both loading conditions as

$$|\tau| = \alpha P + \beta \qquad (2.2)$$

where α, β are material parameters determined via applying the least-square method to the measured data in Figure 2-3. Note that these material parameters depend on the applied strain-rates. In sum, the triaxial tests demonstrate that the shear strength increases as the hydrostatic pressure increases.

However, the increase in the shear strength is not unbounded according to other impact tests. The above triaxial tests are conducted only up to a moderate level of the confining pressure because of difficulties in experimental implementations. Other test methods such as the bar impact test and the plate impact test have been prevalently used at the higher level of the pressure in order to investigate the effect of the pressure on the material strengths [38,39]. Figure 2-4 shows the shear strength vs. the hydrostatic pressure for the triaxial tests and other impact tests together. According to the strength curve, the shear strength of AlN gradually becomes insensitive to the hydrostatic pressure beyond a limit pressure, at which the ceramic ingredients are locked to each other and the friction force effect diminishes. In this study, the gradual transition [21] from pressure-dependent to pressure-independent behavior is approximated as two distinct states, primarily due to lack of experiments in the transitional pressure range. The limit pressure is called the threshold pressure. The shear strength is expressed under the moderate level of pressure as

$$|\tau| = \alpha P + \beta, \text{ for } P < P_{th} \qquad (2.3)$$

where P_{th} is the threshold pressure, below which ceramics show pressure-dependent behaviors. Note that the material parameters α, β are defined below the threshold pressure only. The shear strength becomes pressure independent as

$$|\tau| = \tau_f, \qquad \text{for } P \geq P_{th} \qquad (2.4)$$

where τ_f is a constant, limit shear strength beyond the threshold pressure. The threshold pressure is calculated via solving equations (2.3) and (2.4) as

$$P_{th} = \frac{\tau_f - \beta}{\alpha} \qquad (2.5)$$

Not only is the material behavior of ceramics dependent on the hydrostatic pressure, but it is also affected by the applied strain-rate. For example, the shear strength in Figure 2-3 is dependent on the applied strain-rate as well as the hydrostatic pressure. For Aluminum Nitride, the slope α remains approximately constant while the coefficient β changes as the applied strain-rate increases [21]. To take into account the strain-rate effect, the coefficient β can be assumed as an exponential function of the strain-rate as

$$\beta(\dot{\varepsilon}) = \tau_f - B_1 e^{-B_2 \dot{\varepsilon}} \qquad (2.6)$$

where the material constants B_1, B_2 can be determined using the two test results under the quasi-static and dynamic loading conditions. Using equations (2.5) and (2.6), one can calculate the threshold strength at a given strain-rate. Accordingly, one can obtain the shear strength vs. hydrostatic pressure curve at a given strain-rate via obtaining the four material constants, τ_f, α, B_1 and B_2 from the experimental data. Figure 2-5 shows the shear strength vs. the pressure at various strain-rates. Note that the threshold pressure decreases as the strain-rate increases. In other words, the shear strength becomes independent of the pressure starting at a lower pressure.

For a high-strain-rate case, the coefficient β in equation (2.6) becomes almost equal to the limit shear strength. And the threshold pressure in equation (2.5) approaches zero. Accordingly, the material behavior becomes independent of the pressure under the high strain-rate loading condition. For example, Figure 2-4 shows the shear strength of AlN under dynamic loading conditions based on various test results, performed at all different strain-rates. Beyond the pressure level of about $3.5\ \mathrm{GPa}$, the shear strength remains approximately constant while the shear strength at $9\ \mathrm{GPa}$ is obtained under a much higher strain-rate loading condition. Accordingly, the shear strength becomes independent of the applied strain-rate as well as the hydrostatic pressures under the extremely high strain-rate condition.

For the uniaxial loading condition ($P_o = 0$ in equation (2.1)), the relationship between the shear strength and the pressure is expressed as

$$|\tau| = \frac{3}{2}P \qquad (2.7)$$

Plugging equation (2.7) into equation (2.3), one can determine the pressure level at the failure of ceramics under the uniaxial loading condition as

$$P_{trial} = \frac{\beta}{\frac{3}{2} - \alpha}$$

(2.8)

where P_{trial} is a trial pressure. Note that one can use any of equations (2.3) and (2.4) first. Comparing the trial pressure with the threshold pressure, one can determine the uniaxial compressive strength at a given strain-rate as

$$Y_C = Y = \begin{cases} 3P_{trial}, & \text{for } P_{trial} < P_{th} \\ 2\tau_f, & \text{for } P_{trial} \geq P_{th} \end{cases}$$

(2.9)

where the initial failure strength Y is equal to the final strength Y_C under the uniaxial compressive loading condition. For a given strain-rate, one can calculate the uniaxial compressive strength using equation (2.8) and (2.9). Figure 2-6 shows that the calculated uniaxial compressive strength increases with increasing the applied strain-rate. Under the extremely high strain-rate condition ($\dot{\varepsilon} = 10^4$ (1/sec)), the uniaxial strength becomes independent of the applied strain-rate, which is consistent with the observation made in the shear strength curve.

2.2 Two Pressure-Dependent Failure Surfaces

For ceramics, material stiffness gradually deteriorates while microcracks initiate and nucleate under multi-axial loading conditions, and completely diminishes at the final failure. A failure criterion such as the Mohr-Coulomb criterion can be used to describe the final failure of ceramic materials. The Mohr-Coulomb criterion is conceptually simple and mathematically convenient. However, represented by a hexagonal surface at a given pressure, it can be quite inconvenient for numerical implementation [36]. In this section, a failure criterion with a smooth surface is introduced in order to construct a damage model.

Ceramic materials are sensitive to the confining hydrostatic pressure and behave in different fashions under tension and compression. For rocks and soils having similar characteristics, Pariseau [40] proposed a general yield function as

$$f(\boldsymbol{\sigma}) = \left| a_1(\sigma_{22} - \sigma_{33})^2 + a_2(\sigma_{33} - \sigma_{11})^2 + a_3(\sigma_{11} - \sigma_{22})^2 + a_4\sigma_{23}^2 + a_5\sigma_{31}^2 + a_6\sigma_{12}^2 \right|^{\frac{1}{2}n}$$
$$+ a_7\sigma_{11} + a_8\sigma_{22} + a_9\sigma_{33} - 1 = 0 \tag{2.10}$$

where f is a yield function and $\boldsymbol{\sigma}$ is the stress vector. The yield function determines the elastic limit of a material in the stress state. The coefficients $a_1, a_2, \ldots, a_9$ and n are material constants to be determined by experiments. This is often called as the general anisotropic n-type yield function corresponding to the selected value of n. If the three linear terms of the normal stresses are negligible and n is equal to 2, the yield function is reduced to that of the quadratic Hill criterion [41] for anisotropic pressure-independent materials. For isotropic materials, the function f must be

invariant for arbitrary reference axes and the relations between coefficients are obtained as follows:

$$a_1 = a_2 = a_3, \ a_4 = a_5 = a_6 = 6a_1, \ a_7 = a_8 = a_9 \qquad (2.11)$$

Then, the number of material constants in the yield function is reduced down to three. The yield function is expressed using coefficients a_1, a_7, n as

$$f(\boldsymbol{\sigma}) = \left| a_1 \{ (\sigma_{22} - \sigma_{33})^2 + (\sigma_{33} - \sigma_{11})^2 + (\sigma_{11} - \sigma_{22})^2 \} + 6a_1 (\sigma_{23}^2 + \sigma_{31}^2 + \sigma_{12}^2) \right|^{\frac{1}{2}n}$$
$$+ a_7 (\sigma_{11} + \sigma_{22} + \sigma_{33}) - 1 = 0 \qquad (2.12)$$

Or the yield function can be rewritten as

$$f(\boldsymbol{\sigma}) = \left| 6a_1 J_2 \right|^{\frac{1}{2}n} + a_7 I_1 - 1 = 0 \qquad (2.13)$$

where J_2 is the second invariant of the deviatoric stress and I_1 is the first invariant of the stress. In this study, a special case of n-type yield function, the parabolic function (n=2) is used, as originally stated by Torre [42]. Assuming that ceramic is isotropic material, one can write a quadratic yield function as

$$f(\boldsymbol{\sigma}) = 6a_1 J_2 + a_7 I_1 - 1 = 0 \qquad (2.14)$$

where a_1, a_7 are material parameters, which are determined by experimental data. For the plane stress condition, the yield function is simplified to

$$f(\sigma) = 2a_1(\sigma_{11}^2 + \sigma_{22}^2 - \sigma_{11}\sigma_{22} + 3\sigma_{12}^2) + a_7(\sigma_{11} + \sigma_{22}) - 1 = 0 \qquad (2.15)$$

In the present work, the quadratic yield function in equation (2.14) is used to describe the initial failure of ceramics. The initial failure corresponds to the stress state where the microcracks start to grow and ceramics lose their elastic behavior. The material parameters are determined by the uniaxial strengths. For the uniaxial tensile and compressive tests, equation (2.14) becomes

$$\begin{aligned}
2a_1 X^2 + a_7 X - 1 &= 0 \\
2a_1 Y^2 - a_7 Y - 1 &= 0
\end{aligned} \qquad (2.16)$$

where X, Y denotes uniaxial tensile and compressive material strengths. Using equation (2.16), one can solve for the material parameters as

$$a_1 = \frac{1}{2XY}, \ a_7 = \frac{1}{X} - \frac{1}{Y} \qquad (2.17)$$

where the compressive strength is obtained at a given strain-rate as discussed in the previous section. Accordingly, the initial failure surface is determined at a given strain-rate.

For ceramics under compression, it is assumed that material stiffness starts to decrease at the initial failure state and completely diminishes at the final failure state. The yield function alone is not sufficient to describe this material behavior of ceramics under compression. For the compressive failure mode, it is hypothesized that an additional failure surface defining the complete loss of stiffness exists, which is called the final failure surface. The hypothesis is based on the observation from triaxial tests showing that, in the presence of lateral confinement, the compressive strength significantly increases. This indicates that material behavior transitions from brittle to ductile as pressure increases, resulting in higher compressive strength [21]. Since material behavior of partially failed ceramics is also sensitive to pressure, it is reasonable to assume the same form of equation (2.14) for the final failure surface as

$$g(\boldsymbol{\sigma}) = 6b_1 J_2 + b_7 I_1 - 1 = 0 \qquad (2.18)$$

where b_1, b_7 are material parameters. The material parameters can be determined from the triaxial tests. For the triaxial tests, the axial material strength in the compressive loading direction is measured under various confining stresses in the lateral directions. The normal stresses at the failure are

$$\sigma_{11} = -Y_c, \ \sigma_{22} = \sigma_{33} = -p_o \qquad (2.19)$$

where Y_c is the measured compressive strength in the axial direction and p_o is the magnitude of the controlled lateral confining stresses. The material parameters b_1, b_7

can be determined via applying the least-square method to the set of the first and second invariants that represent failure stresses at various confining stresses. Also, the two material parameters are determined at a given strain-rate.

The failure surfaces represent three-dimensional surfaces in the principal stress space. Figure 2-7 shows a cut of the initial and final failure surfaces in the principal stress plane where the out-of-plane stress is equal to the confining stress of a triaxial test ($\sigma_{\mathrm{III}} = -0.2 \times Y_{QS}$), represented by the left-most circle. The principal stresses are non-dimensionalized to the quasi-static, uniaxial compressive strength (Y_{QS}). Note that the three points marked by circles are not located on the constant σ_{III}-plane. To help understanding, another cut of the initial and final failure surfaces is shown in Figure 2-8, where the out-of-plane stress is equal to zero.

In Figure 2-8, the solid curve represents the final failure state and the dashed curve stands for the initial failure state. The two surfaces intersect each other near the points that represent the uniaxial compression states. A solid straight line that passes these two points is expressed as

$$\sigma_{\mathrm{I}} + \sigma_{\mathrm{II}} = C \tag{2.20}$$

where the coefficient C is related to the pressure as

$$P_{br} = -\frac{C}{3} \tag{2.21}$$

where P_{br} is defined as the brittle pressure that determines the failure mode: abrupt or gradual failures. For $P < P_{br}$, the initial and final failure occurs at the same time. Otherwise, the two failures occur under the separate stress states. Note that these two initial and final failure surfaces do not take into account the transition from pressure-dependent to pressure-independent behavior.

2.3 *Modified Failure Surfaces*

The previously introduced failure surfaces are pressure-dependent regardless of the pressure level. However, the shear strength becomes pressure-independent beyond the threshold pressure according to the modified Mohr-Coulomb criterion. At this level of the pressure, pressure-independent failure surfaces must replace the pressure-dependent ones. One can construct the pressure-independent failure surfaces using a failure criterion such as the Von Mises criterion. In general, the Von Mises criterion is written as

$$\mathrm{J}_2 - k^2 = 0 \tag{2.22}$$

where k is the only material constant that determines the failure surface. One can define a pressure-independent, initial failure surface beyond the threshold pressure as

$$f_2(\sigma) = \mathrm{J}_2 - k_i^2 = 0 \tag{2.23}$$

where the material constant k_i is obtained using the stress state of the threshold pressure. For example, the solid straight line in Figure 2-9 represents the stress state equivalent to the threshold pressure. The stress state in the straight line can be expressed by the first invariant of the stress as

$$\mathrm{I}_1 = -3P_{th} \tag{2.24}$$

The solid straight line crosses the pressure-dependent initial and final failure surfaces at two points each. Using equation (2.14) and (2.24), one can obtain the second invariant of the deviatoric stresses for the initial failure surface as

$$\mathrm{J}_2 = \frac{1 + 3a_7 P_{th}}{6a_1} \tag{2.25}$$

Plugging the second invariant into equation (2.23), the material constant for the pressure-independent initial failure surface is obtained as

$$k_i = \sqrt{\frac{1 + 3a_7 P_{th}}{6a_1}} \tag{2.26}$$

Similarly, one can define the pressure-independent final failure surface as

$$g_2(\sigma) = \mathrm{J}_2 - k_o^2 = 0 \tag{2.27}$$

where k_o is the material constant for the pressure-independent final failure surface. One can obtain the Von Mises material constant for the pressure-independent final failure surface using equation (2.18) and (2.27) as

$$k_o = \sqrt{J_2} = \sqrt{\frac{1 + 3b_7 P_{th}}{6b_1}} \qquad (2.28)$$

For example, the pressure-independent failure surfaces are constructed and shown as thick solid and dotted curves in Figure 2-9. In the figure, the inner dotted curve represents the initial failure surface and the outer solid curve represents the final failure surface. These two pressure-independent failure surfaces are only valid when the pressure is greater than the threshold pressure. An example of the modified initial and final failure surfaces, compared to the relative location of the threshold pressure line, is shown in Figure 2-10. Note that these surfaces are constructed at a given strain-rate (quasi-static condition, $\dot{\varepsilon} = 1.0 \times 10^{-4} (1/\sec)$). As the strain-rate increases to $\dot{\varepsilon} = 5 \times 10^2 (1/\sec)$, the initial and final failure surfaces change, as shown in Figure 2-11. In this figure, the pressure-dependent initial failure surface becomes wider than the quasi-static rate counterpart, indicating the increased material strength. In addition, the area between the pressure-dependent initial and final failure surfaces becomes smaller than the quasi-static counterpart, indicating that pressure-dependent behavior is slowly diminishing as the strain-rate goes up.

As the strain-rate increases further to $\dot{\varepsilon} = 1.5 \times 10^3 (1/\text{sec})$, the initial and final failure surfaces shift more and the threshold line moves toward the origin, as shown in Figure 2-12. One can notice that the two pressure-independent surfaces become closer to each other than they are at the lower strain-rate. This indicates that the pressure-dependent failure behavior gradually disappears as the strain-rate increases.

As the strain-rate increases extremely high to $\dot{\varepsilon} = 1 \times 10^4 (1/\text{sec})$, the model for pressure-dependent final failure surface breaks down as the coefficient b_7 becomes very small or close to zero. Eventually, the pressure-dependent final failure surface disappears at a certain strain-rate. Accordingly, the pressure-independent final failure surface cannot be defined. There only remain the initial failure surfaces afterwards, as shown in Figure 2-13. This is consistent with experimental results indicating that the failure mechanism under the compressive loading is dominated by the plastic deformation at an extremely high loading rate while it is dominated by crack nucleation at moderate loading rates.

2.4 Stress-Based Damage Model

For ceramics, it is assumed that there exist two failure states: the initial failure and the final failure. Two failure surfaces are previously introduced to describe these two states. In this section, a damage model is constructed out of these two failure surfaces. The effect of the damage model boils down to the nonlinear and inelastic stress-strain relationships. Assuming that the damage is a quantity, accumulated up to the previous equilibrium state, one can use the previous damage status to determine

the next equilibrium state. For simplicity, the damage status is represented by a single damage parameter. For the one-parameter model, the stress vector at the material point is related to the strain vector as

$$\boldsymbol{\sigma} = (1 - D)\mathbf{C}_e\boldsymbol{\varepsilon} \qquad (2.29)$$

where D is a scalar quantity that stands for the degree of damage, called as the damage parameter henceforth and $\mathbf{C}_e$ is the elastic stiffness matrix for the virgin material. The damage parameter ranges from 0(no damage) to 1(complete damage) depending upon the stress state, the definition of which is introduced later in the section.

Ceramic fails in a brittle fashion if the hydrostatic pressure is lower than the brittle pressure. Note that the brittle pressure varies as the strain-rate increases. Failures under the above condition will be called the tensile failure mode or simply the tensile mode. Otherwise, failures will be called the compressive failure mode or the compressive mode.

For materials subjected to the tensile mode, ceramics lose the stiffness immediately as the stress state increases beyond their elastic limit. Accordingly, the damage parameter is set to either one or zero depending upon the stress state as follows:

$$D_T = \begin{cases} 1, f(\boldsymbol{\sigma}) \geq 0 \\ 0, f(\boldsymbol{\sigma}) < 0 \end{cases} \qquad (2.30)$$

28

where D_T is the damage parameter for the tensile mode and f is the pressure-dependent initial failure function. Note that the initial failure surface is coincident with the final failure surface for the tensile mode. For example, the failure surface for the tensile mode at a given strain-rate is described by curve (1) in Figure 2-14.

For materials subjected to the compressive mode, the stiffness loss tends to be more gradual. The damage parameter for the compressive mode is determined via using both initial and final failure surfaces. Each surface is comprised of two parts, pressure-independent and pressure-dependent parts. For example, the pressure-dependent initial failure surface is represented by curve (1) and the pressure-independent initial failure surface is represented by curve (2) in Figure 2-14. Material is assumed intact as long as the current stress state resides inside the initial failure surfaces irrespective of the pressure as

$$D_C = 0, \begin{cases} f(\boldsymbol{\sigma}) < 0 \text{ for } P < P_{th} \\ \qquad or \\ f_2(\boldsymbol{\sigma}) < 0 \text{ for } P \geq P_{th} \end{cases} \qquad (2.31)$$

where D_C is the damage parameter for the compressive mode and f_2 is defined in equation (2.23).

Otherwise, damage occurs and its level is determined according to the current stress state. In this model, it is assumed that the damage parameter is equal to zero on and inside the initial failure surface and equal to one in the region out of the final failure surface. A method to determine the damage parameter, using the relative

location of the current stress state to these two failure surfaces, is proposed in the following. As shown in Figure 2-15, one can draw a line from a reference stress state $(-Y_{QS}, -Y_{QS})$ of the compressive failure mode to the current principal stress state (marked by '•'), where Y_{QS} is the quasi-static compressive strength. The damage parameter is expressed using three distances to points in the line as

$$D_C = \frac{d - d_i}{d_c - d_i}$$
(2.32)

where d is a distance to the current stress point, d_i is a distance to the initial failure surface point along the line and d_c is a distance to the final failure surface point along the line. Depending upon the stress state, one can select the corresponding initial and final failure surfaces. For example, to estimate the damage parameter for the stress state represented by the cross mark in Figure 2-14, one can use the pressure-dependent initial failure surface (1) and the pressure-dependent final failure surface (3). It appears that the stress state is a bit closer to the final failure surface than to the initial failure surface. In this particular case, the damage parameter is greater than 0.5. Similarly, for the stress state represented by the asterisk mark, one can use failure surfaces (1) and (4). For the stress state represented by the circle mark, one can use failure surfaces (2) and (4).

2.5 *History-Dependent Damage Model*

According to the dynamic failure model proposed by Park [23], the stiffness degradation in failed fiber/matrix composites is instant. Once failed, materials immediately lose their stiffness and remain failed afterwards. This is only partly true for ceramic materials. First and foremost, their failure is more gradual under the compressive loading conditions. In addition, material damage of ceramics is dependent upon the prior damage or loading path as well as the current stress state under the general multi-axial loading conditions.

In this section, a damage model taking into account the damage history is introduced. First, one can obtain the damage parameter as described in the previous section, which requires nothing but the stress state. This damage parameter is defined as the trial damage parameter. Then, the actual damage parameter is determined comparing the trial parameter with the prior damage history of the tensile and the compressive failure modes.

For materials subjected to the tensile failure mode, the damage parameter is set to unity if materials have experienced any damage before, regardless of the compressive or tensile modes. If they are intact up to the current state, the damage parameter accepts the trial damage parameter as it is. This is summarized below:

$$D_T = \begin{cases} 1, \text{ any damage history} \\ D_T^*, \text{ otherwise} \end{cases} \qquad (2.33)$$

where D_T^* is the trial damage parameter for the tensile mode.

For materials subjected to the compressive mode, the damage parameter accepts the trial damage parameter as long as no compressive damage has occurred in the damage history. Damage history of the tensile mode is not as critical as the history of the compressive mode because ceramics, damaged in the tensile mode, tend to keep the load carrying capability under the compressive loading. For materials previously damaged under the compressive mode, the maximum value out of the old and trial damage parameters becomes the new damage parameter. It is based on the idea that damage cannot be reversible. This is summarized as follows:

$$D_C = \begin{cases} D_C^* \text{ ,no damage history in compression} \\ Max(D_C^o, D_C^*) \text{ ,otherwise} \end{cases} \tag{2.34}$$

where D_C^* is the trial damage parameter for the compressive failure mode and D_C^o is the old damage parameter for the compressive failure mode, if any, at the previous equilibrium state.

In sum, the damage parameters are determined by the relative locus of the stress state to the initial and final failure surfaces and corrected by the prior damage history. This is also true regardless of the applied loading rates. For example, consider a material subjected to increased strain-rates. In general, material strength increases as the strain rate increases, but the effect of material damage can decrease if a damage model relies only on the current stress state. Considering damage history and correcting the damage parameters guarantees that the damage level always goes up at the next state.

Chapter 3 Composite Failure Models

In this chapter, failure models for unidirectional composites and woven composites are introduced. For unidirectional composites, in-plane failure criteria introduced by Hashin [28] and Chang et al [32] such as matrix cracking, fiber breakage and matrix/fiber shear failures are used with modifications. For woven composites, the unidirectional failure criteria are modified to take into account different failure mechanisms such as fiber breakages in the two perpendicular fiber directions.

In the finite element analysis, material failure check is performed at every equilibrium state. For composites, the failure check throughout layers of laminates is carried out at every integration point of elements. Once failures are detected, the elastic stiffness of the virgin material is degraded into a reduced value. The stiffness reduction used by Hashin [33] and Padhi, Shenoi, Moy and Hawkins [34] is modified to address different failure modes for woven composites in the present study.

For structures designed to endure extreme conditions such as blasts, the effect of the high strain-rate on the material behavior is of great concern. Experiments carried out by Al-Hassani and Kaddour [43] indicate that material strengths increase in general as the applied loading rate goes up. Accordingly, the effect of the strain-rate on the material strengths is incorporated into the present failure modeling. In the

previous study, Park [23] attempted to address the effect of the high strain-rate on the

constitutive equations of Glass fiber composites via using the viscoplastic formulation

proposed by Sun and Chen [44]. However, the viscoplastic effect on the material

behavior turned out to be insignificant. Accordingly, the viscoplastic effect is ignored

in the present study.

3.1 *Failure Criteria for Unidirectional Composites*

For convenience, an axis system of 1-2-3 is used to describe material failures

in the unidirectional ply, where axis 1 represents a fiber direction, axis 2 represents

the transverse direction and axis 3 represents the thickness direction.

3.1.1 Matrix Cracking Failure (Mode I)

For materials under the tensile stress ($\sigma_{22} > 0$) in the transverse direction, the

matrix cracking failure criterion is written in a quadratic form as

$$e = \left(\frac{\sigma_{22}}{Y_t}\right)^2 + \left(\frac{\sigma_{12}}{SC_{12}}\right)^2 \geq 1 \qquad (3.1)$$

where e is a failure index representing the combined effect of the normal and shear

stresses, Y_t is the tensile strength in the transverse direction and SC_{12} is the in-plane

shear strength. The criterion states that the matrix cracking failure occurs in the

matrix direction if the failure index is equal to or greater than the unity.

For materials under the compressive stress ($\sigma_{22} < 0$) in the transverse direction, the failure criterion is as follows:

$$e = \left(\frac{\sigma_{22}}{Y_c}\right)^2 \geq 1 \tag{3.2}$$

where e is the failure index and Y_c is the compressive strength in the transverse direction. The criterion states that the matrix cracking failure in compression is mainly due to the normal stress under compression.

3.1.2 Fiber Breakage Failure (Mode II)

For materials under tension ($\sigma_{11} > 0$) in the fiber direction, the fiber breakage failure criterion is written as

$$e = \left(\frac{\sigma_{11}}{X_t}\right)^2 + \left(\frac{\sigma_{12}}{SC_{12}}\right)^2 \geq 1 \text{ and } \left(\frac{\sigma_{11}}{X_t}\right)^2 > \left(\frac{\sigma_{12}}{SC_{12}}\right)^2 \tag{3.3}$$

where X_t is the tensile strength in the fiber direction and SC_{12} is the in-plane shear strength. The criterion states that fiber breakage occurs in the fiber direction if the failure index e is equal to or greater than the unity and the effect of normal stress is greater than that of shear stress. In general, the in-plane shear strength SC_{12} is in the order of one tenth of the tensile strength. The second condition in equation (3.3)

ensures that the primary cause of fiber breakage is the high normal stress in the fiber direction.

For material under compression ($\sigma_{11} < 0$) in the fiber direction, the failure criterion is

$$e = \left(\frac{\sigma_{11}}{X_c}\right)^2 \geq 1 \qquad (3.4)$$

where X_c is the compressive strength in the fiber direction.

3.1.3 Fiber-Matrix Shear Failure (Mode III)

Chang and Chang [30] proposed a failure criterion for fiber-matrix shearing failure as follows: For materials under tension ($\sigma_{11} > 0$) in the fiber direction, the fiber-matrix shear failure criterion is defined as

$$e = \left(\frac{\sigma_{11}}{X_t}\right)^2 + \left(\frac{\sigma_{12}}{SC_{12}}\right)^2 \geq 1 \text{ and } \left(\frac{\sigma_{11}}{X_t}\right)^2 < \left(\frac{\sigma_{12}}{SC_{12}}\right)^2 \qquad (3.5)$$

where the criterion states that the shear failure occurs when the effect of the shear stress is greater than that of the normal stress.

For materials under compression ($\sigma_{11} < 0$) in the fiber direction, the fiber-matrix shear criterion is

$$e = \left(\frac{\sigma_{11}}{X_c}\right)^2 + \left(\frac{\sigma_{12}}{SC_{12}}\right)^2 \geq 1 \text{ and } \left(\frac{\sigma_{11}}{X_c}\right)^2 < \left(\frac{\sigma_{12}}{SC_{12}}\right)^2 \qquad (3.6)$$

3.2 *Property Degradation Model for Unidirectional Composites*

For progressive failure analyses, material failure check is performed at every equilibrium state. Once a failure is detected at a local material point, the elastic stiffness of the intact material is degraded into a reduced value. For a unidirectional ply, the in-plane elastic stiffness matrix for the virgin material is expressed as follows:

$$\mathbf{C}_e = \begin{bmatrix} \dfrac{E_1}{1-v_{12}v_{21}} & \dfrac{v_{12}E_1}{1-v_{12}v_{21}} & 0 \\ \dfrac{v_{21}E_2}{1-v_{12}v_{21}} & \dfrac{E_2}{1-v_{12}v_{21}} & 0 \\ 0 & 0 & G_{12} \end{bmatrix} \qquad (3.7)$$

where E_1 is the longitudinal modulus, E_2 is the transverse modulus, v_{12} is the major Poisson's ratio and G_{12} is the shear modulus. The stiffness matrix is degraded corresponding to failure modes defined in the previous section. For material points undergoing multiple failure modes, the minimum in each entry of the reduced stiffness matrices is used.

3.2.1 Matrix Cracking Failure (Mode I)

For the complete failure of matrix, the laminate can be treated as a fiber bundle. Based on this assumption, a degradation model is proposed by Park [23] via setting the shear modulus and transverse modulus to zeros as follows:

$$\mathbf{C}_{\mathrm{deg}} = \begin{bmatrix} v_f E_f & 0 & 0 \\ 0 & 0 & 0 \\ 0 & 0 & 0 \end{bmatrix} \tag{3.8}$$

where $\mathbf{C}_{\mathrm{deg}}$ is the degraded stiffness matrix, v_f is the fiber volume fraction and E_f is the longitudinal modulus of the fiber. However, a matrix cracking failure at a local point is not likely to cause a fiber bundle. Besides, this approach can cause a numerical instability by prematurely predicting structural failures based on local material failures. In addition, the stiffness in the fiber direction is only mildly affected by the local matrix failure.

In this study, it is assumed that matrix is broken at a local point and the extensional modulus E_2 in the transverse direction is reduced to a small fraction of the original value, instead of zero. The small fraction helps avoiding the numerical instability when material failure occurs throughout the thickness at an integration point. Poisson's ratio v_{12} is reduced to zero so that normal stress is not transferred to the failed direction. The in-plane elastic stiffness matrix at the failed integration point is modified at the corresponding layer as below:

38

$$
\mathbf{C}_{\text{deg}} = \begin{bmatrix} E_1 & 0 & 0 \\ 0 & C_{22} \times md & 0 \\ 0 & 0 & G_{12} \end{bmatrix} \tag{3.9}
$$

where C_{22} is the 2nd row and 2nd column entry of the original matrix and md is a small number representing the degree of material degradation. The material degradation parameter should be determined by convergence tests. One may use 1×10^{-6} for the first estimation.

3.2.2 Fiber Breakage Failure (Mode II)

For the fiber breakage in the laminate direction, the extensional modulus E_1 and Poisson's ratio v_{12} are reduced to small fractions. The in-plane elastic stiffness matrix is degraded at the failed integration point of a layer as below.

$$
\mathbf{C}_{\text{deg}} = \begin{bmatrix} C_{11} \times md & 0 & 0 \\ 0 & C_{22} \times md & 0 \\ 0 & 0 & G_{12} \times md \end{bmatrix} \tag{3.10}
$$

where C_{ii} is the entry of the original stiffness matrix at the ith row and i^{th} column.

3.2.3 Fiber-Matrix Shear Failure (Mode III)

For the fiber-matrix shear failure, the in-plane Poisson's ratio v_{12} and the shear modulus G_{12} are reduced to zero while the extensional modulus in the fiber direction remains unaffected. The in-plane elastic stiffness matrix at the integration point is degraded only at the failed layer as below.

$$\mathbf{C}_{\text{deg}} = \begin{bmatrix} E_1 & 0 & 0 \\ 0 & C_{22} \times md & 0 \\ 0 & 0 & G_{12} \times md \end{bmatrix} \qquad (3.11)$$

3.3 *Failure Criteria for Woven Composites*

For the woven composites, a single layer can be viewed as interlocks of two perpendicular fibers, resulting in little or no difference of material properties in the two fiber directions. These two perpendicular fibers affect failure mechanisms in the woven composites. For example, the matrix domination in the transverse direction, common to unidirectional composites, disappears. Accordingly, a failure model different from the unidirectional case is proposed. For instance, fiber breakages in both fiber directions are of main concerns in woven composites. In this study, the failure criteria proposed by Hashin [28] and Chang and Lessard [31] are modified to represent failure mechanisms of the woven composites. For convenience, the warp direction is designated axis-1 and the fill direction is designated axis-2.

3.3.1 Fiber Breakage Failure in Fill Direction (Mode I)

For materials under tension ($\sigma_{22} > 0$) in the fill direction, the fiber breakage failure criterion is written in a quadratic form as

$$e = \left(\frac{\sigma_{22}}{X_t}\right)^2 + \left(\frac{\sigma_{12}}{SC_{12}}\right)^2 \geq 1 \text{ and } \left(\frac{\sigma_{22}}{X_t}\right)^2 > \left(\frac{\sigma_{12}}{SC_{12}}\right)^2 \qquad (3.12)$$

where e is a failure index representing the combined effect of the normal and shear stresses, X_t is the tensile strength in the fiber direction and SC_{12} is the in-plane shear strength. The criterion is identical to the fiber breakage criterion for the unidirectional composites. The criterion states that fiber breakage occurs when the failure index is equal to or greater than the unity and the effect of normal stress is greater than that of shear stress.

For materials under compression ($\sigma_{22} < 0$) in the fill direction, the failure criterion is as follows:

$$e = \left(\frac{\sigma_{22}}{X_c}\right)^2 \geq 1 \qquad (3.13)$$

where e is the failure index and X_c is the compressive strength in the fiber direction. The criterion states that fiber failure under compression is mainly due to the normal stress because buckling dominates the failure.

3.3.2 Fiber Breakage Failure in Warp Direction (Mode II)

The failure criterion used for the fiber breakage in Axis-2 (the fill direction) is applied to the fiber breakage in Axis-1 (the warp direction). The only difference is the normal stress component in the selected fiber direction. For the normal stress in tension ($\sigma_{11} > 0$) in the warp direction, the failure criterion is written as

$$e = \left(\frac{\sigma_{11}}{X_t}\right)^2 + \left(\frac{\sigma_{12}}{SC_{12}}\right)^2 \geq 1 \text{ and } \left(\frac{\sigma_{11}}{X_t}\right)^2 \geq \left(\frac{\sigma_{12}}{SC_{12}}\right)^2 \quad (3.14)$$

where the criterion states that fiber breakage occurs when the failure index is equal to or greater than the unity and the effect of normal stress is greater than that of shear stress.

For the normal stress in compression ($\sigma_{11} < 0$) in the warp direction, the failure criterion is

$$e = \left(\frac{\sigma_{11}}{X_c}\right)^2 \geq 1 \quad (3.15)$$

where material strengths X_c is same as the one used in the fill direction.

3.3.3 Fiber-Matrix Shear Failure (Mode III)

For the normal stress in tension ($\sigma_{ii} > 0$, $i = 1, 2$), the fiber-matrix shear criterion is defined as

$$e = \left(\frac{\sigma_{ii}}{X_t}\right)^2 + \left(\frac{\sigma_{12}}{SC_{12}}\right)^2 \geq 1 \text{ and } \left(\frac{\sigma_{ii}}{X_t}\right)^2 < \left(\frac{\sigma_{12}}{SC_{12}}\right)^2 \qquad (3.16)$$

where the criterion states that the shear failure occurs when the effect of shear is greater than that of normal stress. The shear failure occurs when the criterion is satisfied at least with one of the normal stresses.

For the normal stress in compression ($\sigma_{ii} < 0$, $i = 1, 2$), the fiber-matrix shear criterion is

$$e = \left(\frac{\sigma_{ii}}{X_c}\right)^2 + \left(\frac{\sigma_{12}}{SC_{12}}\right)^2 \geq 1 \text{ and } \left(\frac{\sigma_{ii}}{X_c}\right)^2 < \left(\frac{\sigma_{12}}{SC_{12}}\right)^2 \qquad (3.17)$$

3.4 *Property Degradation Model for Woven Composites*

In this section, a property degradation model for woven composites is proposed according to the modified failure criteria. For example, the fiber breakages in the unidirectional composites reduce the whole stiffness matrix as shown in equation (3.10). For woven composites, the effect of fiber breakages in one direction is not as strong because of the intact fibers existing in the perpendicular direction to the failed ones.

3.4.1 Fiber Breakage Failure in Fill Direction (Mode I)

For the fiber breakage failure, it is assumed that fiber is completely broken and the extensional modulus E_2 in the failed fiber direction is reduced to a small number. Poisson's ratio v_{12} is reduced to zero so that no normal stress is sustained in the failed direction. The in-plane elastic stiffness matrix at an integration point is degraded only at the failed layer as below:

$$\mathbf{C}_{deg} = \begin{bmatrix} E_1 & 0 & 0 \\ 0 & C_{22} \times md & 0 \\ 0 & 0 & G_{12} \end{bmatrix} \qquad (3.18)$$

For woven composites, the stiffness degradation due to the fiber breakage failure is not as severe as the one for unidirectional composites because woven composites have intact fibers in the other fiber direction.

3.4.2 Fiber Breakage Failure in Warp Direction (Mode II)

For the fiber breakage failure in the warp direction, the extensional modulus E_1 is reduced to a small number while Poisson's ratio v_{12} is reduced to zero. The in-plane elastic stiffness matrix is degraded at the failed layer as below.

$$\mathbf{C}_{deg} = \begin{bmatrix} C_{11} \times md & 0 & 0 \\ 0 & E_2 & 0 \\ 0 & 0 & G_{12} \end{bmatrix} \qquad (3.19)$$

3.4.3 Fiber-Matrix Shear Failure (Mode III)

The fiber-matrix shear failure makes the two perpendicular fibers act independent of each other. Accordingly, the in-plane Poisson's ratio v_{12} is reduced to zero and the shear modulus G_{12} is reduced to a small fraction while the two extensional moduli remain unaffected. The in-plane elastic stiffness matrix is degraded at the layer of the integration point as below.

$$\mathbf{C}_{\text{deg}} = \begin{bmatrix} E_1 & 0 & 0 \\ 0 & E_2 & 0 \\ 0 & 0 & G_{12} \times md \end{bmatrix} \quad (3.20)$$

3.5 *Strain-Rate Effect on Material Strengths*

3.5.1 Unidirectional Composites

In general, the in-plane strengths increase as the applied strain-rate increases. However, experiments performed at moderate to high strain-rate levels indicate that material strength in the longitudinal direction is not as sensitive to the strain-rate as the strength in the transverse direction. In this study, the longitudinal strength is assumed to be independent of the strain-rate at moderate to high levels. The transverse strength is modeled as a function of the strain-rate as follows:

$$Y = Y_{QS} + A\dot{\varepsilon}_{22} \quad (3.21)$$

where Y_{QS} is a quasi-static, transverse strength and A is a material constant.

3.5.2 Woven Composites

Uniaxial and off-axis tension tests were carried out by Park [23] to investigate the strain-rate effect on the longitudinal and shear strengths. For woven S-2 Glass fabric ply, the strain-rate dependent in-plane shear strength is modeled as

$$SC_{12} = 8.08 \log \dot{\varepsilon}_{12} + 119.3, (MPa) \tag{3.22}$$

The strain-rate dependent longitudinal strength is modeled as a linear least square fit of experimental data as

$$X_t = 48.16 \log \dot{\varepsilon}_{11} + 727.6, (MPa) \tag{3.23}$$

For the transverse direction, one can use the same material parameters as

$$Y_t = 48.16 \log \dot{\varepsilon}_{22} + 727.6, (MPa) \tag{3.24}$$

In the present study, it is assumed that the above material constants that represent the strain-rate dependency of material strengths remain the same for the compressive strengths.

Chapter 4 Finite Element Formulation for Dynamic Failure Analyses

This chapter describes the nine-node assumed strain solid shell element formulation for dynamic problems to model the nonlinear behavior of composites and ceramics panels under the blast wave pressure loading. First, the nonlinear solid shell element formulation is described. Subsequently, the numerical scheme for dynamic analyses is explained. Lastly, the procedure for the dynamic failure analysis is summarized.

For finite element modeling, both nine-node and eighteen-node elements are used. These elements are equivalent to each other, and the element stiffness matrix and the element load vector can be easily converted from one to the other. A brief description of the transformation is provided in the chapter.

The modeling approach of using multiple elements through the thickness results in increase of the problem size. In the present study, a parallel solver is developed to accommodate the increased problem size, based on the multi-frontal algorithm. A brief introduction to the multi-frontal solver is provided in this chapter.

4.1 Eighteen-Node and Nine-Node Solid Shell Elements

Figure 4-1 shows two versions of a solid shell element, one with eighteen nodes and the other with nine nodes. The eighteen-node version has three degrees of freedom per node while the nine-node version has six degrees of freedom per node. The eighteen-node version has been often used to model multi-layered structures, due to its convenience in stacking elements through the thickness.

These two versions are equivalent to each other and their geometry can be easily convertible from one to the other as follows: For the eighteen-node version, the position vector $\mathbf{x}$ can be described as

$$\mathbf{x} = \frac{1-\varsigma}{2}\mathbf{x}_{bot} + \frac{1+\varsigma}{2}\mathbf{x}_{top} \tag{4.1}$$

where $\mathbf{x}_{bot}$, $\mathbf{x}_{top}$ is the position vector at the bottom and top surface, respectively and ς is a parental coordinate in the thickness direction. For the nine-node version, the geometry of the solid shell can be equivalently expressed as

$$\mathbf{x} = \mathbf{x}_o + \varsigma \frac{t}{2}\mathbf{a}_3 \tag{4.2}$$

where $\mathbf{x}_o$ is a position vector on the shell mid-surface and $\mathbf{a}_3$ is the unit vector through the thickness t. This position vector and the unit vector of the nine-node version are related to the position vectors of the eighteen-node version and the thickness as

$$\mathbf{x}_o = \frac{\mathbf{x}_{top} + \mathbf{x}_{bot}}{2}, \quad \mathbf{a}_3 = \frac{\mathbf{x}_{top} - \mathbf{x}_{bot}}{t} \tag{4.3}$$

For the nine-node version, the position vector $\mathbf{x}$ in equation (4.2) is expressed as

$$\mathbf{x} = \sum_{i=1}^{n} N_i(\xi,\eta)(\mathbf{x}_o)_i + \varsigma \sum_{i=1}^{n} N_i(\xi,\eta)(\frac{t}{2}\mathbf{a}_3)_i \tag{4.4}$$

where n is the number of element nodes on the mid-surface, $(\mathbf{x}_o)_i$ is the nodal position vector, t is thickness of the shell element at node i and $N_i(\xi,\eta)$ is the mapping function corresponding to the node i. Node numbering of nine-node element is shown in Figure 4-2, and the mapping functions for the nine-node element are provided in Appendix A.

Similarly, the displacement vector of the eighteen-node version is easily convertible to that of the nine-node version. For the eighteen-node version, the displacement vector $\mathbf{u}$ is expressed as

$$\mathbf{u} = \frac{1-\varsigma}{2}\mathbf{u}_{bot} + \frac{1+\varsigma}{2}\mathbf{u}_{top} \tag{4.5}$$

where $\mathbf{u}_{bot}$, $\mathbf{u}_{top}$ is the displacement vector at the bottom and top surface, respectively. For the nine-node version, the displacement vector $\mathbf{u}$ can be expressed as

$$\mathbf{u} = \mathbf{u}_o + \varsigma \frac{t}{2} \mathbf{u}_z \qquad (4.6)$$

where the two displacement vectors $\mathbf{u}_o$, $\mathbf{u}_z$ are related to the kinematic parameters of the eighteen-node version as

$$\mathbf{u}_o = \frac{\mathbf{u}_{top} + \mathbf{u}_{bot}}{2}, \ \mathbf{u}_z = \frac{\mathbf{u}_{top} - \mathbf{u}_{bot}}{t} \qquad (4.7)$$

For the nine-node version, the displacement vector $\mathbf{u}$ in equation (4.6) is expressed as

$$\mathbf{u} = \sum_{i=1}^{n} N_i(\xi,\eta)(\mathbf{u}_o)_i + \varsigma \sum_{i=1}^{n} N_i(\xi,\eta)(\frac{t}{2}\mathbf{u}_z)_i \qquad (4.8)$$

where $N_i(\xi,\eta)$ is the shape function corresponding to the i-th node, which is identical to the mapping function. As a contrast to the traditional degenerated shell, no rotational angles are used in the solid shell approach.

4.2 Incremental Forms of Displacement, Strain and Stress Vectors

A geometrically nonlinear formulation for the nine-node solid shell element and the eighteen-node solid shell element is introduced, by Rhiu and Lee [45] and Kim and Lee [46], to account for large rotations. Equilibrium must be satisfied over the deformed configuration. For this purpose, a geometrically nonlinear assumed

strain solid shell formulation is developed based on the total Lagrangian description that employs the Green strain and the second Piola-Kirchhoff stress. In the geometrically nonlinear formulation, the displacement, strain, stress vectors are all expressed in incremental forms.

Based on the description of the geometry and kinematics of deformation, the displacement vector **u** at (i+1)-th state is expressed in incremental form as

$$\mathbf{u} = {}^{(i)}\mathbf{u} + \Delta\mathbf{u} \tag{4.9}$$

where ${}^{(i)}\mathbf{u}$ is the displacement vector at the known state and $\Delta\mathbf{u}$ represents the increment between the two states. Note that the known state is not necessary an equilibrium state. This vectorial approach to the description of kinematics allows for a large load increment, compared to the conventional degenerated shell elements that employ rotational angles.

The Green strain tensor is defined based on the displacement field as

$$\bar{\varepsilon}_{ij} = \frac{1}{2}(u_{i,j} + u_{j,i} + u_{k,i}u_{k,j}) \quad i,j = 1,2,3 \tag{4.10}$$

where the over-bar stands for displacement-dependency of the strain tensor and the repeated index k represents summation from 1 to 3. Using equation (4.9) and (4.10), one can obtain the incremental form of the Green strain as follows:

$$\overline{\varepsilon}_{ij} = {}^{(i)}\overline{\varepsilon}_{ij} + \Delta\overline{e}_{ij} + \Delta\overline{h}_{ij} \tag{4.11}$$

where

$$
\begin{aligned}
{}^{(i)}\overline{\varepsilon}_{ij} &= \frac{1}{2}({}^{(i)}u_{i,j} + {}^{(i)}u_{j,i} + {}^{(i)}u_{k,i}\,{}^{(i)}u_{k,j}) \\
\Delta\overline{e}_{ij} &= \frac{1}{2}(\Delta u_{i,j} + \Delta u_{j,i} + {}^{(i)}u_{k,i}\Delta u_{k,j} + \Delta u_{k,i}\,{}^{(i)}u_{k,j}) \\
\Delta\overline{h}_{ij} &= \frac{1}{2}\Delta u_{k,i}\Delta u_{k,j}
\end{aligned}
\tag{4.12}
$$

Using the above tensor notation, one may write an engineering strain vector as follows:

$$\overline{\mathbf{\varepsilon}} = \begin{Bmatrix} \overline{\varepsilon}_{xx} \\ \overline{\varepsilon}_{yy} \\ \overline{\varepsilon}_{zz} \\ \overline{\varepsilon}_{xy} \\ \overline{\varepsilon}_{yz} \\ \overline{\varepsilon}_{zx} \end{Bmatrix} = \begin{Bmatrix} u_{1,1} \\ u_{2,2} \\ u_{3,3} \\ u_{1,2} + u_{2,1} \\ u_{2,3} + u_{3,2} \\ u_{3,1} + u_{1,3} \end{Bmatrix} \tag{4.13}$$

The displacement-dependent strain vector can be expressed in incremental form as

$$\overline{\mathbf{\varepsilon}} = {}^{(i)}\overline{\mathbf{\varepsilon}} + \Delta\overline{\mathbf{e}} + \Delta\overline{\mathbf{h}} \tag{4.14}$$

where $\Delta\overline{\mathbf{e}}$ is a linear function of $\Delta\mathbf{u}$ and $\Delta\overline{\mathbf{h}}$ is a quadratic function of $\Delta\mathbf{u}$. Similarly, the virtual strain vector can be written as

$$\delta\overline{\boldsymbol{\varepsilon}} = \delta\overline{\mathbf{e}} + \delta\overline{\mathbf{h}} \qquad (4.15)$$

In the assumed strain formulation proposed by Lee and Pian [47], a displacement-independent strain field is introduced in addition to the displacement-dependent strain field to avoid the locking phenomenon. The assumed strain field is related to the displacement-dependent strain through compatibility equations, which will be discussed further in the later section. The assumed independent strain vector is expressed in incremental form as follows:

$$\boldsymbol{\varepsilon} = {}^{(i)}\boldsymbol{\varepsilon} + \Delta\boldsymbol{\varepsilon} \qquad (4.16)$$

where the assumed strain vector is written with respect to special local coordinates system. The local coordinate system, as described by Park and Lee [48], is used to maintain the element invariance. The assumed strain formulation, combined with the solid shell element formulation, is tailored for composite analyses by Yeom and Lee [49].

The stress vector is also expressed in incremental form as follows:

$$\boldsymbol{\sigma} = {}^{(i)}\boldsymbol{\sigma} + \Delta\boldsymbol{\sigma} \qquad (4.17)$$

These incremental forms of the displacement, strain and stress vectors are used to develop the equilibrium and compatibility equations in incremental form in the later section.

4.3 *Constitutive Equation for Damage and Failure Models*

For the linear elastic behavior, the stress and strains vectors are related as

$$\boldsymbol{\sigma} = \mathbf{C}_e \boldsymbol{\varepsilon} \tag{4.18}$$

where $\mathbf{C}_e$ is a matrix of elastic material constants for intact materials, provided in Appendix B. The virtual stress vector can be defined using the above relation as

$$\delta\boldsymbol{\sigma} = \mathbf{C}_e \delta\boldsymbol{\varepsilon} \tag{4.19}$$

For the ceramic damage model, the stress-strain relation is expressed as

$$\boldsymbol{\sigma} = (1 - D)\mathbf{C}_e \boldsymbol{\varepsilon} \tag{4.20}$$

where D is the damage parameter as defined in Chapter 2. The damage parameter is set to one as the material completely fails. For the composite failure model, the stress-strain relation is expressed as

$$\boldsymbol{\sigma} = \mathbf{C}_{\text{deg}} \boldsymbol{\varepsilon} \tag{4.21}$$

where $\mathbf{C}_{\text{deg}}$ is the degraded stiffness matrix corresponding to the detected failure modes as described in Chapter 3.

4.4 Equilibrium and Compatibility Equations

For a solid in equilibrium,

$$\int_V \delta\bar{\boldsymbol{\varepsilon}}^{\mathrm{T}}\boldsymbol{\sigma}dV - \delta W = 0 \qquad (4.22)$$

where $\delta\bar{\boldsymbol{\varepsilon}}$ is the virtual displacement-dependent strain vector, $\boldsymbol{\sigma}$ is the second Piola-Kirchhoff stress vector and δW is the virtual work due to the applied load and V represents the volume of the original configuration prior to any deformation. Equilibrium is satisfied over the deformed configuration based on the total Lagrangian description.

For dynamic problems, the acceleration of the infinitesimal mass can be represented by the applied body force. Assuming that there is no body force other than the one due to the acceleration, one can express the equilibrium equation as

$$\int_V \delta\bar{\boldsymbol{\varepsilon}}^{\mathrm{T}}\boldsymbol{\sigma}dV + \int_V \delta\mathbf{u}^{\mathrm{T}}\ddot{\mathbf{u}}\rho dV - \delta W_{\mathrm{T}} = 0 \qquad (4.23)$$

where $\delta\mathbf{u}$ is the virtual displacement vector, $\ddot{\mathbf{u}}$ is the acceleration vector and δW_{T} is the virtual work due to the traction force.

In the conventional shell element formulation, the displacement vector is the only independent variable. However, shell elements based on the assumed displacement alone suffer from the element locking. An assumed strain formulation

has been introduced to alleviate the element locking. In the assumed strain formulation, the strain field is assumed independent of the displacement vector and the displacement-independent strain is related with the displacement-dependent strain through the compatibility equation as

$$\int_V \delta\boldsymbol{\sigma}^T (\overline{\boldsymbol{\varepsilon}} - \boldsymbol{\varepsilon}) dV = 0 \tag{4.24}$$

where $\delta\boldsymbol{\sigma}$ is the virtual stress vector. The parameter for the assumed strain is eliminated at element level.

4.4.1 Finite Element Discretization

For the nine-node solid shell element, the element degrees of freedom vector $\mathbf{q}_e$ consists of nodal degrees of freedom as follows:

$$\mathbf{q}_e = \lfloor (u_o, v_o, w_o, u_z, v_z, w_z)_1 \quad \dots \quad (u_o, v_o, w_o, u_z, v_z, w_z)_n \rfloor^T \tag{4.25}$$

where n is the number of nodes in the element.

In the solid shell element, the displacement vector $\mathbf{u}$, the acceleration vector $\ddot{\mathbf{u}}$, the linear part of the displacement-dependent strain vector $\overline{\mathbf{e}}$ in equation (4.14) and the assumed strain vector $\boldsymbol{\varepsilon}$ can be symbolically expressed as follows:

$$\mathbf{u} = \mathbf{N}(\xi, \eta, \varsigma)\mathbf{q}_e, \quad \ddot{\mathbf{u}} = \mathbf{N}(\xi, \eta, \varsigma)\ddot{\mathbf{q}}_e \tag{4.26}$$

56

$$\overline{\mathbf{e}} = \mathbf{B}(\xi, \eta, \varsigma)\mathbf{q}_e \tag{4.27}$$

$$\boldsymbol{\varepsilon} = \mathbf{P}(\xi, \eta, \varsigma)\boldsymbol{\alpha} \tag{4.28}$$

where $\mathbf{N}$ is a matrix of the shape functions, $\mathbf{B}$ is a matrix that relates the linear part of the displacement-dependent strain vector to the element degrees of freedom vector, $\mathbf{P}$ is a matrix of assumed strain shape functions and $\boldsymbol{\alpha}$ is a vector of assumed strain coefficients. Cho [50] provided derivation for all the symbolic functions and explained the selection process of the assumed strain shapes functions in great details. Subsequently, their incremental forms and virtual forms are written as

$$\Delta\mathbf{u} = \mathbf{N}\Delta\mathbf{q}_e, \quad \delta\mathbf{u} = \mathbf{N}\delta\mathbf{q}_e \tag{4.29}$$

$$\Delta\overline{\mathbf{e}} = \mathbf{B}\Delta\mathbf{q}_e, \quad \delta\overline{\mathbf{e}} = \mathbf{B}\delta\mathbf{q}_e \tag{4.30}$$

$$\Delta\boldsymbol{\varepsilon} = \mathbf{P}\Delta\boldsymbol{\alpha}, \quad \delta\boldsymbol{\varepsilon} = \mathbf{P}\delta\boldsymbol{\alpha} \tag{4.31}$$

where $\Delta\mathbf{q}_e$ is the incremental element degree of freedom vector and $\Delta\boldsymbol{\alpha}$ is a vector of unknown assumed strain parameters.

4.4.2 Compatibility Equation in Incremental Form

For finite element modeling, the integration in the compatibility equation is carried out over each element and summed over the entire volume. Due to the arbitrary nature of the virtual stress vector $\delta\boldsymbol{\sigma}$, the compatibility must be satisfied in each element as

$$\int_{V_e} \delta\boldsymbol{\sigma}^{\mathrm{T}}\left(\overline{\boldsymbol{\varepsilon}}-\boldsymbol{\varepsilon}\right)dV = 0 \tag{4.32}$$

where the subscript e indicated that the integration is over an individual element. The incremental form of the above element compatibility equation can be obtained by substituting the incremental expressions for the two strain vectors in equations (4.14) and (4.16).

$$\int_{V_e} \delta\boldsymbol{\sigma}^{\mathrm{T}}\left(^{(i)}\overline{\boldsymbol{\varepsilon}}-{}^{(i)}\boldsymbol{\varepsilon}\right)dV + \int_{V_e} \delta\boldsymbol{\sigma}^{\mathrm{T}}\left(\Delta\overline{\mathbf{e}}+\Delta\overline{\mathbf{h}}\right)dV - \int_{V_e} \delta\boldsymbol{\sigma}^{\mathrm{T}}\Delta\boldsymbol{\varepsilon}\,dV = 0 \tag{4.33}$$

Substituting the virtual stress vector in equation (4.19) and the symbolic expressions for the strain vectors in equations (4.30) and (4.31) into the above equation, and canceling the high-order term yields,

$$\delta\boldsymbol{\alpha}^{\mathrm{T}}\left(^{(i)}\mathbf{F}_e + \mathbf{G}\Delta\mathbf{q}_e - \mathbf{H}\Delta\boldsymbol{\alpha}\right) = 0 \tag{4.34}$$

where

58

$$^{(i)}\mathbf{F}_e = \int_{V_e} \mathbf{P}^{\mathrm{T}}\mathbf{C}(^{(i)}\overline{\boldsymbol{\varepsilon}} - {}^{(i)}\boldsymbol{\varepsilon})dV, \ \mathbf{G} = \int_{V_e} \mathbf{P}^{\mathrm{T}}\mathbf{C}\mathbf{B}dV, \ \mathbf{H} = \int_{V_e} \mathbf{P}^{\mathrm{T}}\mathbf{C}\mathbf{P}dV \qquad (4.35)$$

The $^{(i)}\mathbf{F}_e$ vector represents the compatibility mismatch in the element between the displacement-dependent strain and the independently assumed strain at the i-th state. For an arbitrary vector $\delta\boldsymbol{\alpha}$, the vector of unknown strain parameters $\Delta\boldsymbol{\alpha}$ in equation (4.34) is obtained as follows:

$$\Delta\boldsymbol{\alpha} = \mathbf{H}^{-1}\left(^{(i)}\mathbf{F}_e + \mathbf{G}\Delta\mathbf{q}_e\right) \qquad (4.36)$$

4.4.3 Equilibrium Equation in Incremental Form

Substituting the virtual strain vector and the incremental stress vector in equations (4.15) and (4.17), one can express the strain energy term of the equilibrium equation in incremental form as

$$\int_V \delta\overline{\boldsymbol{\varepsilon}}^{\mathrm{T}}\boldsymbol{\sigma}dV = \int_V \delta\overline{\mathbf{e}}^{\mathrm{T}\,(i)}\boldsymbol{\sigma}dV + \int_V \delta\overline{\mathbf{e}}^{\mathrm{T}}\Delta\boldsymbol{\sigma}dV + \int_V \delta\overline{\mathbf{h}}^{\mathrm{T}\,(i)}\boldsymbol{\sigma}dV + A_n \qquad (4.37)$$

where A_n is a higher order term in $\Delta\mathbf{u}$. For the finite element approximation, the integration is carried out over the volume of the individual element and summed over the entire elements as

$$\int_V \delta\overline{\boldsymbol{\varepsilon}}^{\mathrm{T}}\boldsymbol{\sigma}dV = \sum \int_{V_e} \delta\overline{\boldsymbol{\varepsilon}}^{\mathrm{T}}\boldsymbol{\sigma}dV \qquad (4.38)$$

59

where $\sum$ stands for summation over all elements. Using the virtual and incremental expressions of stress and strain vectors in the equations (4.30) and (4.31), one can rewrite the strain energy term as follows:

$$\int_V \delta\overline{\boldsymbol{\varepsilon}}^{\mathrm{T}}\boldsymbol{\sigma}dV = \sum \delta\mathbf{q}_e^{\mathrm{T}}\left({}^{(i)}\mathbf{Q}_e + \mathbf{G}^{\mathrm{T}}\Delta\boldsymbol{\alpha} + \mathbf{K}_s\Delta\mathbf{q}_e + A_n \right) \tag{4.39}$$

where

$$ {}^{(i)}\mathbf{Q}_e = \int_{V_e} \mathbf{B}^{\mathrm{T}\,(i)}\boldsymbol{\sigma}dV, \quad \delta\mathbf{q}_e^{\mathrm{T}}\mathbf{K}_s\Delta\mathbf{q}_e = \int_{V_e} \delta\overline{\mathbf{h}}^{\mathrm{T}\,(i)}\boldsymbol{\sigma}dV \tag{4.40}$$

${}^{(i)}\mathbf{Q}_e$ is the element load vector due to the stress ${}^{(i)}\boldsymbol{\sigma}$ and $\mathbf{K}_s$ is the element stiffness matrix due to the stress ${}^{(i)}\boldsymbol{\sigma}$. Placing equation (4.36) into equation (4.39), one can rewrite the strain energy term as

$$\int_V \delta\overline{\boldsymbol{\varepsilon}}^{\mathrm{T}}\boldsymbol{\sigma}dV = \sum \delta\mathbf{q}_e^{\mathrm{T}}\left(\mathbf{K}_e\Delta\mathbf{q}_e + {}^{(i)}\mathbf{Q} + \mathbf{G}^{\mathrm{T}}\mathbf{H}^{-1\,(i)}\mathbf{F}_e + A_n + B_n \right) \tag{4.41}$$

where the element tangent stiffness matrix is expressed as

$$\mathbf{K}_e = \mathbf{G}^{\mathrm{T}}\mathbf{H}^{-1}\mathbf{G} + \mathbf{K}_s \tag{4.42}$$

60

Alternatively, the strain energy in equation (4.22) can be viewed as a nonlinear function of the global degrees of freedom vector $\mathbf{q}$ as

$$\int_V \delta\bar{\boldsymbol{\varepsilon}}^{\mathrm{T}}\boldsymbol{\sigma}dV = \delta\mathbf{q}^{\mathrm{T}}\mathbf{f}(\mathbf{q}) \qquad (4.43)$$

where the $\delta\mathbf{q}$ is the virtual global vector of the nodal degrees of freedom and $\mathbf{f}(\mathbf{q})$ is a vector of nonlinear functions that represent the internal forces corresponding to the global degrees of freedom $\mathbf{q}$.

The body force term due to the acceleration of the mass in the equilibrium equation is expressed as

$$\int_V \delta\mathbf{u}^{\mathrm{T}}\ddot{\mathbf{u}}\rho dV = \sum \delta\mathbf{q}_e^{\mathrm{T}}\mathbf{M}_e\ddot{\mathbf{q}}_e \qquad (4.44)$$

where the element mass matrix is

$$\mathbf{M}_e = \int_{V_e} \mathbf{N}\mathbf{N}\rho dV \qquad (4.45)$$

Assembled over all the elements, the body force term is expressed as

$$\int_V \delta\mathbf{u}^{\mathrm{T}}\ddot{\mathbf{u}}\rho dV = \delta\mathbf{q}^{\mathrm{T}}\mathbf{M}\ddot{\mathbf{q}} \qquad (4.46)$$

where $\mathbf{M}$ is the global mass matrix.

61

4.5 *Dynamic Implicit Scheme*

Using equations (4.43) and (4.46), the equilibrium equation for dynamic problems can be symbolically written as

$$\delta\mathbf{q}^{\mathrm{T}}\left(\mathbf{f}(\mathbf{q})+\mathbf{M}\ddot{\mathbf{q}}-\mathbf{Q}\right)=0 \tag{4.47}$$

where the $\delta\mathbf{q}$ is the virtual global vector of the nodal degrees of freedom and $\mathbf{f}(\mathbf{q})$ is a vector of nonlinear functions that represent the internal forces corresponding to the global nodal degrees of freedom $\mathbf{q}$, $\mathbf{M}$ is a global mass matrix and $\mathbf{Q}$ is the applied load vector. For an arbitrary vector $\delta\mathbf{q}$, the equilibrium equation can be rewritten as

$$\mathbf{f}(\mathbf{q})+\mathbf{M}\ddot{\mathbf{q}}=\mathbf{Q} \tag{4.48}$$

For the dynamic formulation, time is represented by discrete time steps as

$$t_{n+1}=t_{n}+\Delta t \tag{4.49}$$

The displacement, velocity and acceleration vectors at time $t=t_{n}$ are written as

$$\mathbf{q}_{n}=\mathbf{q}(t_{n}),\ \dot{\mathbf{q}}_{n}=\dot{\mathbf{q}}(t_{n}),\ \ddot{\mathbf{q}}_{n}=\ddot{\mathbf{q}}(t_{n}) \tag{4.50}$$

It is assumed that these vectors are known and satisfy the equilibrium equation at time $t = t_n$. One can use the implicit scheme such as the trapezoidal rule for numerical integration in time, to determine the displacement and acceleration vectors that satisfy the equilibrium at time $t = t_{n+1}$ as

$$\mathbf{f}(\mathbf{q}_{n+1}) + \mathbf{M}\ddot{\mathbf{q}}_{n+1} = \mathbf{Q}_{n+1} \tag{4.51}$$

According to the trapezoidal rules, the unknown displacement and velocity vectors are assumed as follows:

$$\mathbf{q}_{n+1} = \mathbf{q}_n + \left(\frac{\dot{\mathbf{q}}_n + \dot{\mathbf{q}}_{n+1}}{2}\right)\Delta t \tag{4.52}$$

$$\dot{\mathbf{q}}_{n+1} = \dot{\mathbf{q}}_n + \left(\frac{\ddot{\mathbf{q}}_n + \ddot{\mathbf{q}}_{n+1}}{2}\right)\Delta t \tag{4.53}$$

Plugging equation(4.53) into equation(4.52), the displacement vector at time $t = t_{n+1}$ is rewritten as

$$\mathbf{q}_{n+1} = \mathbf{q}_n + \frac{\Delta t}{2}\left(2\dot{\mathbf{q}}_n + \frac{\Delta t}{2}(\ddot{\mathbf{q}}_n + \ddot{\mathbf{q}}_{n+1})\right) \tag{4.54}$$

The acceleration vector at time $t = t_{n+1}$ is obtained through some mathematical manipulation of equation (4.54) as

$$\ddot{\mathbf{q}}_{n+1} = \frac{4}{(\Delta t)^2}\left(\mathbf{q}_{n+1} - \mathbf{q}_n\right) - \frac{4}{(\Delta t)^2}\dot{\mathbf{q}}_n - \ddot{\mathbf{q}}_n \tag{4.55}$$

where $\ddot{\mathbf{q}}_{n+1}$ is a function of the unknown $\mathbf{q}_{n+1}$. Using the implicit scheme, the equilibrium equation in (4.51) becomes a nonlinear algebraic equation for the unknown vector $\mathbf{q}_{n+1}$.

The unknown vector $\mathbf{q}_{n+1}$ can be determined in an iterative fashion. One can express the equilibrium equation satisfied at (i+1)-th iteration as

$$\mathbf{f}(^{(i+1)}\mathbf{q}_{n+1}) + \mathbf{M}\,^{(i+1)}\ddot{\mathbf{q}}_{n+1} = \mathbf{Q}_{n+1} \tag{4.56}$$

where the left superscript represent the iteration number, and the displacement and acceleration vectors are expressed in an incremental form as

$$\begin{aligned}
^{(i+1)}\mathbf{q}_{n+1} &= {}^{(i)}\mathbf{q}_{n+1} + \Delta\mathbf{q} \\
^{(i+1)}\ddot{\mathbf{q}}_{n+1} &= {}^{(i)}\ddot{\mathbf{q}}_{n+1} + \Delta\ddot{\mathbf{q}}
\end{aligned} \tag{4.57}$$

Using equation (4.57), the equilibrium equation can be written in an incremental form as

$$\mathbf{f}(^{(i)}\mathbf{q}_{n+1}) + {}^{(i)}\!\left(\frac{\partial\mathbf{f}}{\partial\mathbf{q}_{n+1}}\right)\Delta\mathbf{q} + \mathbf{M}(^{(i)}\ddot{\mathbf{q}}_{n+1} + \Delta\ddot{\mathbf{q}}) = \mathbf{Q}_{n+1} \tag{4.58}$$

where $\left(\dfrac{\partial \mathbf{f}}{\partial \mathbf{q}_{n+1}}\right)^{(i)}$ corresponds to the tangential global stiffness matrix, $^{(i)}\mathbf{K}_{n+1}$ at the

i–th iteration. From equation (4.55), the following relationships are obtained.

$$\Delta\ddot{\mathbf{q}} = \frac{4}{(\Delta t)^2}\Delta\mathbf{q} \tag{4.59}$$

Plugging equation (4.59) into (4.58), one obtains a linear equation as

$$\left(^{(i)}\mathbf{K}_{n+1} + \frac{4}{(\Delta t)^2}\mathbf{M}\right)\Delta\mathbf{q} = \mathbf{Q}_{n+1} - \mathbf{f}(^{(i)}\mathbf{q}_{n+1}) - \mathbf{M}\,^{(i)}\ddot{\mathbf{q}}_{n+1} \tag{4.60}$$

where the right hand side of the equation corresponds to the dynamic imbalance. The increment $\Delta\mathbf{q}$ can be determined using the linear static solver. The displacement and acceleration vectors at the next iterations are updated using equations (4.57) and (4.59).

To start the first iteration for time $t = t_{n+1}$, the iteration number i is set to zero. Then, the equation (4.60) becomes

$$\left(^{(0)}\mathbf{K}_{n+1} + \frac{4}{(\Delta t)^2}\mathbf{M}\right)\Delta\mathbf{q} = \mathbf{Q}_{n+1} - \mathbf{f}(^{(0)}\mathbf{q}_{n+1}) - \mathbf{M}\,^{(0)}\ddot{\mathbf{q}}_{n+1} \tag{4.61}$$

where an initial guess for $^{(0)}\mathbf{q}_{n+1}$ is needed. Setting $^{(0)}\ddot{\mathbf{q}}_{n+1}$ to zero, one can find the

initial guess for $^{(0)}\mathbf{q}_{n+1}$ using equation (4.54) as

$$^{(0)}\mathbf{q}_{n+1} = \mathbf{q}_n + \frac{\Delta t}{2}\left(2\dot{\mathbf{q}}_n + \frac{\Delta t}{2}\ddot{\mathbf{q}}_n\right) \tag{4.62}$$

4.6 *Dynamic Failure Analysis*

Numerical procedure for the dynamic failure analysis is as follows:

1)   Start analysis to determine $\mathbf{q}_{n+1}$ at time $t = t_{n+1}$.

2)   Determine the time-dependent external load $\mathbf{Q}_{n+1}$ at time $t = t_{n+1}$. Use known

quantities $\mathbf{q}_n$, $\dot{\mathbf{q}}_n$, $\ddot{\mathbf{q}}_n$ at time $t = t_n$ to build the linear system of equations

provided in equation (4.60).

3)   Solve the linear system of equations and determine an incremental

displacement, $\Delta\mathbf{q}$.

4)   Update the displacement at time $t = t_{n+1}$ as

$$^{(i+1)}\mathbf{q}_{n+1} = {}^{(i)}\mathbf{q}_{n+1} + \Delta\mathbf{q} \tag{4.63}$$

and also update the entries in equation (4.60).

5)   Obtain the equilibrium state at time $t = t_{n+1}$ via repeating steps 3) and 4) until

$\Delta\mathbf{q}$ falls within a pre-defined tolerance.

6) Compute stresses at every integration point of elements and determine stresses at each composite layer in the ply directions or at each ceramic layer.

7) Determine if materials have failed or been damaged based on the proper failure criteria. Degrade material stiffness corresponding to the detected damage, if any. Repeat step 3) to 7) until no further damage occurs.

4.7 *Element Stiffness for Eighteen-Node Elements*

For the eighteen-node solid shell element, the element degrees of freedom vector $\mathbf{q}_e^{18}$ consists of nodal degrees of freedom as follows:

$$\mathbf{q}_e^{18} = \lfloor (u,v,w)_1 \quad \ldots \quad (u,v,w)_{18} \rfloor^{\mathrm{T}} \tag{4.64}$$

The nine-node element degrees of freedom vector $\mathbf{q}_e$ is related to the eighteen-node element degrees of freedom vector $\mathbf{q}_e^{18}$ as

$$\mathbf{q}_e = \mathbf{T}\mathbf{q}_e^{18} \tag{4.65}$$

where $\mathbf{T}$ is a transformation matrix based on equation (4.7). The detailed description of the matrix $\mathbf{T}$ is provided in Bin's work [51]. Using the transformation matrix in (4.65) and the element stiffness matrix $\mathbf{K}_e$ in equation (4.42), the element stiffness matrix for the eighteen-node elements $\mathbf{K}_e^{18}$ can be obtained as

$$\mathbf{K}_e^{18} = \mathbf{T}^{\mathrm{T}} \mathbf{K}_e \mathbf{T} \qquad\qquad (4.66)$$

Similarly, the element mass matrix and element load vector can be transformed from the nine-node counterparts.

4.8 *Multi-Frontal Parallel Solver*

To properly model the multi-layered structures, multiple elements are required through the thickness, increasing the problem size. The increased problem size would render the conventional skyline solver for the structural analysis impractically time-consuming. This is especially true for dynamic analyses that require a very small time step to guarantee the numerical convergence. In this study, a multi-frontal parallel solver, introduced by Scott [52], has been developed to efficiently solve the resulting linear systems of equations from the nonlinear solid shell element formulation. In this study, the single frontal solver, introduced by Orrigner [53], has been extended to a multi-frontal solver. The program code is written in Fortran 90. The solver makes use of Message Passing Interface, based on the interface software, Pooch developed by Decyk [54], to distribute the work tasks among the processors. The solver has been tested on a cluster of four G5 processors under Macintosh OS X. The computational time for the dynamic analyses has been roughly cut by a half.

Chapter 5 Numerical Tests

In this chapter, the effect of material damage and failure on the structural behavior of ceramic and composite panels is investigated, via carrying out the finite element analysis. First, structural analyses of Aluminum Nitride ceramic under the static and dynamic loading conditions are carried out using the ceramic damage model, introduced in Chapter 2. Subsequently, structural analyses of unidirectional and woven composite panels under the static and dynamic loading conditions are conducted using the composite failure models described in Chapter 3, and the resulting structural responses of the panels are validated in comparison with available experimental data. In addition, the structural behavior of a multi-layered composite armor with a ceramic layer under the blast wave pressure loading is investigated via conducting the finite element analysis. Subsequently, a modified armor design is proposed, and its structural performance is compared with that of the original design For the finite element modeling, the solid shell element formulation is used to describe the geometrically nonlinear and also materially nonlinear behavior of the ceramic and composite panels, and the dynamic analysis is carried out using the dynamic solution scheme described in Chapter 4.

5.1 Aluminum Nitride Ceramic Cube

In this section, the effect of lateral constraints on the failure behavior of the ceramic cube is investigated. A 0.01 meter long ceramic cube, subjected to pressure on one side and fixed at the opposite side, is considered as shown in Figure 5-1. Mechanical properties for Aluminum Nitride are provided in Table 1. The structural behavior of the ceramic cubes is examined with and without constraints in the lateral direction in the following subsections.

5.1.1 Without Lateral Constraints

In this example, the cube is free to expand in the lateral direction. First, nonlinear static analyses are carried out under the uniaxial compressive loading condition, and the load vs. the resulting maximum deflection of the ceramic cube is shown in Figure 5-2. The maximum displacement is linearly proportional to the pressure up to the collapse point, and the cube collapses in a brittle fashion. The collapse point, represented by the x-mark is very close to the quasi-static uniaxial compressive strength (Y_{QS}=2770 MPa), obtained from experiments. Subsequently, nonlinear dynamic analyses are carried out under a constant compressive loading. Figure 5-3 shows maximum displacement vs. time plot of the ceramic cube subjected to three load levels. For $P = 0.1$ GPa case, no damage is observed in the ceramic cube, the cube oscillates along time due to the inertia effect. For $P = 1.0$ GPa case, the ceramic cube catastrophically fails near 2 msec due to compressive failure. For $P = 3.0$ GPa case, the ceramic cube collapses as soon as it reaches equilibrium at the first time step. These results indicate that the ceramic cube fails in a brittle fashion

under the uniaxial static and dynamic loads. The failure occurs at lower load level under the dynamic loading condition.

5.1.2 With Lateral Constraints

The cube is now constrained in the lateral directions and only allowed for sliding in the loading direction, as shown in Figure 5-4. First, nonlinear static analyses are carried out under the uniaxial compressive loading condition, and the load vs. the resulting maximum deflection of the ceramic cube is shown in Figure 5-5. The maximum displacement is linearly proportional to the pressure when there is no material damage. As the pressure increases further, the maximum displacement increases more rapidly. Note that the cube does not catastrophically collapse at the initial failure, but gradually fails and collapses at the final failure under compression. The less brittle failure is qualitatively consistent with the observation made in the triaxial experiments. Subsequently, nonlinear dynamic analyses are carried out under the constant pressure loadings. Figure 5-6 shows maximum displacement vs. time plot of the ceramic cube subjected to three load levels. For the first two lower load levels, no material damage is observed. For $P = 3.0$ GPa case, the collapse of the ceramic cube is not as imminent as that of the laterally unconstrained cube. The lateral constraints increase the hydrostatic pressure in the cube, and increase material strength as a result, which is consistent with the pressure-dependent material behavior observed in the triaxial experiments.

5.2 *Aluminum Nitride Ceramic Panel*

A ceramic panel shown in Figure 5-7 is subjected to the uniform pressure on its top surface. The panel is clamped at two edges and free at the other two edges. The panel is made of Aluminum Nitride ceramic. Mechanical properties and geometry data are provided in Table 1 and Table 2. In addition to the flat panel shown in Figure 5-8, a low arched panel is also considered to investigate the effect of the curvature on the structural behavior of the panels under the pressure loading. Note that the arch length is very close to the length of the flat panel ($L_{arch}/L = 1.001$), and the weight increase due to the shape change is of little concern. Due to symmetry in loading and geometry, only one quarter of the panel is used for analyses. The panels are modeled using 8x8x2 eighteen-node elements.

5.2.1 Static Analyses

Nonlinear static analyses of the flat and arched panels are carried out under a constant transverse pressure. Figure 5-9 shows pressure vs. the displacement at the center of the flat and arched panels. For the flat panel, the displacement is approximately proportional to the pressure, and the panel collapses catastrophically at about $P = 0.2 \, \text{MPa}$. For the low arched panel, the failure occurs at a much higher pressure ($P = 1.0 \, \text{MPa}$), and it is rather gradual. This less brittle behavior can be attributed to the facts that the primary stress state in the low arch panels is compression and the compressive strength is much higher than the tensile strength in ceramics.

5.2.2 Blast Wave Model

A blast shock wave is modeled as a dynamic pressure loading on the top surface of the ceramic panel [55-56]. It is assumed that the pressure loading is uniform over the panel surface. The magnitude of the pressure loading, $P(t)$ is modeled using the Friedlander decay function as

$$P(t) = P_m (1 - \frac{t}{t_p}) \exp(-\alpha_p \frac{t}{t_p}) \tag{5.1}$$

where P_m is the magnitude of the pressure wave at time $t = 0$ and t_p, α_p are blast wave profile parameters that decide characteristics of the blast wave. Figure 5-10 shows the Friedlander function in non-dimensional form.

5.2.3 Dynamic Analyses

Nonlinear dynamic analyses of the flat and low arched panels under the blast wave pressure loading are carried out, with and without applying the ceramic damage model. The blast wave is modeled using Friedlander decay function parameters ($P_m = 1.065$ MPa, $t_p = 1.3$ msec, $\alpha = 1.7$). For the analysis, it is assumed that the pressure wave exists during the time span $0 \leq t \leq t_p$ and completely dies out after t_p.

For the flat panel, the resulting maximum displacements at the panel center are shown along time in Figure 5-11. The effect of the damage model on the structural response is evident; the center displacement at the first peak significantly increases and the time of the first peak is also significantly delayed. Figure 5-12

shows a side view of failed regions due to tensile failures for the quarter of the panel at two instants. The left end represents the clamped edge, and the right end corresponds to the panel center. As shown in Figure 5-12, the panel experiences tensile damages almost through the thickness at the clamped edge and center edge at $t = 3$ ms. Note that the panel is no longer under the pressure loading after $t = 1.3$ ms. Accordingly, the failure progresses little after $t = 3$ ms.

For the low arched panel, the resulting maximum displacements at the panel center are shown in Figure 5-13. The effect of the damage model on the structural response is not as evident around the first peak as the flat panel case. According to the failed region plot at $t = 2.1$ ms in Figure 5-14, the arched panel does not go through as much tensile failures as the flat one does. However, as the panel reverses its direction toward the first trough, the tensile failure progresses through the thickness at the left edge, as shown in Figure 5-14, and the panel structurally collapses. Therefore, the low arched design is beneficial only when the arch design remains close to its original configuration such as when it deforms under the static loading condition.

5.3 *Unidirectional Composites Panel*

5.3.1 Static Analyses

A static progressive failure analysis is carried out on an E-Glass/Polyester composite panel using the failure model for the unidirectional ply. The panel is clamped at all edges and subjected to uniform transverse pressure loading as shown in Figure 5-15. The mechanical properties of the E-Glass/Polyester ply are provided in Table 3. The lay-up sequence and thickness of the laminate are provided in Table 4.

74

For numerical analysis, experimental results as well as material properties and geometrical data are taken from Padhi et al [34]. According to their test data, the panel exhibits nonlinear responses and progressive damage as pressure increases, and the panel structurally collapses at pressure (P=0.605 MPa).

The full plate is modeled using 16x16 nine-node elements. To check the effect of non-symmetry due to the ply lay-up, the top-left quarter of the panel is also modeled using an 8x8 element mesh, and the analysis results are compared with the full plate model. Figure 5-16 shows pressure vs. transverse displacement at the panel center. For reference purpose, the analysis results obtained without applying the material damage model are provided (a full 20x20 mesh). As shown in the figure, the panel exhibits a geometrically nonlinear behavior without the damage effect. Note that a pressure increment of 0.01 MPa is used for the analyses, resulting in about 60 load steps.

In Figure 5-16, the effect of progressive failure on the structural behavior is clearly shown, and the analysis results are favorably compared with the experimental data by Padhi et al [34]. Numerical analyses fail to converge above 0.60 MPa, represented by the x-mark in Figure 5-16, indicating the onset of the structural collapse for the panel. This is also in good agreement with the experimentally observed failure at 0.605 MPa.

There is little difference in the pressure vs. displacement curves up to 0.15 MPa between the quarter model (8x8 mesh) and the full model (16x16 mesh), as shown in Figure 5-16. However, as the pressure increases, the difference in their predicted responses becomes more evident. At 0.6 MPa, the difference is about two

percents of the displacement. In addition, the collapse pressure predicted by the full model is different from the collapse pressure of the quarter model. This indicates that there is some effect of structural non-symmetry on the deformation of the plate as material failure spreads over the plate.

The progressive failure of the panel, observed experimentally by Padhi et al [34], is summarized as follows: The matrix cracking failures first appear along the clamped edges, characterized by the emitted noise, and spreads over the panel as the pressure increases. As the pressure increases further, fiber breakage failures along the edges are accompanied by very loud noises.

The test data in Figure 5-16 show two drastic changes in the deflection at around the pressure of 0.18 MPa and 0.46 MPa. Numerical results also predict the drastic changes in the deflection around the same pressure levels. For the quarter model results (8x8), another drastic change in the deflection is observed at the pressure of 0.63 MPa, indicating the onset of the structural collapse. For each pressure level, the failure regions and failure modes for the quarter model are shown in Figure 5-17. Each column in Figure 5-17 shows failure regions from top to bottom layers at a pressure level. Bottom-right corner represents the center of the panel. The grey patch represents the matrix cracking failure and the black patch represents the fiber breakage failure. As shown in the first two columns, the matrix cracking failures rapidly spread around the panel center in the 90 degree layer at 0.18 MPa. The rapid increase of the matrix cracking failures around the center accounts for the drastic change in the center deflection. As shown in the third and fourth columns, the fiber breakage failures occur in the edges of the bottom two layers for the first time at 0.46

76

MPa. This explains the drastic change in the deflection at the pressure. Finally, the fiber breakages spread through the thickness as shown in the last two columns, accompanied by the drastic change in the deflection. As the pressure increases further, the fiber breakages result in a structural collapse.

Pinpointing the collapse point using numerical analyses is challenging because the failure to find converged equilibrium can be numerical problems, not physical phenomena. Using fine meshes for the full plate (14x14 ~ 24x24), one may conduct convergence tests on the collapse point or at least the onset of the collapse point. As shown in Figure 5-18, their resulting response is very close to one another, except around the collapse point. It appears that the onset for the collapse point converges at 0.58 MPa as the mesh becomes finer (22x22, 24x24), as shown in Figure 5-19.

5.3.2 Dynamic Analyses

The clamped square composite panel is revisited, and the panel is subjected to a blast shock wave. The plate geometry, ply lay-up sequence and material properties are identical to those in the previous static example. Dynamic analyses are conducted on the top-left quarter of the plate, as shown in Figure 5-20, using the 8x8 mesh to save the computational time. The Friedlander decay function in equation (5.1) is used to model the blast wave loading. Two different levels of blast wave are considered: the Friedlander parameters are $P_m = 0.2$ (MPa), $t_p = 1.8$ (msec), $\alpha = 0.35$ for case 1, and the initial pressure magnitude is increased to $P_m = 1.0$ (MPa) for case 2. For both analyses, the time increment of 0.25×10^{-4} second is used. Figure 5-21 and Figure

5-22 show the resulting center displacements due to the progressive failure effect corresponding to the two different pressures.

In Figure 5-21, the dotted curve represents the analysis results with no failure effect and the solid curve represents the analysis results with the progressive failure effect. It is observed that the progressive failure effect on the structural behavior is not very significant in the initial stage prior to the first peak. The first peak for the case with no failure is 33.7 mm while the first peak for the case with failure is 35.4 mm. As observed in the dotted curves of Figure 5-21 and Figure 5-22, the first peak occurs faster for higher level of pressure, mainly because of the increased stiffness due to the geometrically nonlinear effect.

For case 2, as shown in Figure 5-22, the panel structurally collapses before it even reaches the first peak, irrespective of the time increments. The pressure at the structural collapse is about 0.37 MPa. The collapse pressure is lower than the collapse pressure of the static case due to the dynamic effect.

Figure 5-23 shows how material failures propagate in the bottom ply (0 degree) along time for P_m =1.0 MPa case. The region shown in the figure is the top-left quarter of the plate with the center located at the right-bottom corner. It is observed that the failure starts from the upper edge where the failure is dominated by the matrix cracking failures, represented by a grey square mark. The failed region grows toward the left side edge and plate center. At and around the plate center, a separate region of matrix cracking failure develops and grows. The fiber breakage failure starts from the left side edge and grows along the other edges. It is well to point out that, for the present case, the analysis considering material damage fails to

converge even before the first peak is reached, indicating the collapse of the structure. This phenomenon cannot be predicted unless material damage effect is incorporated into the analysis.

5.4 *Woven Composite Panels*

A dynamic analysis is conducted on a square woven composite plate subjected to the blast wave pressure loading. The pressure is applied on the bottom surface of the plate. The plate, clamped along two opposite edges and free along the remaining two edges, is 914 mm long, 914 mm wide and 9.525 mm thick. The ply is a woven fabric made of S-2 Glass fiber/Epoxy resin, and its mechanical properties, lay-up sequence for the fifteen layers and strain-rate effect constants are provided in Table 5 - Table 7.

Impact tests on the plate subjected to the blast shock wave were carried out. In the tests, the TNT-standard blast loading module was used to calculate the blast pressure time history on the selected points on the plate. Two different tests have been conducted. For both tests, it is assumed that the pressure waves exist during the time span of $0 < t \le t_p$. For time t greater than t_p, P_m is equal to 0. The parameters for the description of the blast loadings are, for the first loading case, P_m=1.065 MPa, t_p=1.3 msec, α=1.7 and, for the second loading case, P_m=3.10 MPa, t_p=1.2 msec, α=2.15.

Due to the symmetry in geometry and loading, a top-left quarter of the plate is used for the finite element analysis. Figure 5-24 show the center displacement vs.

time for the first loading case. Figure 5-25 shows the growth of the failed regions on the bottom two plies and the top two plies as time elapses. As shown in Figure 5-25, material damages are observed only in the bottom two layers at the first peak as they are under compression and the material has lower strength in compression. At the first trough, the stress state is switched and the top two layers fail under compression.

Figure 5-26 shows the center displacement vs. time when P_m increases to 3.1 MPa. The first peak almost doubles from the previous case and it occurs faster due to the geometrically nonlinear effect. As shown in Figure 5-27, material failures are observed in both bottom and top layers before the first peak (0.8 ms). The bottom layers experience more damages because they are under compression. After the first peak, more damages are observed in the top layers (1.6 ms).

Figure 5-28 shows maximum displacement at the plate center vs. impulse. In the figure, numerically obtained values are compared with the available test data. For the lower impulse loading (0.41 MPa-ms, Test 1), the numerical analysis slightly under-predicts the displacement while, for the higher impulse loading (1.02 MPa-ms, Test 2), numerical values falls inside the band of the experimental result. Figure 5-28 also includes numerically obtained results for two additional analyses, carried out for impulse loadings of 0.2 MPa-ms and 0.7 MPa-ms. The blast wave parameters for these loadings are, P_m=0.504 MPa, t_p=1.3 msec, α=1.7 and P_m=2.129 MPa, t_p=1.2 msec, α=2.15, respectively.

5.5 *Dynamic Analyses of Ceramic Armor Panels*

In this section, dynamic response of Aluminum Nitride (AlN) core sandwich panels under the blast wave pressure loading is investigated via conducting the finite element analysis. First, the effect of wrapping a ceramic panel with composite laminates, on the structural behavior is examined. Subsequently, the structural behavior of an armor design, tailored for penetration resistance, is investigated under the blast wave pressure loading. Lastly, a modified armor design is proposed, and its structural performance is compared with that of the original design.

5.5.1 Wrapped Ceramic Panels

The flat and low-arched sandwich panels in Figure 5-29 are subjected to the uniform transverse pressure on their top surface. Aluminum Nitride ceramic is used as the core material and two identical Graphite/Epoxy laminates are used as the skin material. Mechanical properties, lay-up sequence and thickness of Graphite/Epoxy plies are provided in Table 8 - Table 10. For the Graphite/Epoxy laminates, the strain-rate dependent transverse strength defined in equation (3.21) is expressed as a log function of the strain-rate as

$$Y = Y_{QS}(1 + 0.02 \times \log \frac{\dot{\varepsilon}_{22}}{\dot{\varepsilon}_{ref}}) \tag{5.2}$$

where $\dot{\varepsilon}_{ref}$ is a reference strain-rate.

Geometry of the ceramic panel and boundary conditions are shown in Figure 5-7. Due to the symmetry in geometry and loading, only the top-left quarter of the panel is used for analyses. Aluminum Nitride is assumed isotropic, but fictitious layers are introduced through thickness to facilitate layer-wise damage analyses. The blast wave loading is modeled as a dynamic uniform pressure loading via using the Friedlander function parameters identical to the previous unwrapped cases ($P_m = 1.065$ MPa, $t_p = 1.3$ msec, $\alpha = 1.7$).

For the flat panel, the resulting maximum displacements at the panel center and failed regions are shown along time in Figure 5-30, in comparison with those of the ceramic panel without wrappings. The effect of wrapping on the structural response is evident; the center displacement at the first peak significantly decreases and the first peak is also not as significantly delayed as the unwrapped case. However, the wrapping material, Graphite/Epoxy laminate, almost fails at the clamped edge while it remains intact at the panel center at 6 ms, indicating that there exists little advantage over the unwrapped design.

For the arched panel, the resulting maximum displacements at the panel center and failed regions are shown along time in Figure 5-31, also in comparison with those of the unwrapped ceramic panel. The effect of wrapping on the structural response is not as evident as the previous flat panel case; the center displacement at the first peak only slightly decreases, and there exists little difference in their response up to the collapse point. It is observed that materials remain intact around the panel center irrespective of wrapping or no wrapping while extensive damage occurs at the clamped edge through the thickness.

A different boundary condition that allows sliding at the left edge, as shown in Figure 5-32, is considered in an attempt to relieve stresses at the clamped edge. The resulting maximum displacement at the panel center and failed regions are shown along time in Figure 5-33. It appears that the sliding boundary conditions somewhat relieve stress at the clamped edge, and as a result, material damages spread over the panel. However, wrapped or not, the arched panels collapse before they even reach the first peak because the first peak increases from 3.5 mm to 6 mm under the sliding boundary condition for the wrapped case. This indicates that the clamping of the plate edge is necessary to obtain good blast resistance via substantially reducing the deflection.

5.5.2 Wrapped Ceramic Panels with a Back-Plate

A multi-layered square panel in Figure 5-34 is subjected to the uniform pressure on its top surface. The multi-layered panel is comprised of two parts as shown in the lower diagram of Figure 5-34. The upper part is the Aluminum Nitride core sandwich that directly faces the blast wave pressure loading on its top surface. The lower part is a back plate attached to the sandwich to provide structural integrity. The back plate is made of woven fabric Glass/Epoxy laminates. Mechanical properties, lay-up sequence for the twenty four layers and geometry data of the woven composite are provided in Table 5 - Table 7. Due to the symmetry in geometry and loading, only a quarter of the panel is used for analyses, shown as a shaded area in Figure 5-34.

A blast shock wave is modeled as a dynamic uniform pressure loading on the top surface of the target panel. Four different blast wave profiles are considered, and the three Friedlander parameters corresponding to each blast wave profile are provided in Table 11. Figure 5-35 shows the four blast wave profiles. Impulse is often used to describe the load level of the applied shock wave. Table 11 lists the impulse for each profile obtained via integrating the pressure profile.

For the stiffness degradation model, a small number md, introduced in equation (3.9), is used to avoid potential numerical instabilities. For the ceramic damage model, the damage parameter is modified via subtracting md as

$$D = D - md \qquad\qquad (5.3)$$

Accordingly, the damage parameter D is very close to one at failure, but always smaller than 1. For analyses, $md = 1.0 \times 10^{-6}$ is used.

Using the 8x8x6z mesh and the time step ($\Delta t = 3 \ (\mu s)$), dynamic analyses of the armor panel are carried out with and without applying the damage and failure models under the first four blast-wave loading conditions. Figure 5-36 - Figure 5-39 show the resulting dynamic deflection at the panel center vs. time and failed regions at an instant. For case I, the effect of material damage on the structural response is not significant as shown in Figure 5-36. For case II, the peak deflection increases and lags in time when the damage and failure models are applied, as shown in Figure 5-37. In addition, the amplitude of maximum displacement at the first trough is greater than the amplitude at the first peak, indicating increased effect of the material damage on

84

the structural behavior. As the impulse of the blast wave increases further, failure or damage of panels causes higher and delayed peak deflections, as shown in Figure 5-38. For case IV, the panel structurally collapses before it reaches the peak deflection, as shown in Figure 5-39. The maximum deflections at the first peak are provided in Table 12.

5.5.3 Wrapped Ceramic Panels with Front and Back-Plates

The armor design shown in Figure 5-34 is modified via splitting the back-plate into two plates and attaching one of them onto the top of the sandwich armor, as shown in Figure 5-40. Accordingly, the weight of the modified armor panel is identical to the original armor panel. Dynamic analyses are carried out with and without applying the damage and failure models for the four blast loading cases. The resulting dynamic responses and failed regions are shown from Figure 5-41 to Figure 5-44.

For case I, it appears that there is no obvious advantage of using the modified design against the original design; the maximum displacement at the first peaks in Figure 5-36 and Figure 5-41 are close to each other, and the first peaks occurs at about 1.5 ms. The difference between amplitudes at the first peak and trough in Figure 5-41 is less than that of Figure 5-36, which indicates that the material damage in the ceramic plate affects the structural behavior less in the modified design. This is true even though the material damage for ceramic plates in the modified design is more severe than that in the original design.

For case II, the advantage of using the modified design becomes more pronounced; the amplitude at the first trough does not significantly increase from the amplitude at the first peak, as shown in Figure 5-42. Recall that there is a significant increase in the amplitude at the first trough for the original design, as shown in Figure 5-37. The front and back plates remain intact at 6 ms, as shown in Figure 5-42, while the top skin in the original design experiences material damages at the clamped edge and center, as shown in Figure 5-37.

For case III, the advantage of using the modified design becomes even more pronounced. As shown in Figure 5-43, the front and back plates remain almost intact at 6 ms while the back plate in the original design suffers from material damages, as shown in Figure 5-38. For case IV, the modified design structurally collapses before it reaches the first peak, as shown in Figure 5-44.

Chapter 6 Conclusions and Recommendations for Future Work

6.1 *Conclusions*

A damage model for ceramic materials has been developed and incorporated into the geometrically nonlinear solid shell element formulation for dynamic analyses of multi-layered ceramic armor panels under blast wave pressure loading condition. The ceramic damage model is based on the local stress state. Accordingly, it can describe dynamic failure mechanisms of ceramics regardless of their configurations and loading rates. A two-surface damage model is introduced to takes into account the pressure-dependent behaviors of ceramics under compression. Damage accumulation depends on the prior damage states as well as the current stress state. In addition, the effect of strain-rates on the material strengths is incorporated into the damage model.

The previous composite failure model is modified into two separate failure models to address different failure mechanisms in the unidirectional and woven composites. Accordingly, two separate stiffness degradation models for the

unidirectional and woven composites are introduced. In addition, the effect of strain-rates on the material strengths is incorporated into the composite failure models.

The newly developed ceramic damage model and modified composite failure models are incorporated into the geometrically nonlinear solid shell element formulation for dynamic problems. The effect of material damage and failure on the structural behavior of ceramic panels and composite panels is investigated, via conducting the finite element analysis under the static and dynamic loading conditions. The developed ceramic damage model and composite failure models are validated in comparison with available experimental data.

The dynamic response of a multi-layered Aluminum Nitride core sandwich armor panel under the blast wave pressure loading is investigated via conducting the finite element analysis. The multi-layered armor panel, tailored for penetration resistance, is comprised of an Aluminum Nitride core sandwich with unidirectional Graphite/Epoxy skins and a woven S-2 Glass/Epoxy back-plate. Multiple eighteen-node elements are used through the thickness to properly describe the mechanics of the multi-layered panel. For the finite element analysis, the geometrically nonlinear solid shell element formulation for dynamic problems is used in conjunction with the material damage and failure models for the ceramic and composite layers. The resulting dynamic responses of the panel demonstrate that dynamic analyses that do not take into account material damage of failure models significantly under-predict the first peak displacement. The under-prediction becomes more pronounced as the blast load level increases. As the blast load level increases further, the panel suffers a

structural failure due to material failures on the clamped edges and tensile failure mode is dominant in the ceramic layer.

An equally weighted armor design is proposed via splitting the back-plate into two plates and attaching one of them onto the top of the sandwich armor. The geometrically nonlinear analyses of the armor panel are carried out under the blast wave loading condition. The resulting dynamic response shows that the amplitudes of the modified design do not grow over time as significantly as those of the original design, indicating better performance of the modified design against the blast shock wave. This exercise clearly demonstrates the capability of the present analytical methodology to determine dynamic response of multi-layered sandwich armor panels for a design study.

6.2 *Contribution of the Present Work*

Even though mainly used to predict multi-axial phenomena, existing damage models for ceramics have been developed based on the uniaxial impact tests. Recent advances in multi-axial experimental techniques have enabled better understanding of the ceramic material behavior under the multi-axial loading condition. The present work provides the first ceramic damage model that directly reflects the multi-axial phenomena based on observations made from the triaxial test.

6.3 *Recommendations for Future Works*

Among commercially available ceramics, Alumina has been of the greatest interest to armor designs because it provides moderate level of material strengths at relatively small cost. However, due to the lack of required experimental data, the developed damage model could not be applied to Alumina. Accordingly, triaxial tests on Alumina specimen are recommended for future work. The triaxial tests must be performed at various loading-rates in order to obtain material parameters required for the present damage model for ceramic materials.

Also, according to the numerical results provided in Chapter 5, for flat and low-arched panels, tensile failure mode is dominant in the ceramic layer under the blast wave pressure loading. Accordingly, it is recommended that the future work include investigation of alternative panel designs to take advantage of the behavior of ceramic layers under compression.

Survivability under extreme loading conditions such as blast shock wave and ballistic impact is one of the most important factors in armor design. This study focuses only on the survivability of the armor panel under blast shock wave. Accordingly, it is recommended that future work extend the analytical methodology to the analysis of the armor panel under ballistic impact.

Appendix A. Mapping and Shape Functions

For the nine-node element, the mapping functions $N_i(\xi,\eta)$ in equation (4.4) are as follows:

$$N_1 = \frac{1}{4}\xi(1+\xi)\eta(1+\eta)$$

$$N_2 = \frac{1}{2}(1+\xi)(1-\xi)\eta(1+\eta)$$

$$N_3 = -\frac{1}{4}\xi(1-\xi)\eta(1+\eta)$$

$$N_4 = -\frac{1}{2}\xi(1-\xi)(1+\eta)(1-\eta)$$

$$N_5 = \frac{1}{4}\xi(1-\xi)\eta(1-\eta) \qquad\qquad \text{(A.1)}$$

$$N_6 = -\frac{1}{2}(1+\xi)(1-\xi)\eta(1-\eta)$$

$$N_7 = -\frac{1}{4}\xi(1+\xi)\eta(1-\eta)$$

$$N_8 = \frac{1}{2}\xi(1+\xi)(1+\eta)(1-\eta)$$

$$N_9 = (1+\xi)(1-\xi)(1+\eta)(1-\eta)$$

where the original of the parental coordinates and the node numbering are shown in Figure 4-2. Note that the shape functions in equation (4.8) are identical to the mapping functions for an isoparametric element.

Appendix B. Stress-Strain Relation

For general three-dimensional solids, the strain-stress relation for isotropic and orthotropic materials is expressed as

$$\boldsymbol{\varepsilon} = \mathbf{S}\boldsymbol{\sigma} \tag{B.1}$$

where $\mathbf{S}$ is the compliant matrix. For example, the transverse normal strain ε_{zz} is expressed as

$$\varepsilon_{zz} = S_{31}\sigma_{xx} + S_{32}\sigma_{yy} + S_{33}\sigma_{zz} \tag{B.2}$$

where S_{ij} is the i-th row and j-th column entry of the compliant matrix. For thin structures, the normal strain is very close to zero. The conventional degenerated shells reduce the matrix $\mathbf{S}$ by removing the third row and column.

Solid shell elements assume a linear shear deformation through the thickness and a constant thickness change. The constitutive equations must be properly modified to represent the assumed behavior of solid shell elements. To decouple the in-plane normal stresses from the out-of-plane normal stress, the equation (B.2) is replaced by an artificial strain-stress relation as

$$\varepsilon_{zz} = S_{33}\sigma_{zz} \tag{B.3}$$

where the in-plane stresses σ_{xx}, σ_{yy} do not affect the transverse normal strain. In addition, the effect of the transverse normal stress σ_{zz} on other in-plane stresses σ_{xx}, σ_{yy} is ignored via setting the following condition:

$$S_{13} = 0, \quad S_{23} = 0 \tag{B.4}$$

Inversing the modified compliant matrix, one can obtain a modified $\mathbf{C}_e$ matrix for isotropic materials as

$$\mathbf{C}_e = \begin{bmatrix} \dfrac{E}{1-v^2} & \dfrac{vE}{1-v^2} & 0 & 0 & 0 & 0 \\[2mm] \dfrac{vE}{1-v^2} & \dfrac{E}{1-v^2} & 0 & 0 & 0 & 0 \\[2mm] 0 & 0 & E & 0 & 0 & 0 \\[2mm] 0 & 0 & 0 & G & 0 & 0 \\[2mm] 0 & 0 & 0 & 0 & \beta G & 0 \\[2mm] 0 & 0 & 0 & 0 & 0 & \beta G \end{bmatrix} \tag{B.5}$$

where E is Young's modulus, v is Poisson's ratio, G is shear modulus and $\beta = 5/6$ is a shear correction factor. For orthotropic materials, the modified $\mathbf{C}_e$ matrix is expressed as

$$\mathbf{C}_e = \begin{bmatrix} \dfrac{E_1}{1-v_{12}v_{21}} & \dfrac{v_{21}E_1}{1-v_{12}v_{21}} & 0 & 0 & 0 & 0 \\[2mm] \dfrac{v_{12}E_2}{1-v_{12}v_{21}} & \dfrac{E_2}{1-v_{12}v_{21}} & 0 & 0 & 0 & 0 \\[2mm] 0 & 0 & E_3 & 0 & 0 & 0 \\[2mm] 0 & 0 & 0 & G_{12} & 0 & 0 \\[2mm] 0 & 0 & 0 & 0 & \beta G_{23} & 0 \\[2mm] 0 & 0 & 0 & 0 & 0 & \beta G_{31} \end{bmatrix} \tag{B.6}$$

For relatively thick panels, multiple solid shell elements can be used to model the high-order deformation through the thickness. The artificial strain-stress relation

imposed for thin structures is not valid any more. The fully three-dimensional constitutive equations must be used. For isotropic materials, the full $\mathbf{C}_e$ is written as

$$\mathbf{C}_e = \frac{E}{(1+v)(1-2v)}\begin{bmatrix} 1-v & v & v & 0 & 0 & 0 \\ v & 1-v & v & 0 & 0 & 0 \\ v & v & 1-v & 0 & 0 & 0 \\ 0 & 0 & 0 & \dfrac{1-v}{2} & 0 & 0 \\ 0 & 0 & 0 & 0 & \dfrac{1-2v}{2} & 0 \\ 0 & 0 & 0 & 0 & 0 & \dfrac{1-2v}{2} \end{bmatrix} \tag{B.7}$$

For orthotropic materials, the full $\mathbf{C}_e$ is written as

$$\mathbf{C}_e = \begin{bmatrix} \dfrac{1-v_{23}v_{32}}{E_2 E_3 \Delta_e} & \dfrac{v_{21}+v_{31}v_{23}}{E_2 E_3 \Delta_e} & \dfrac{v_{31}+v_{21}v_{32}}{E_2 E_3 \Delta_e} & 0 & 0 & 0 \\ \dfrac{v_{12}+v_{13}v_{32}}{E_3 E_1 \Delta_e} & \dfrac{1-v_{31}v_{13}}{E_3 E_1 \Delta_e} & \dfrac{v_{32}+v_{31}v_{12}}{E_3 E_1 \Delta_e} & 0 & 0 & 0 \\ \dfrac{v_{13}+v_{12}v_{23}}{E_1 E_2 \Delta_e} & \dfrac{v_{23}+v_{13}v_{21}}{E_1 E_2 \Delta_e} & \dfrac{1-v_{12}v_{21}}{E_1 E_2 \Delta_e} & 0 & 0 & 0 \\ 0 & 0 & 0 & G_{12} & 0 & 0 \\ 0 & 0 & 0 & 0 & G_{23} & 0 \\ 0 & 0 & 0 & 0 & 0 & G_{31} \end{bmatrix} \tag{B.8}$$

where

$$\Delta_e = \frac{1-v_{12}v_{21}-v_{23}v_{32}-v_{31}v_{13}-2v_{12}v_{23}v_{31}}{E_1 E_2 E_3} \tag{B.9}$$

Tables

Table 1: Mechanical properties of Aluminum Nitride (AlN)

Material Properties	Value
Young's Modulus, E_x (GPa)	315.0
Poisson's Ratio, ν	0.237
Density, ρ (kg/m^3)	3200
Quasi-static Tensile Strength, X_{QS} (MPa)	320.0
Quasi-static Compressive Strength, Y_{QS} (MPa)	2777.5
Pressure-independent Shear Strength, τ_f (MPa)	3500
Pressure-dependent strength parameter, α	0.96468
Pressure-dependent strength parameter, B_1	3004.4
Pressure-dependent strength parameter, B_2	1.0115e-4

Table 2: Fictitious number of layers and thickness for Aluminum Nitride plate

Number of Plies (fictitious)	Thickness, t (mm)
24	19.05

Table 3: Mechanical properties of unidirectional E-Glass/Polyester ply

Material Properties	Value
Longitudinal Modulus, E_x (GPa)	23.6
Transverse Modulus, $E_y = E_z$ (GPa)	10.0
Shear Modulus, $G_{xy} = G_{xz}$ (GPa)	1.0
Shear Modulus, G_{yz} (GPa)	1.0
Poisson's Ratio, $\nu_{xy} = \nu_{xz}$	0.23
Poisson's Ratio, ν_{yz}	0.30
Density, ρ (kg/m^3)	1500
Longitudinal Tensile Strength, X_T (MPa)	735.0
Longitudinal Compressive Strength, X_C (MPa)	600.0
Transverse Tensile Strength, Y_T (MPa)	45.0
Transverse Compressive Strength, Y_C (MPa)	100.0
In-Plane Shear Strength, SC (MPa)	45.0

Table 4: Lay-up sequence and thickness of unidirectional E-Glass/Polyester laminated composite plates

Lay-up Sequence	Number of Plies	Thickness, t (mm)
$[0/45/90/-45/0]$	5	3.43

Table 5: Mechanical properties of woven fabric S-2 Glass/Epoxy ply

Material Properties	Value
Longitudinal Modulus, E_x (GPa)	28.3
Transverse Modulus, E_y (GPa)	28.3
Shear Modulus, G_{xy} (GPa)	5.86
Poisson's Ratio, ν_{xy}	0.23
Density, ρ (kg/m^3)	1800
Quasi-static Longitudinal Tensile Strength, X_T^{QS} (MPa)	583.12
Quasi-static Longitudinal Compressive Strength, X_C^{QS} (MPa)	402.12
Quasi-static Transverse Tensile Strength, Y_T^{QS} (MPa)	583.12
Quasi-static Transverse Compressive Strength, Y_C^{QS} (MPa)	402.12
Quasi-static In-Plane Shear Strength, SC^{QS} (MPa)	95.06

Table 6: Strain-rate dependent strength properties of woven fabric S-2 Glass/Epoxy ply

Longitudinal Tensile Strength, X_T (MPa)	$X_T = 48.16 \log_{10} \dot{\varepsilon}_{11} + X_T^{QS} + 144.48$
Longitudinal Compressive Strength, X_C (MPa)	$X_C = 48.16 \log_{10} \dot{\varepsilon}_{11} + X_C^{QS} + 144.48$
Transverse Tensile Strength, Y_T (MPa)	$Y_T = 48.16 \log_{10} \dot{\varepsilon}_{22} + Y_T^{QS} + 144.48$
Transverse Compressive Strength, Y_C (MPa)	$Y_C = 48.16 \log_{10} \dot{\varepsilon}_{22} + Y_C^{QS} + 144.48$
In-Plane Shear Strength, SC (MPa)	$SC = 8.08 \log_{10} \dot{\varepsilon}_{12} + SC^{QS} + 24.24$

Table 7: Lay-up sequence and thickness of S-2 Glass/Epoxy laminated composite plates

Lay-up Sequence	Number of Plies	Thickness, t (mm)
$(0,45,0,45,0)_3$	15	9.525
$(0/45)_{6S}$	24	15.24

Table 8: Mechanical properties of unidirectional Graphite/Epoxy (IM7/8551) ply

Material Properties	Value
Longitudinal Modulus, E_x (GPa)	50.1
Transverse Modulus, $E_y = E_z$ (GPa)	3.54
Shear Modulus, $G_{xy} = G_{xz}$ (GPa)	1.61
Shear Modulus, G_{yz} (GPa)	1.22
Poisson's Ratio, $\nu_{xy} = \nu_{xz}$	0.32
Poisson's Ratio, ν_{yz}	0.45
Density, ρ (kg/m^3)	1500
Quasi-static Longitudinal Tensile Strength, X_T^{QS} (MPa)	858.99
Quasi-static Longitudinal Compressive Strength, X_C^{QS} (MPa)	515.40
Quasi-static Transverse Tensile Strength, Y_T^{QS} (MPa)	23.84
Quasi-static Transverse Compressive Strength, Y_C^{QS} (MPa)	53.69
Quasi-static In-Plane Shear Strength, SC^{QS} (MPa)	25.77

Table 9: Strain-rate dependent strength properties of IM7/8551 ply

Longitudinal Tensile Strength, X_T (MPa)	$X_T \approx X_T^{QS}$
Longitudinal Compressive Strength, X_C (MPa)	$X_C \approx X_C^{QS}$
Transverse Tensile Strength, Y_T (MPa)	$Y_T = Y_T^{QS}(1.0 + 0.02 \times \log\frac{\dot{\varepsilon}_{22}}{\dot{\varepsilon}_{ref}})$
Transverse Compressive Strength, Y_C (MPa)	$Y_C = Y_C^{QS}(1.0 + 0.02 \times \log\frac{\dot{\varepsilon}_{22}}{\dot{\varepsilon}_{ref}})$
In-Plane Shear Strength, SC (MPa)	$SC \approx SC^{QS}$
The Reference Strain-Rate, $\dot{\varepsilon}_{ref}$ (1/sec)	1.0×10^{-4}

Table 10: Lay-up sequence and thickness of IM7/8551 laminated composite plates

Lay-up Sequence	Number of Plies	Thickness, t (mm)
$[0/45/90/-45]_{3S}$	24	3.175

Table 11: Three parameters for four blast wave pressure loadings, and impulses

Profile	P_m (MPa)	α_P	t_P (Sec)	Impulse, I (MPa-ms)
I	1.065	1.7	0.0013	0.429
II	3.1	2.15	0.0012	1.0192
III	5.0	2.15	0.0012	1.6439
IV	10.0	2.15	0.0012	3.2878

Table 12: The first peak of max dynamic deflection (mm) at the center for a clamped-free panel

Profile	I	II	III
Max deflection At the first peak	−3.03	−9.47	−17.69

Figures

P_o : Lateral pressure

$\sigma = Y_C$ at Failure

Specimen

ϕ

ϕ: specimen
diameter

Sleeve

$\phi - \delta$

δ: misfit

Assembly
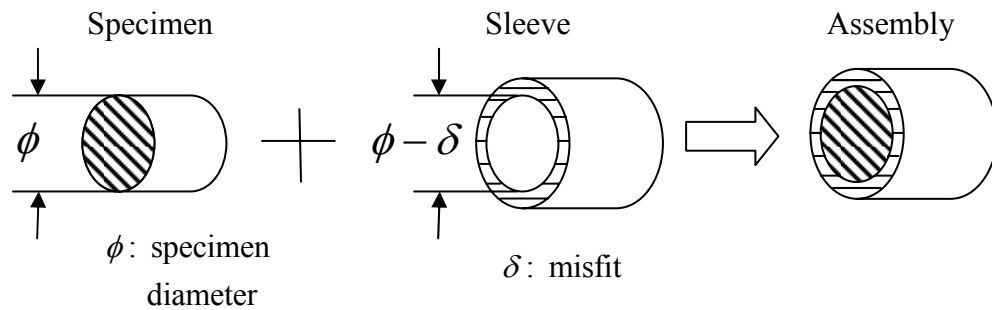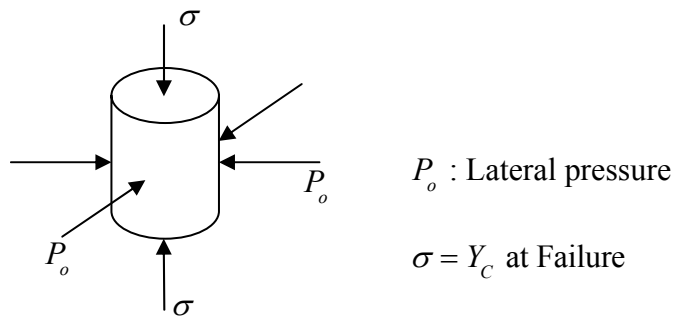
Figure 2-1: A schematic illustration of a triaxial stress state and the shrink-fit sleeve used to confine the ceramic specimen (Chen and Ravichandran)
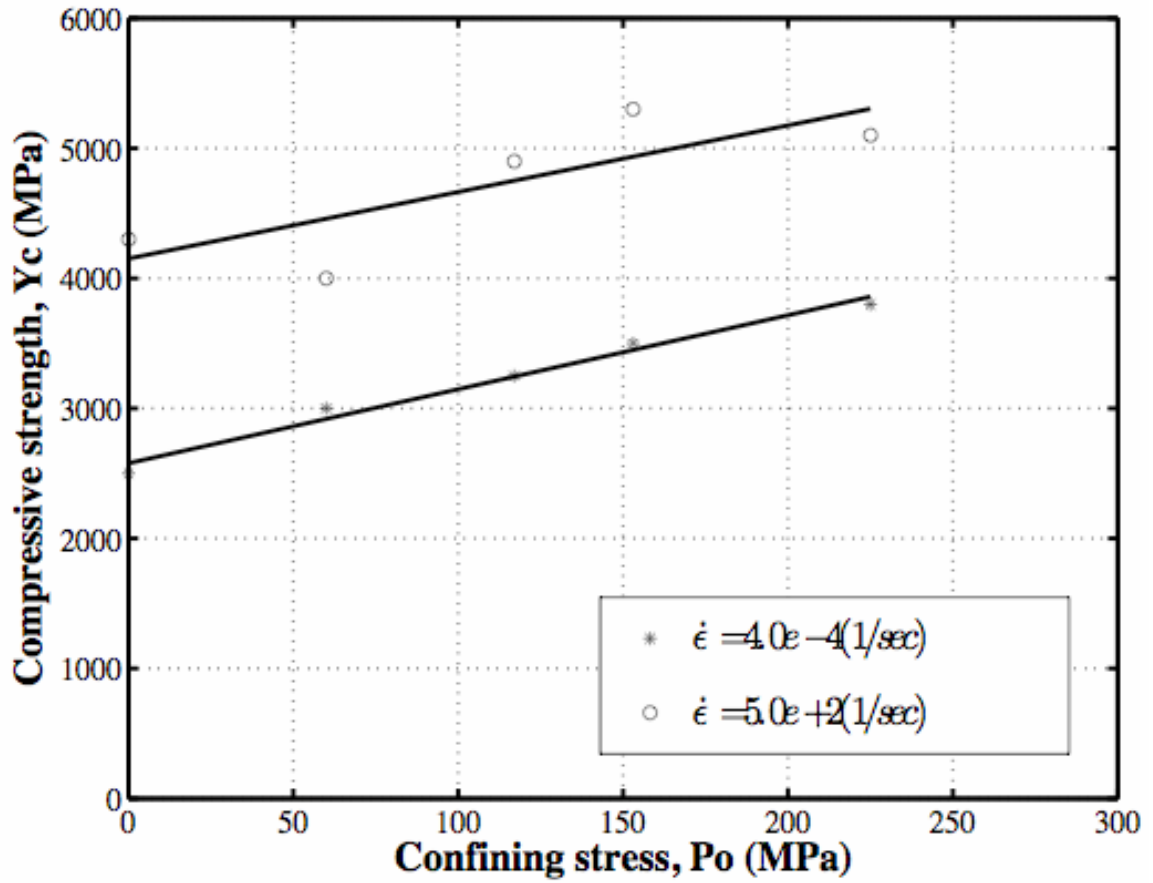
Figure 2-2: Compressive strength vs. the confining pressure in multi-axial compression test on Aluminum Nitride (Chen and Ravichandran)
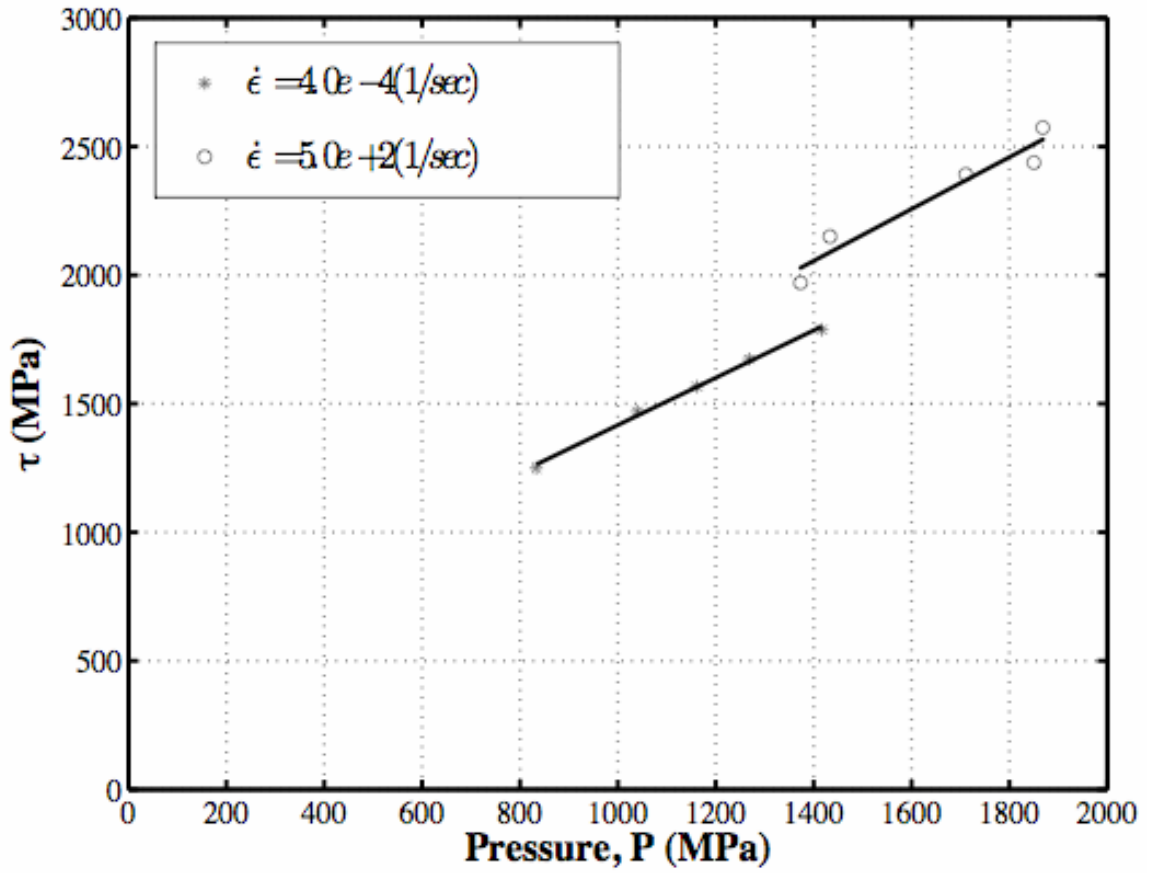
Figure 2-3: Shear strength vs. the applied pressure in multi-axial compression test on Aluminum Nitride (Chen and Ravichandran)
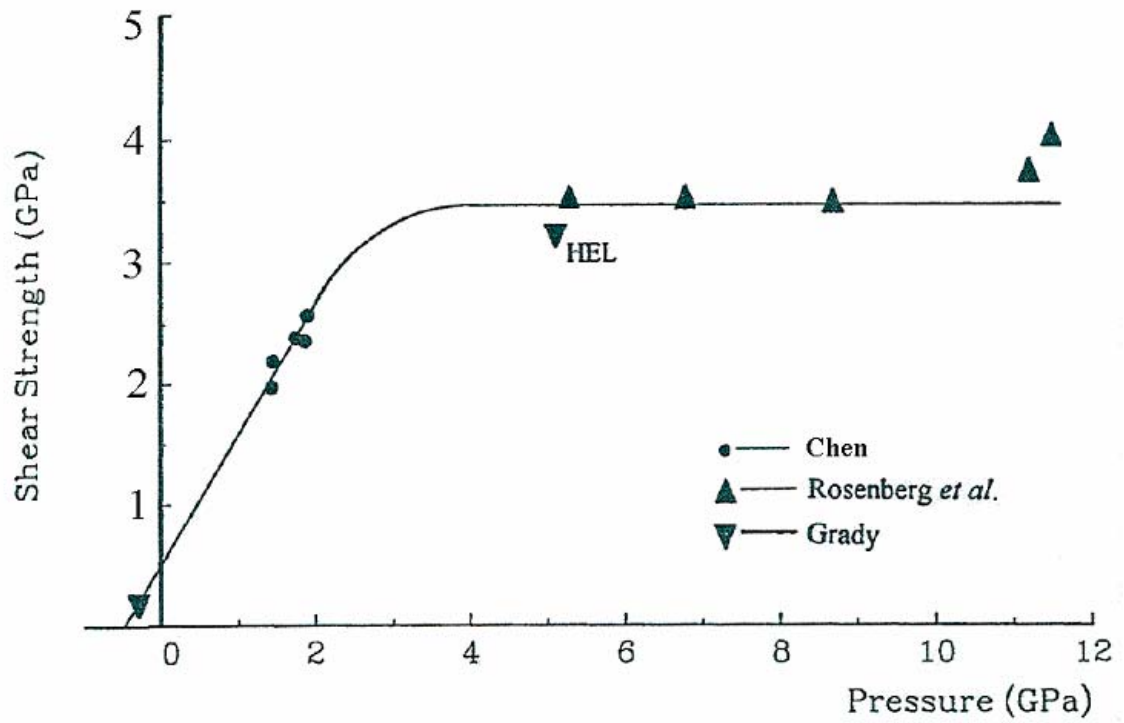
Figure 2-4: The shear strengths of Aluminum Nitride under dynamic loading (Chen)
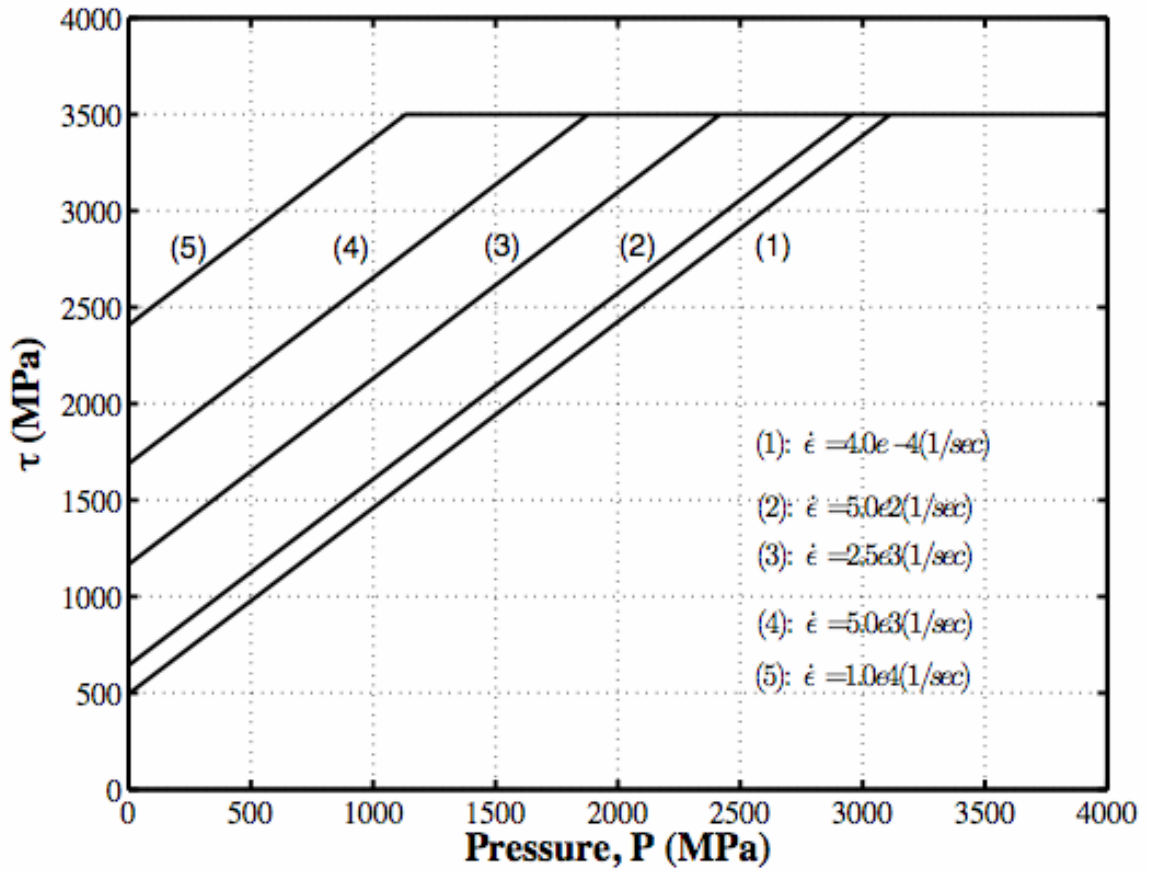
Figure 2-5: The shear strength vs. the applied pressure at various strain-rates (Aluminum Nitride)
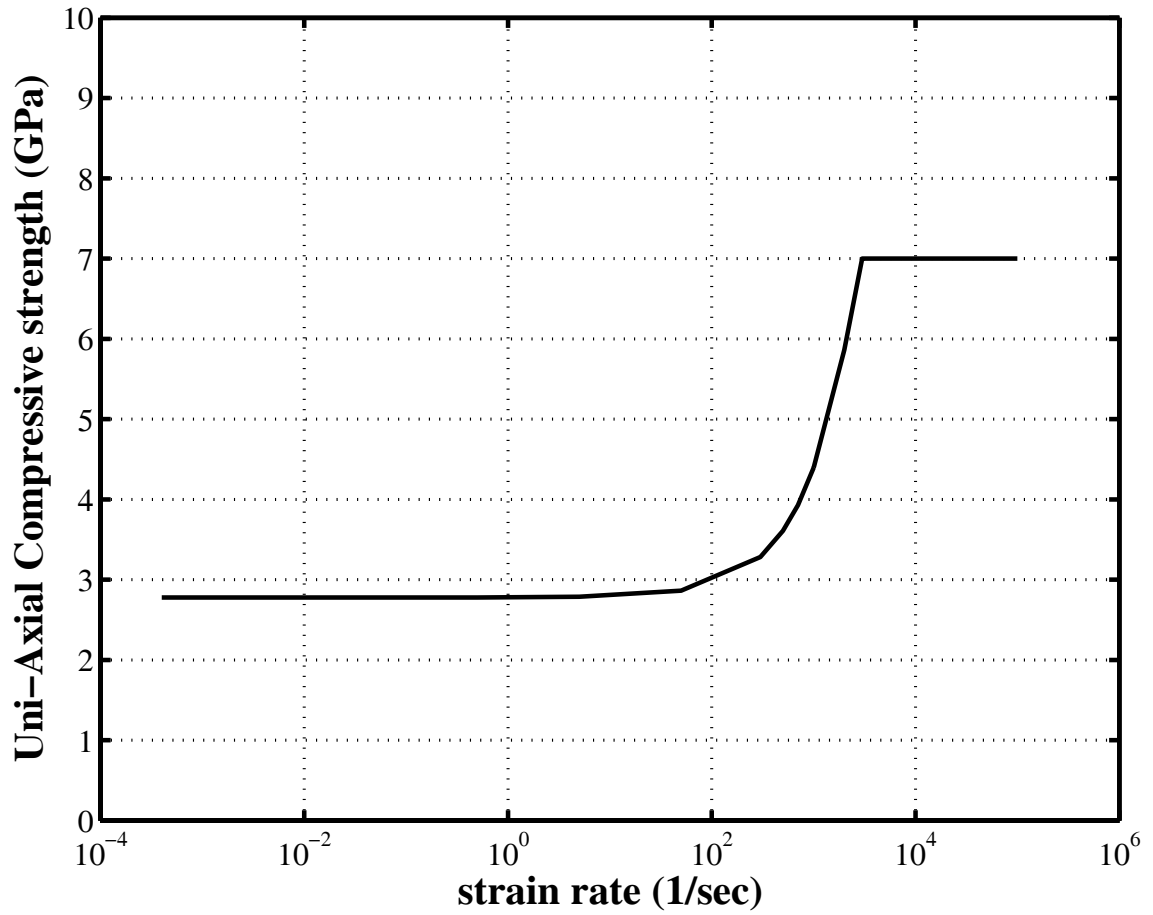
Figure 2-6: Uniaxial strength vs. the applied strain-rate (Aluminum Nitride)
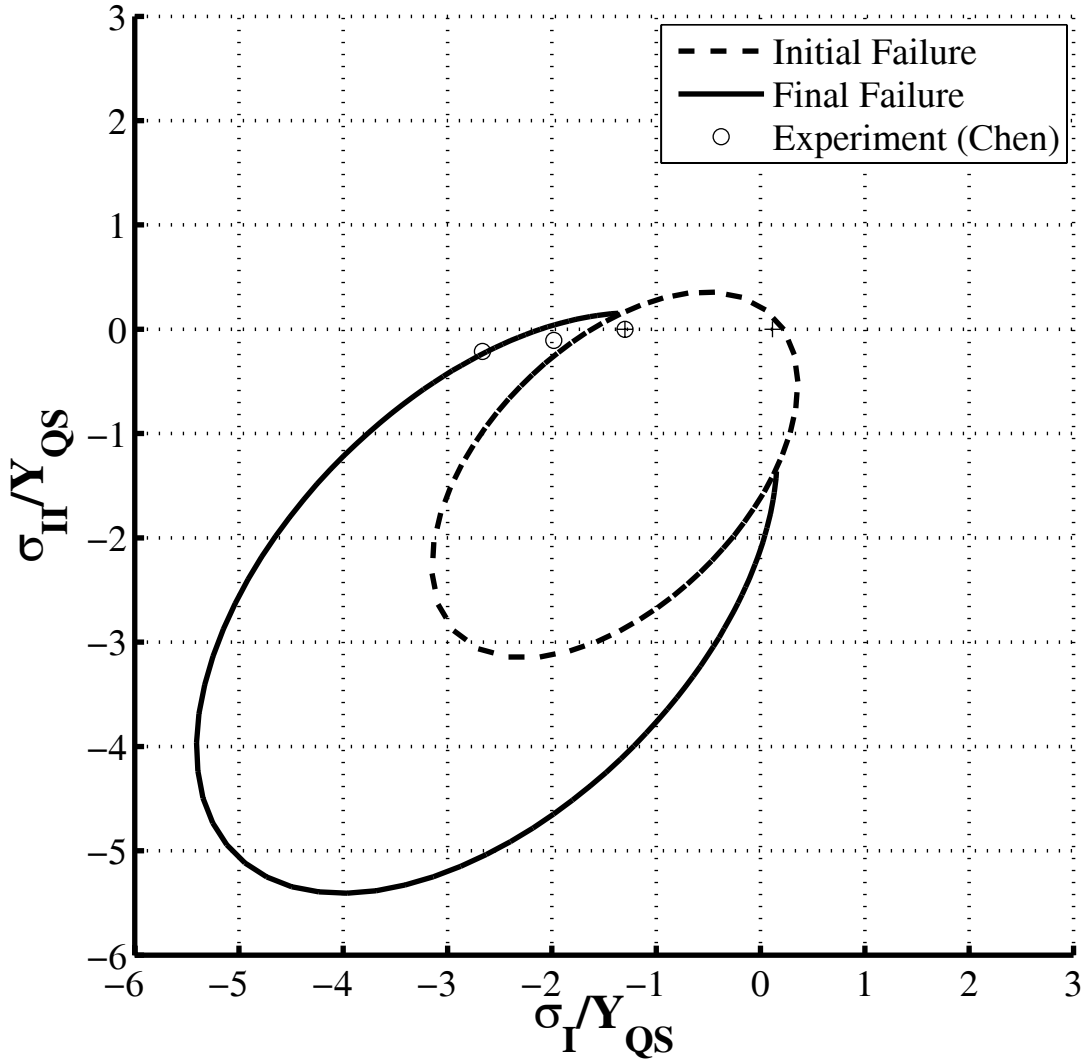
Figure 2-7: Pressure-dependent initial and final failure surfaces in non-dimensionalized principal stress plane ($\sigma_{III} \neq 0$), ($\dot{\varepsilon} = 5 \times 10^2$ (1/sec))
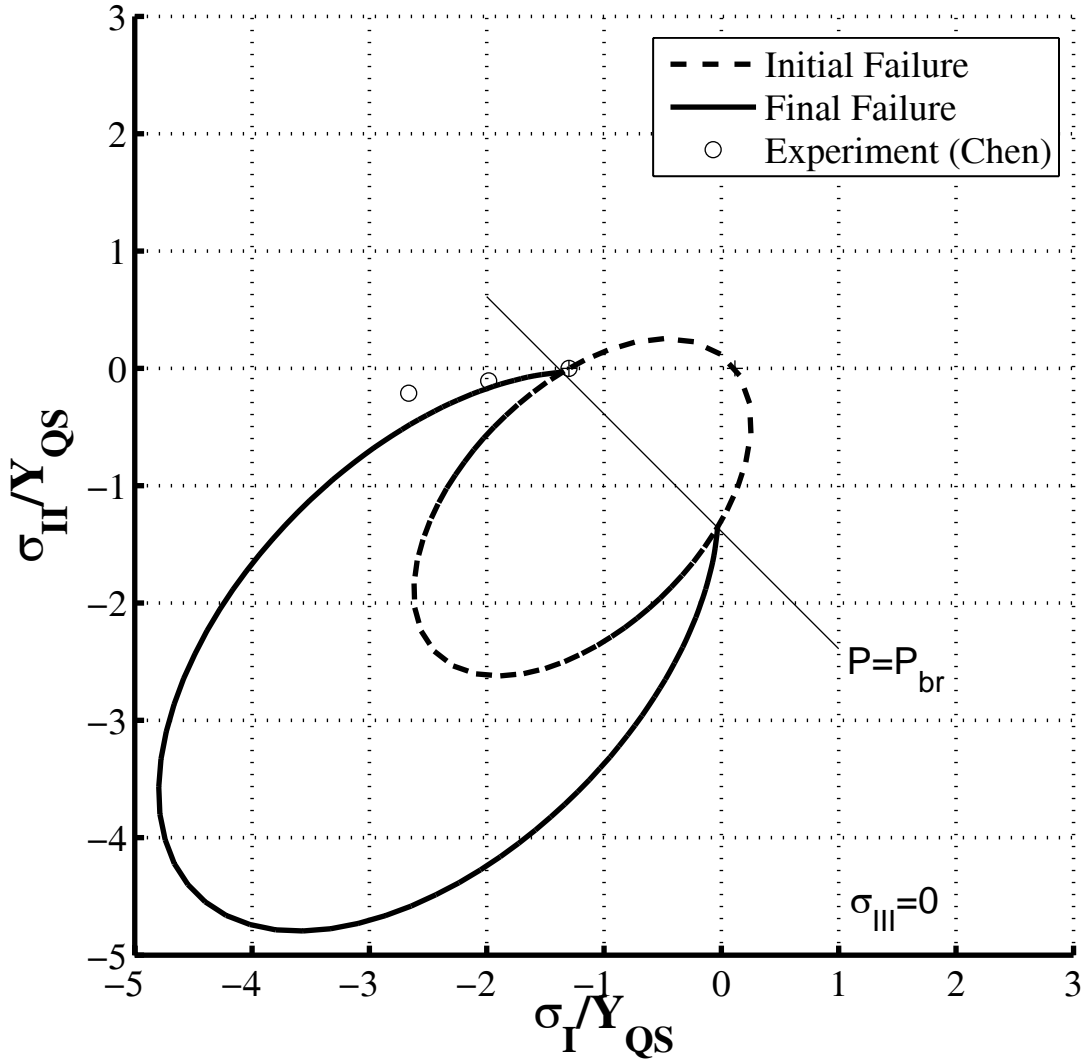
Figure 2-8: Pressure-dependent initial and final failure surfaces in non-dimensionalized principal stress plane ($\sigma_{III} = 0$), ($\dot{\varepsilon} = 5 \times 10^2$ (1/sec))
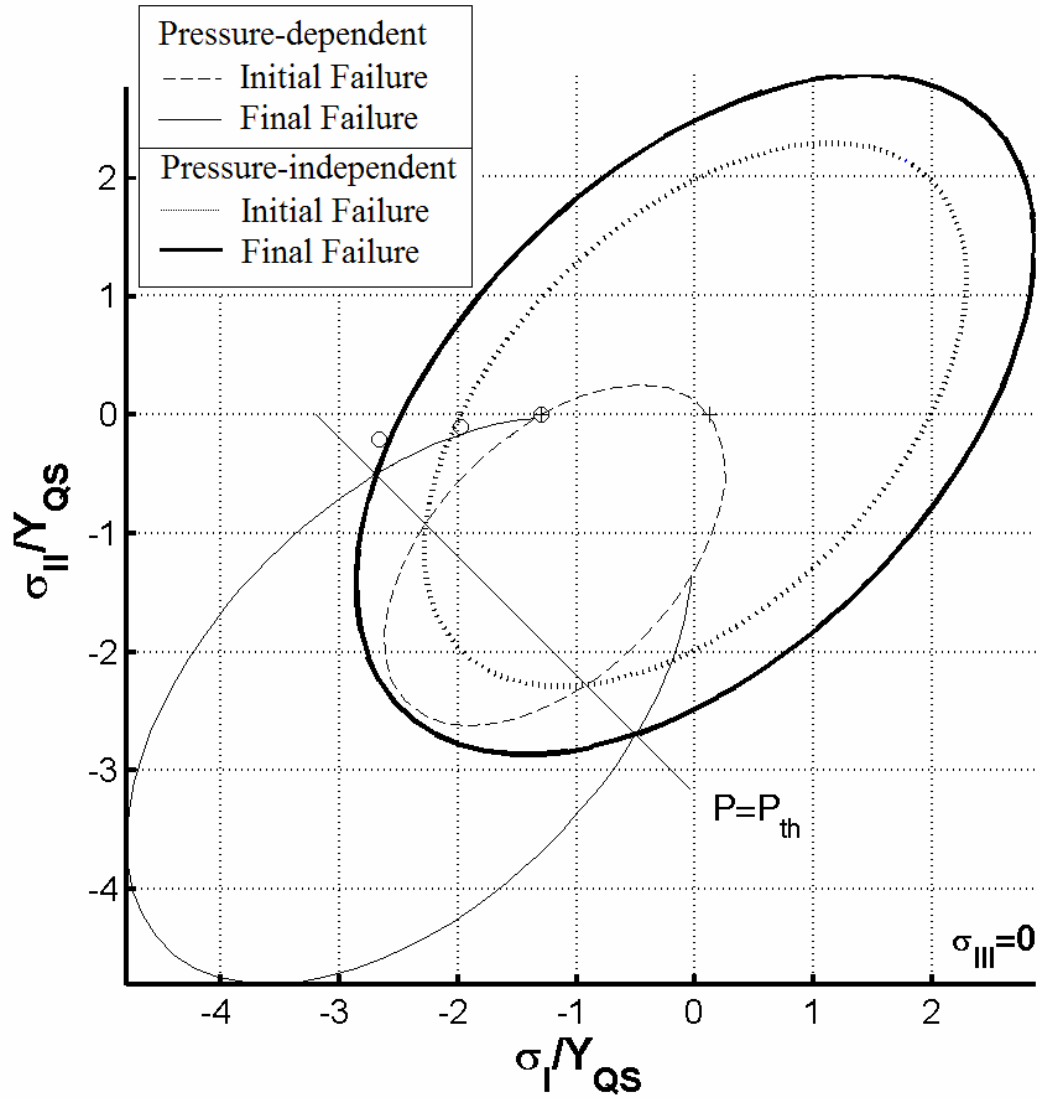
Figure 2-9: Pressure-independent and pressure-dependent initial and final failure surfaces in non-dimensionalized principal stress plane ($\dot{\varepsilon} = 5 \times 10^2$ (1/sec))
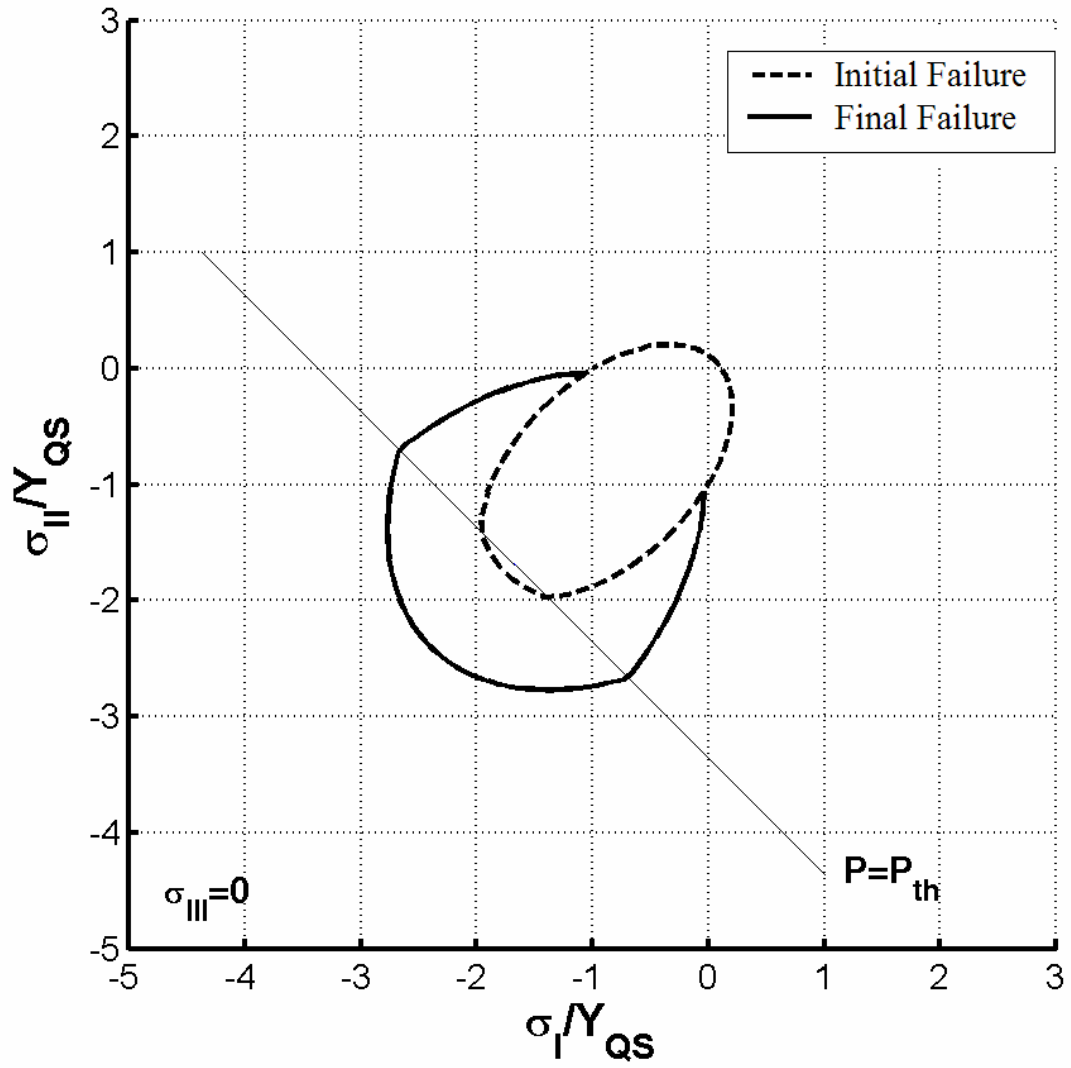
Figure 2-10: Initial and final failure surfaces in non-dimensionalized principal stress plane ($\dot{\varepsilon} = 1 \times 10^{-4}$ (1/sec))
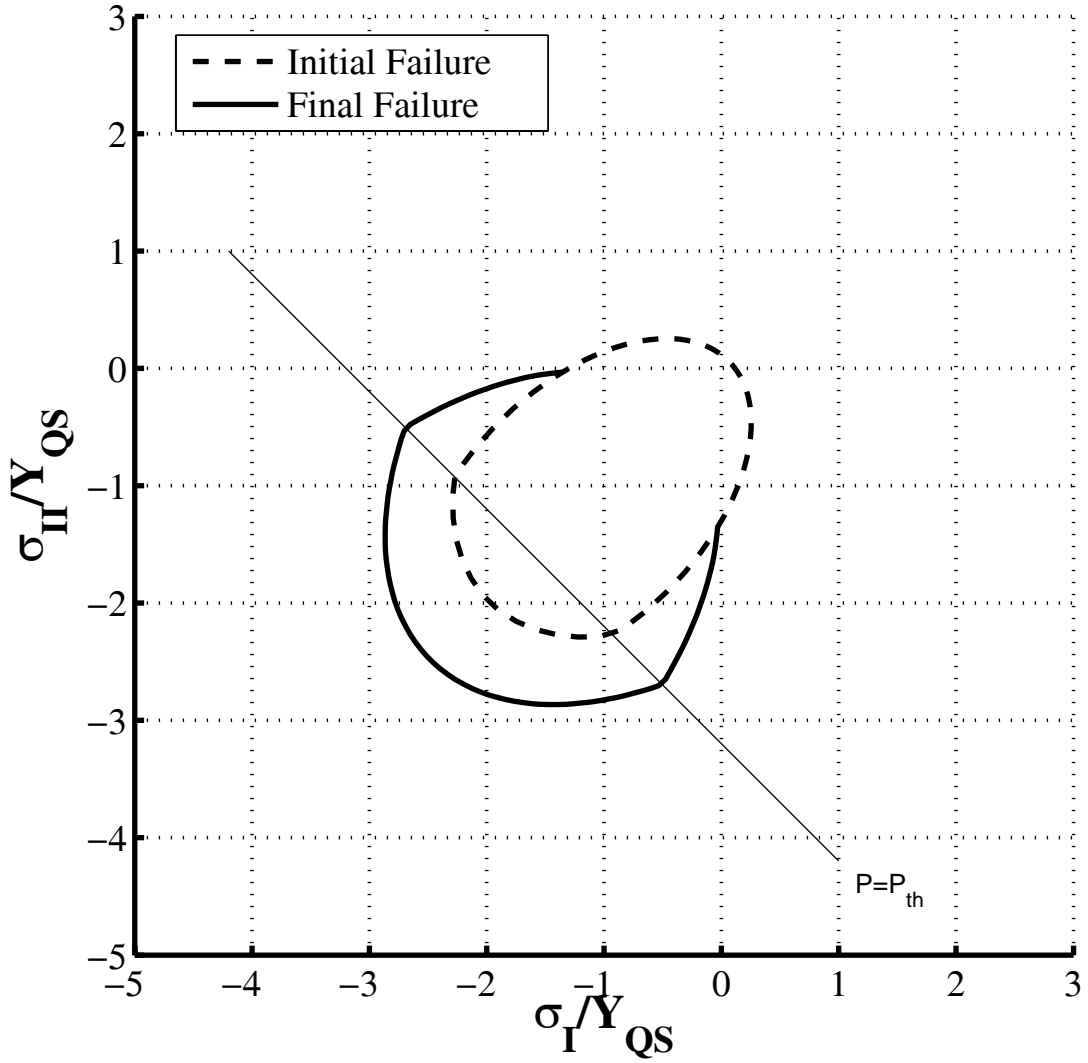
Figure 2-11: Initial and final failure surfaces in non-dimensionalized principal stress plane ($\dot{\varepsilon} = 5 \times 10^2$ (1/sec))
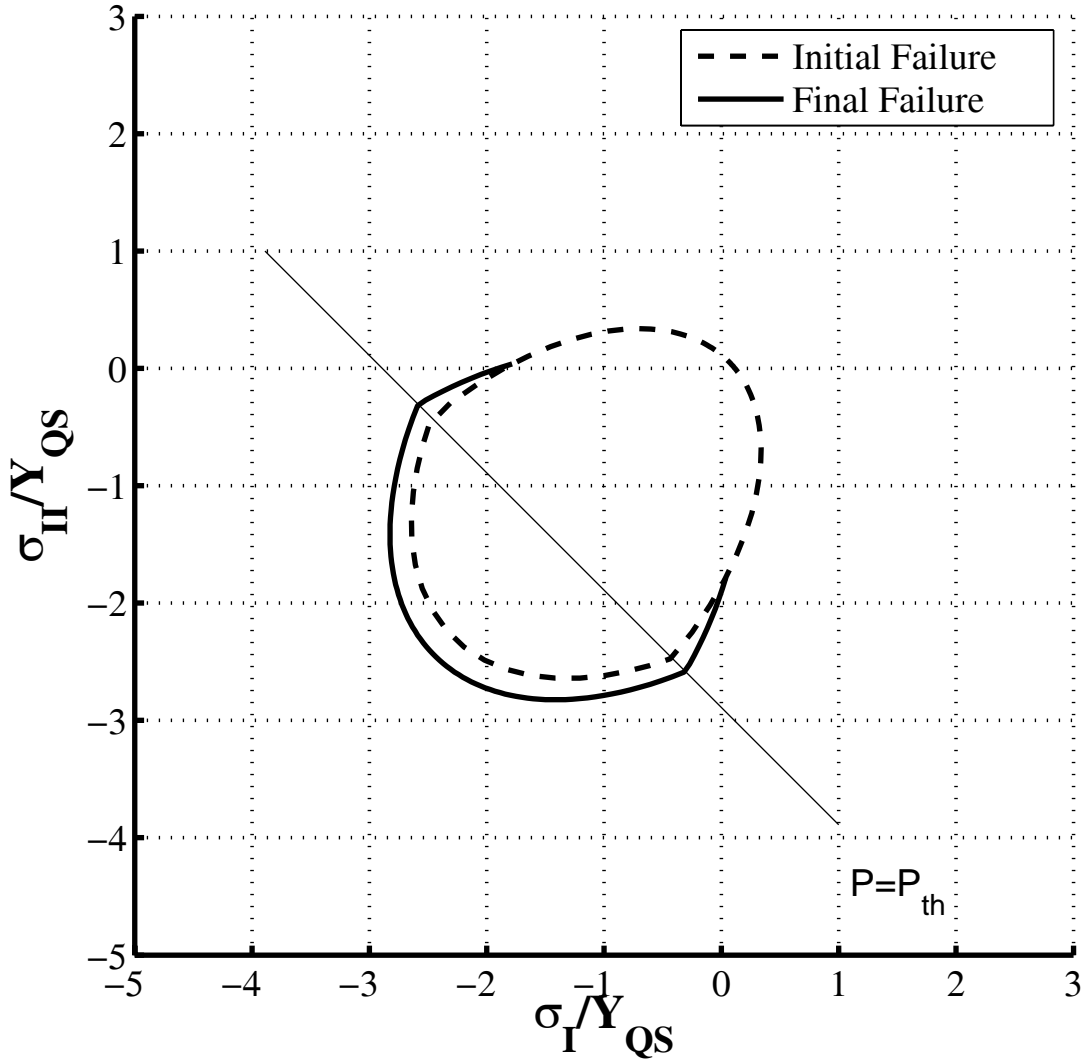
Figure 2-12: Initial and final failure surfaces in non-dimensionalized principal stress plane ($\dot{\varepsilon} = 1.5 \times 10^3$ (1/sec))
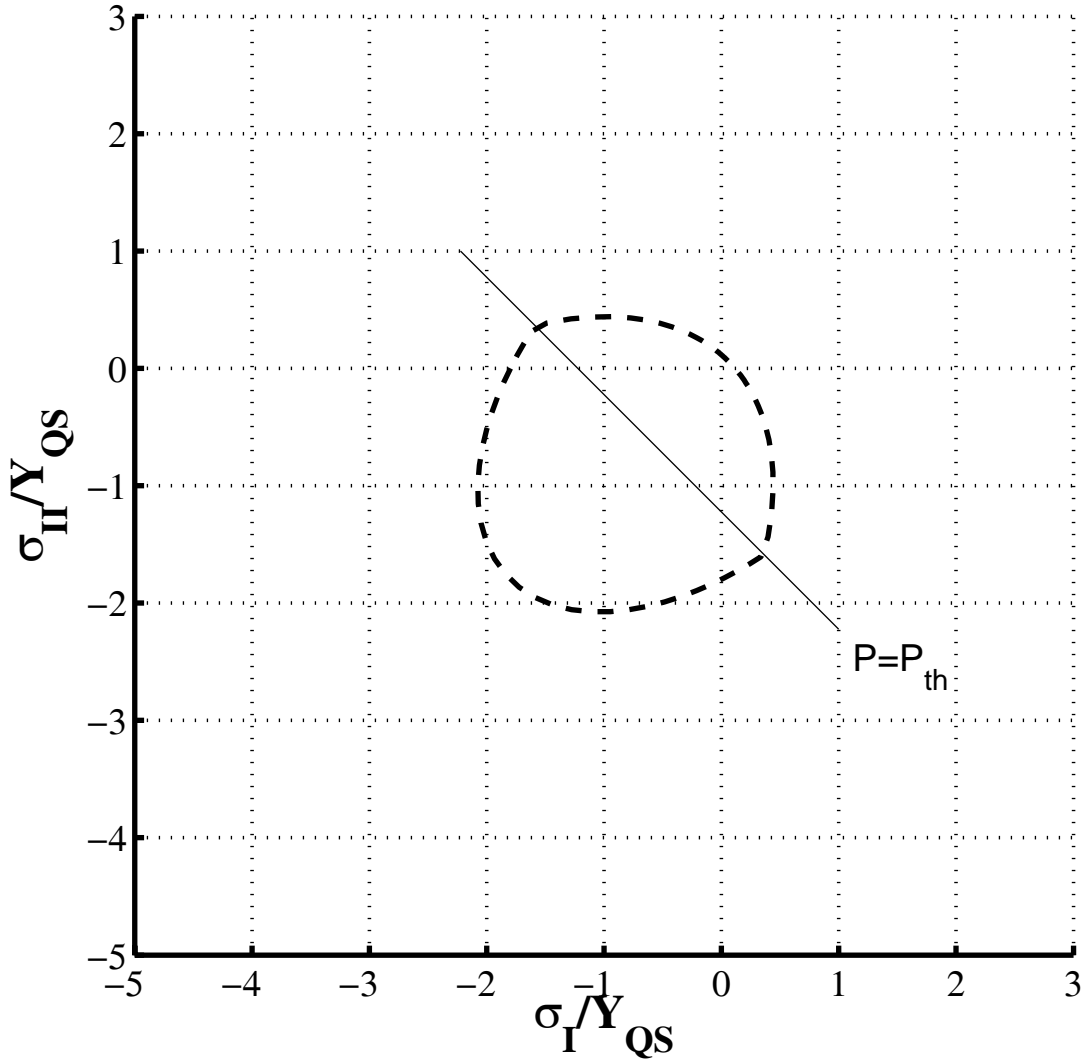
Figure 2-13: Initial surfaces in non-dimensionalized principal stress plane
$(\dot{\varepsilon} = 1 \times 10^4 \ (1/\text{sec}))$
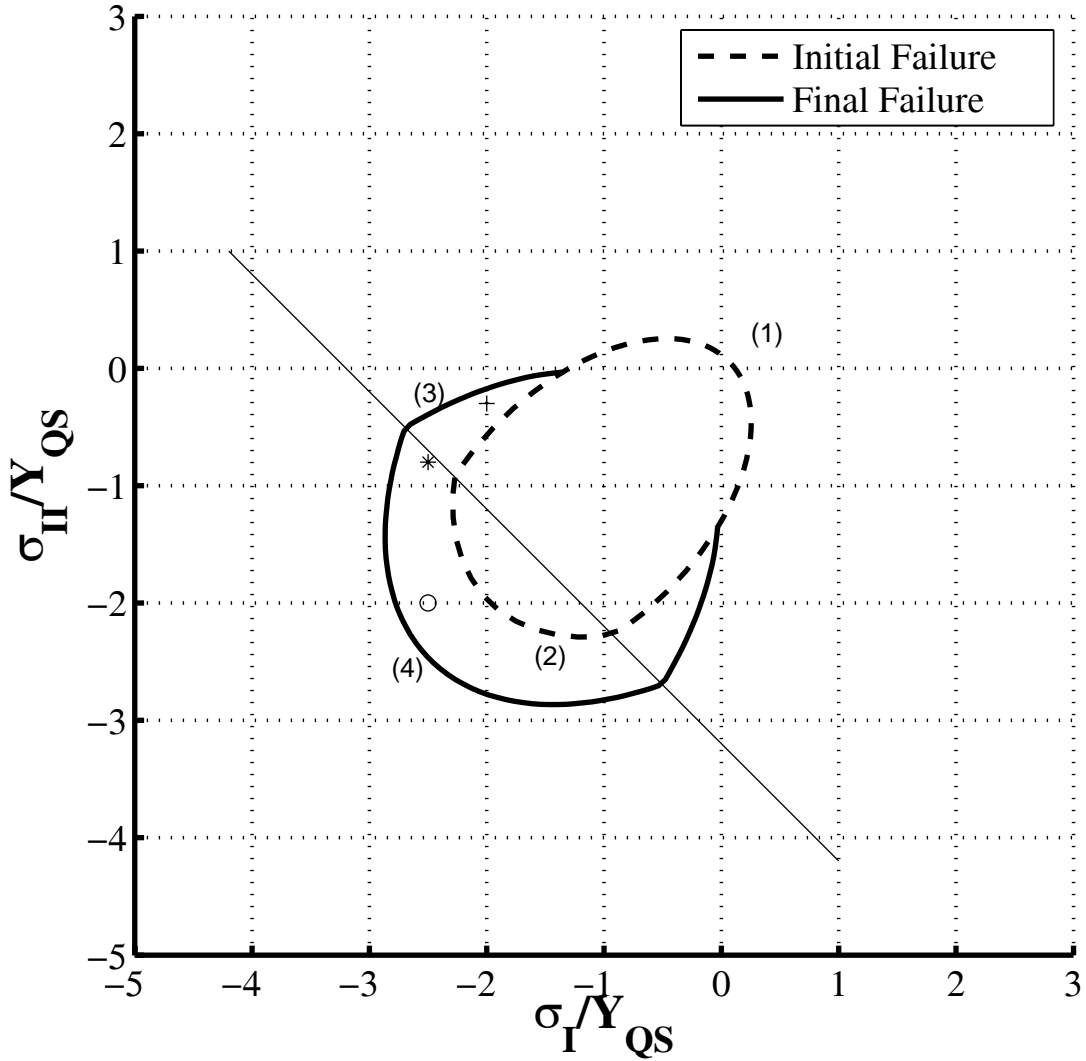
Figure 2-14: Initial and final failure surfaces for damage model
$(\dot{\varepsilon} = 5 \times 10^2 \ (1/\text{sec}))$
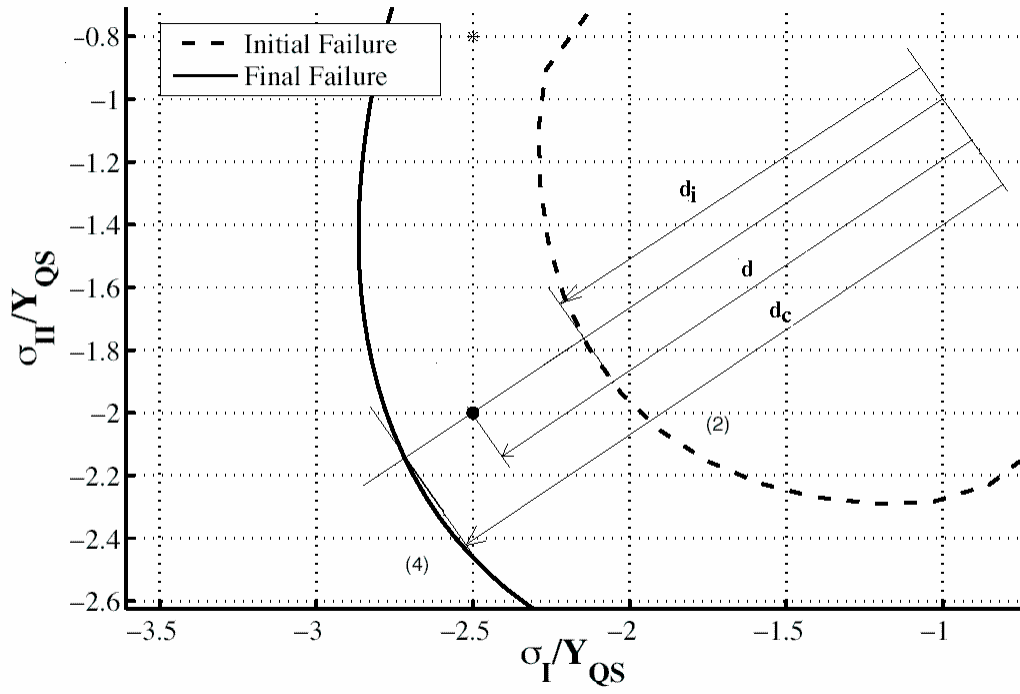
Figure 2-15: Three distances for damage model ($\dot{\varepsilon} = 5 \times 10^2$ (1/sec) **)**

114
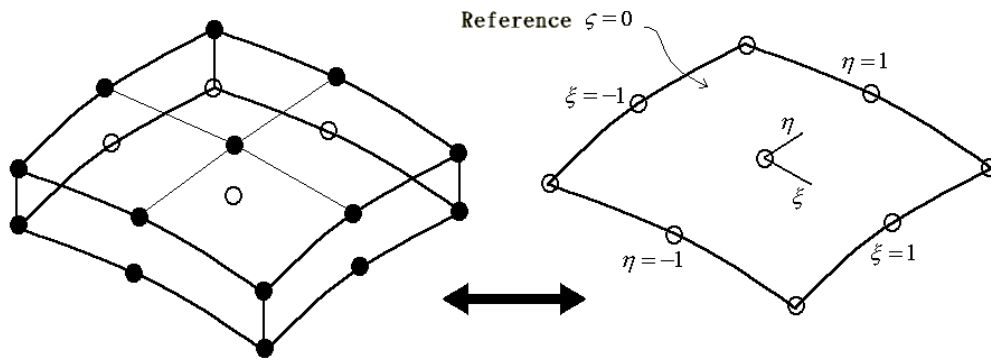
Figure 4-1: Two versions of solid shell elements, eighteen-node and nine-node element
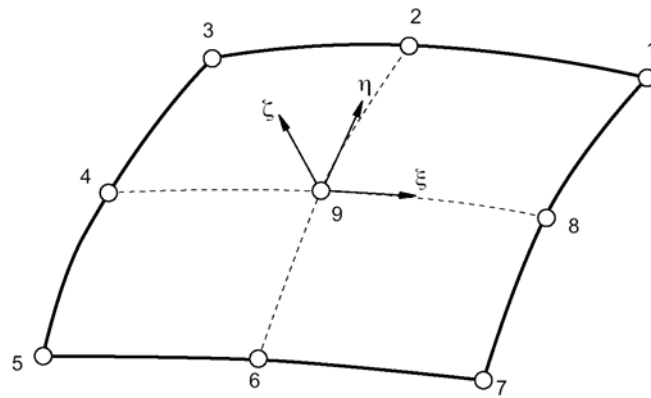
Figure 4-2: Node numbering for a nine-node element
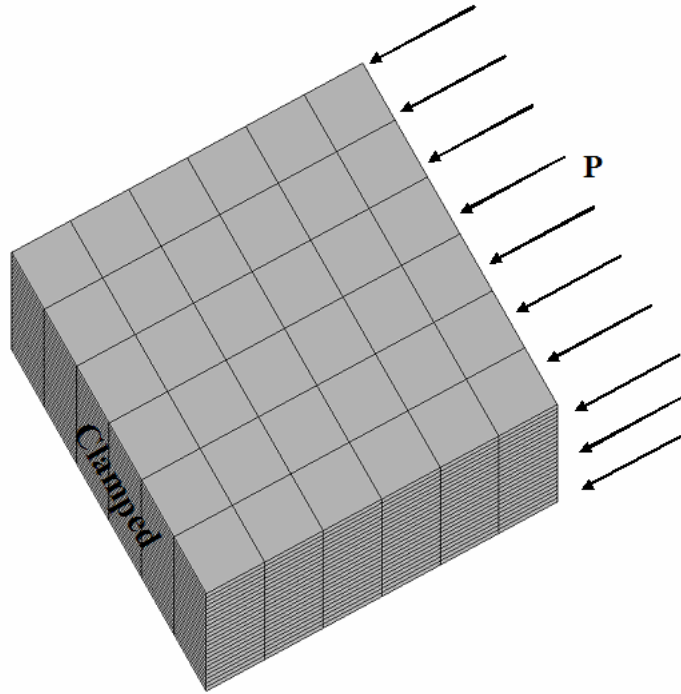
Figure 5-1: Configuration of a clamped ceramic cube (Aluminum Nitride) subjected to the uniaxial pressure load
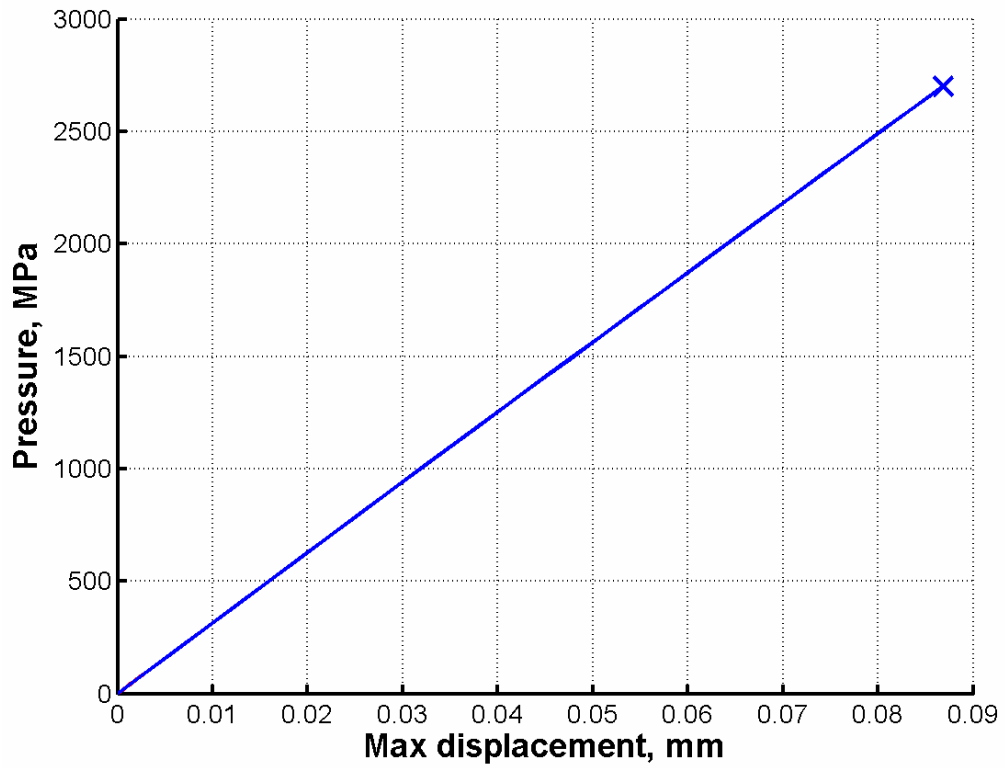
Figure 5-2: Pressure vs. maximum displacement of a ceramic cube (Aluminum Nitride) subjected to the uniaxial static load
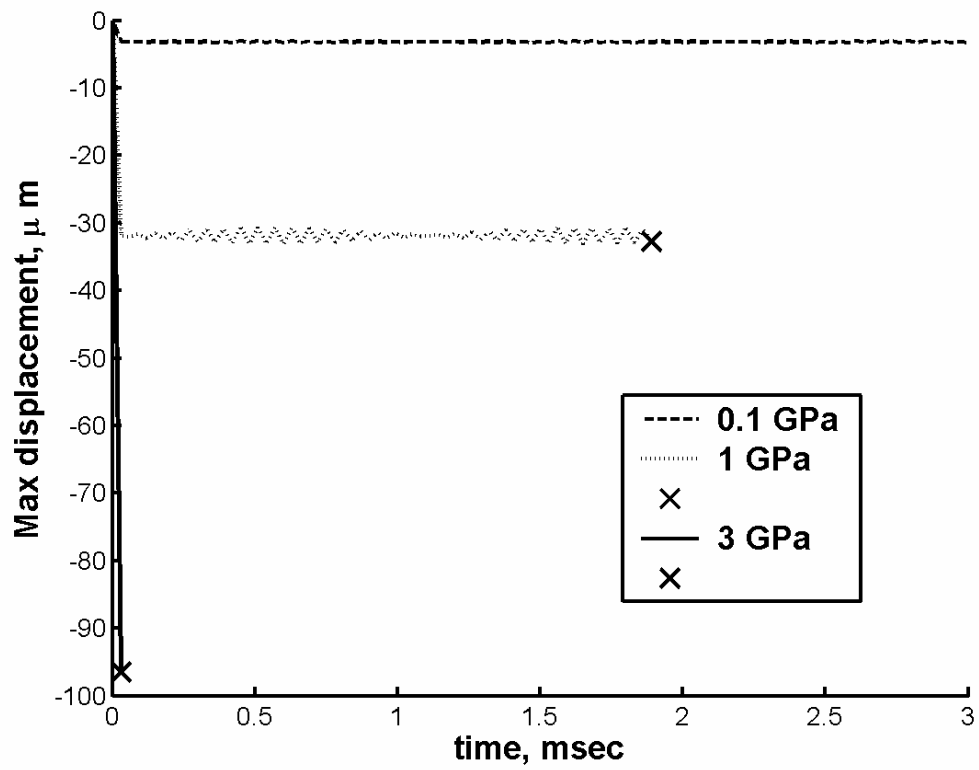
Figure 5-3: Maximum displacement vs. time of the ceramic cube (Aluminum Nitride) subjected to the uniaxial dynamic pressure
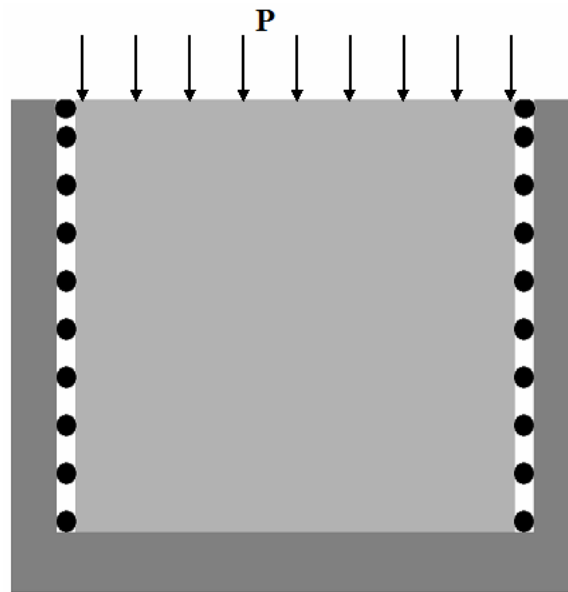
Figure 5-4: Configuration of a constrained ceramic cube (Aluminum Nitride) subjected to the uniaxial pressure load
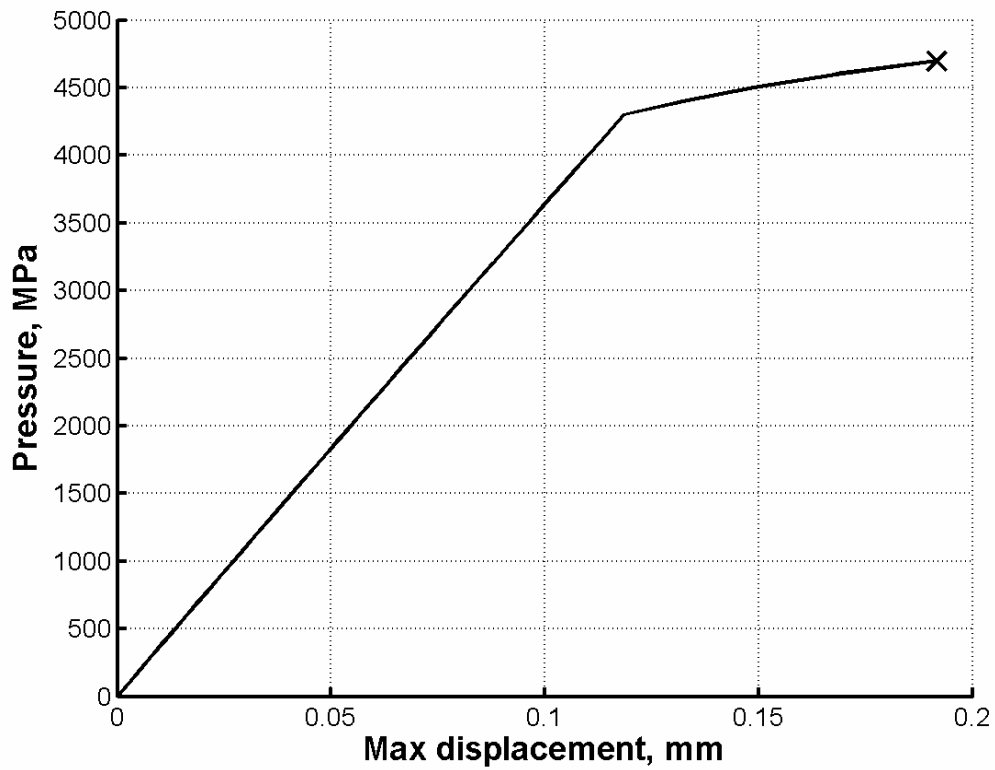
Figure 5-5: Pressure vs. maximum displacement of a constrained ceramic cube (Aluminum Nitride) subjected to the uniaxial static load
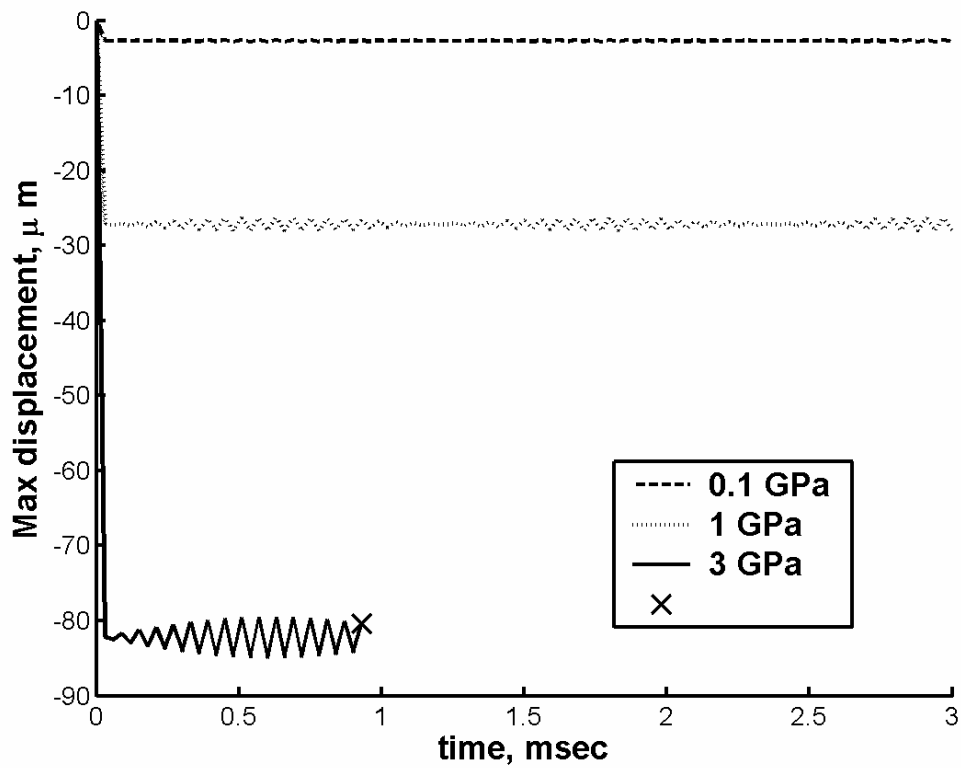
Figure 5-6: Maximum displacement vs. time of the constrained ceramic cube (Aluminum Nitride) subjected to the uniaxial dynamic pressure
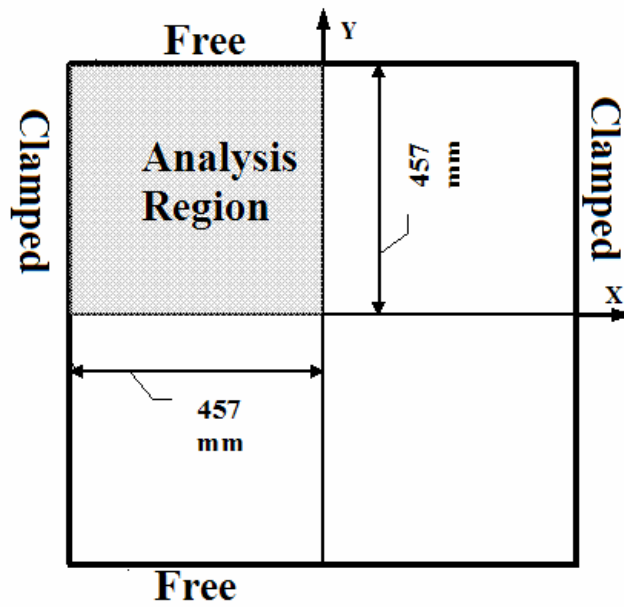
Figure 5-7: Analysis region and boundary conditions of the flat and arched ceramic panels (Aluminum Nitride)
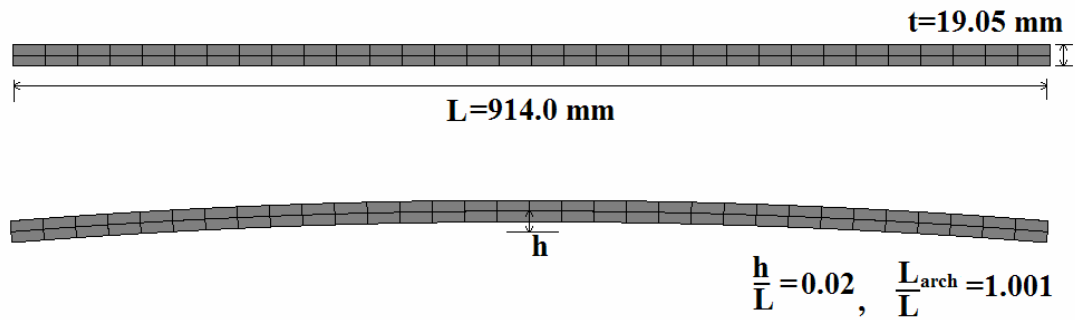
Figure 5-8: Geometry of flat and arched ceramic panels (Aluminum Nitride)
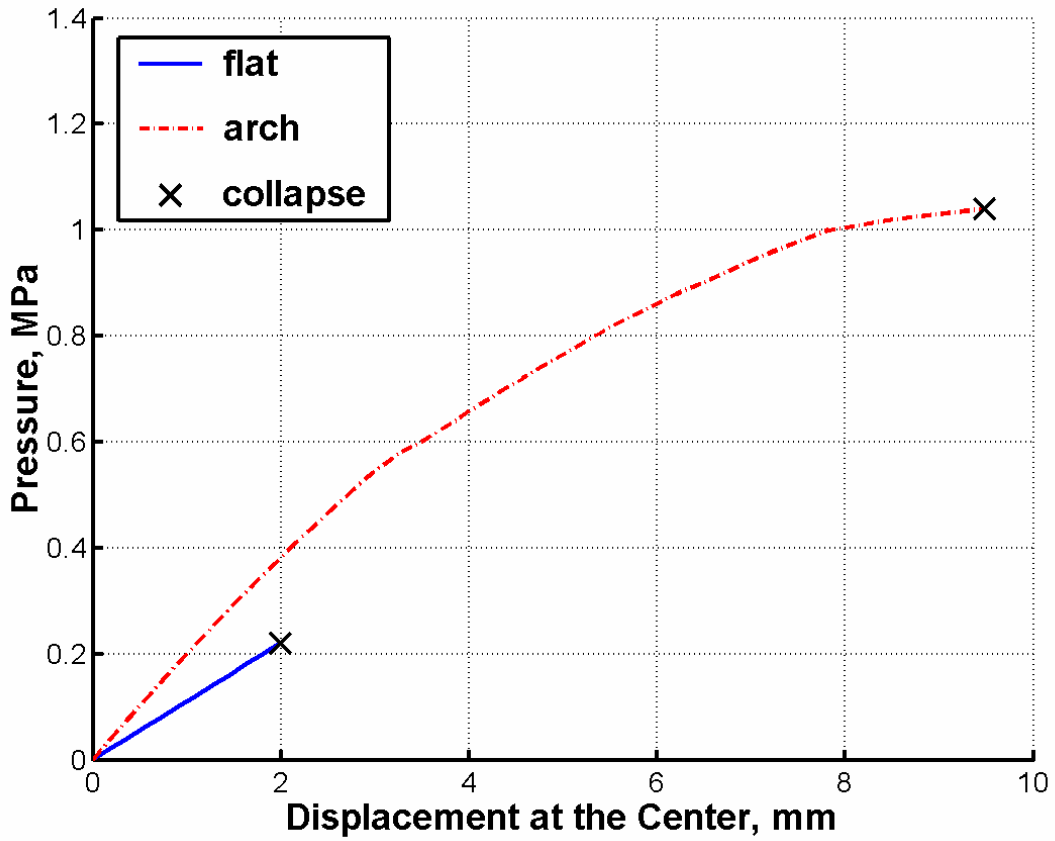
Figure 5-9: Pressure vs. displacement at the center of the flat and arched ceramic panels (Aluminum Nitride)
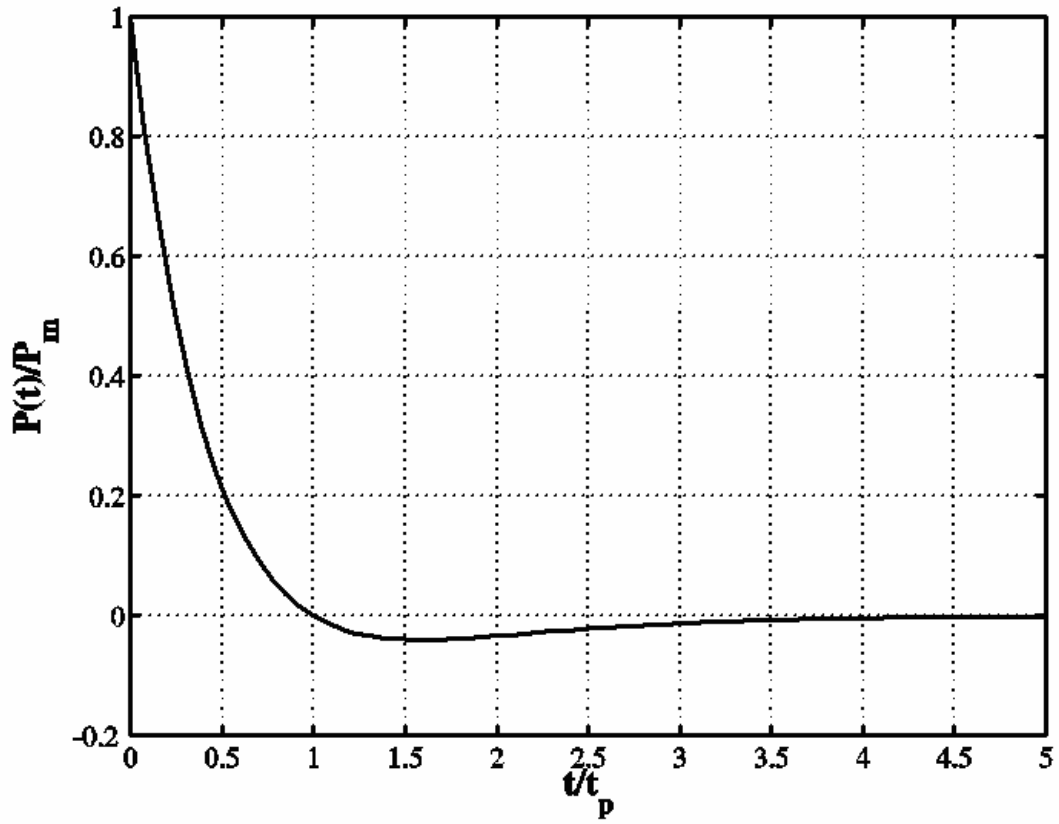
Figure 5-10: Non-dimensional pressure model for blast wave pressure loading using Friedlander decay function
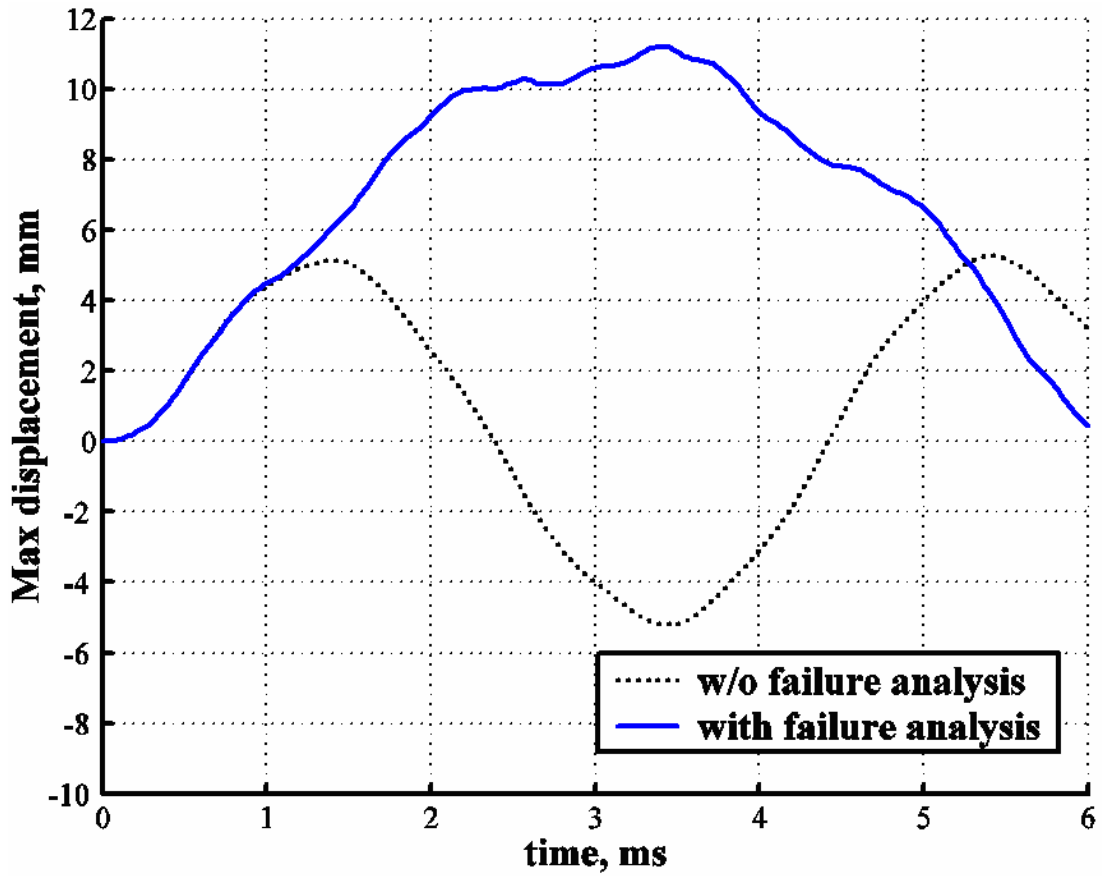
Figure 5-11: Dynamic displacement at the panel center vs. time for the flat ceramic panel (Aluminum Nitride)
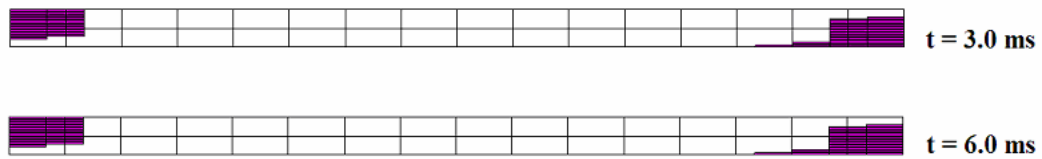
Figure 5-12: Failed region of the flat ceramic panel (Aluminum Nitride)
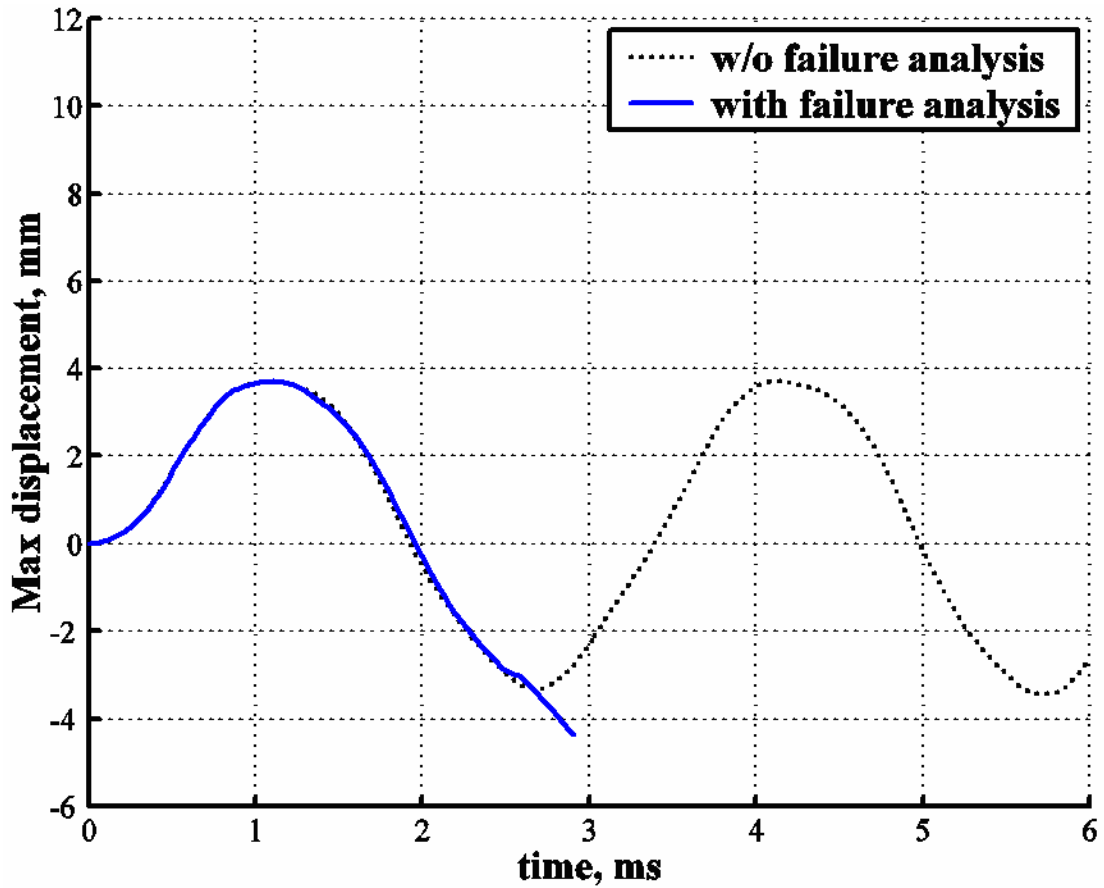
Figure 5-13: Dynamic displacement at the panel center vs. time for the arched ceramic panel (Aluminum Nitride)
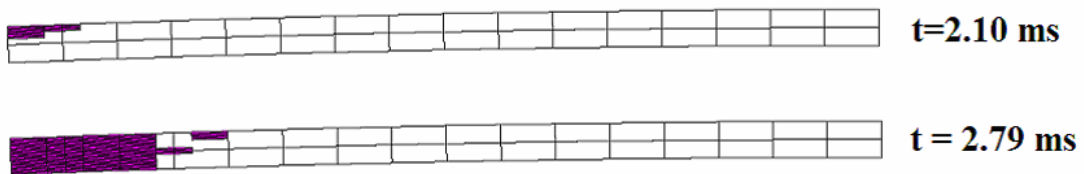
Figure 5-14: Failed region of the arched ceramic panel (Aluminum Nitride)
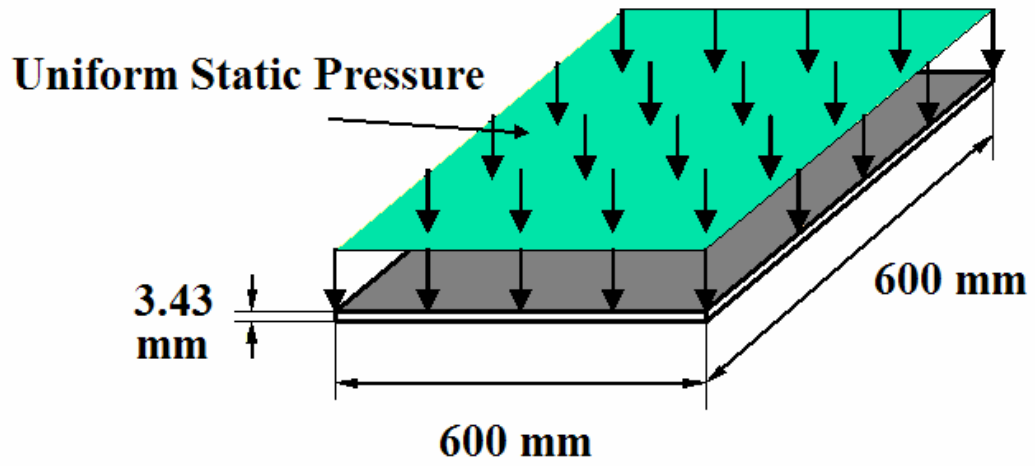
Figure 5-15: Geometry and loading conditions for unidirectional composite panels (E-Glass/Polyester)
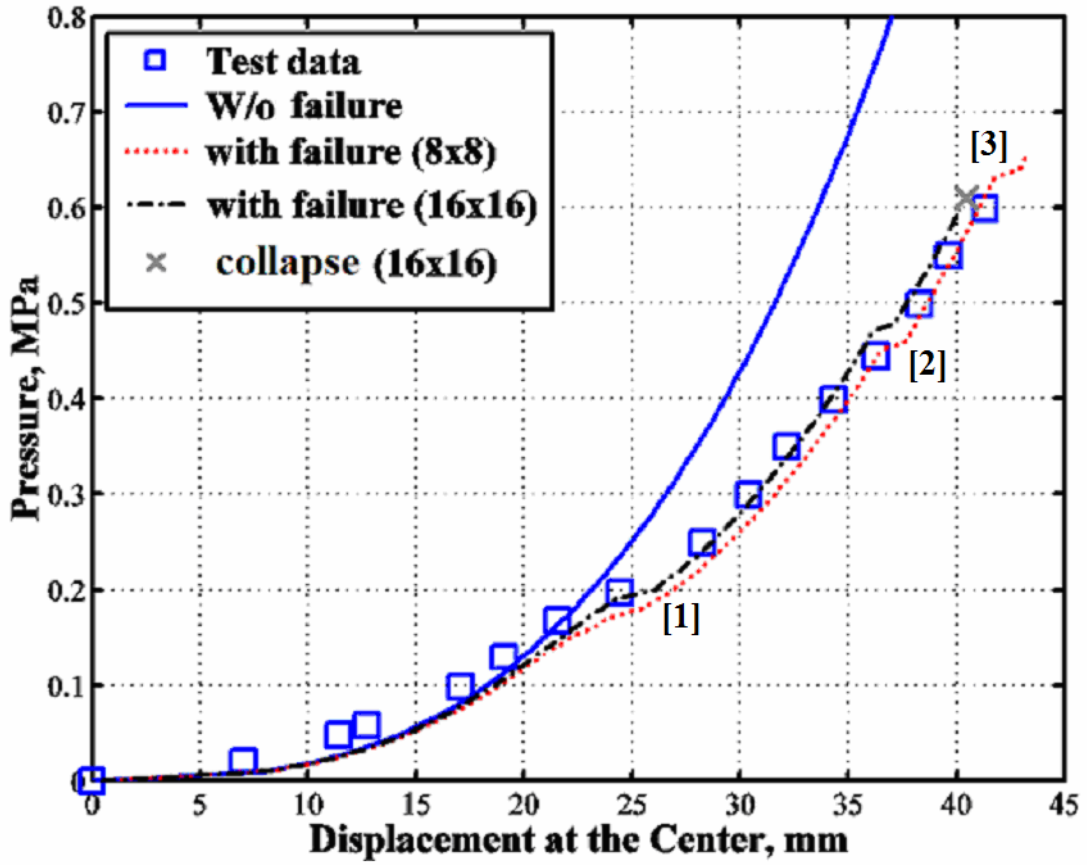
Figure 5-16: Pressure vs. displacement at the E-Glass/Polyester panel center
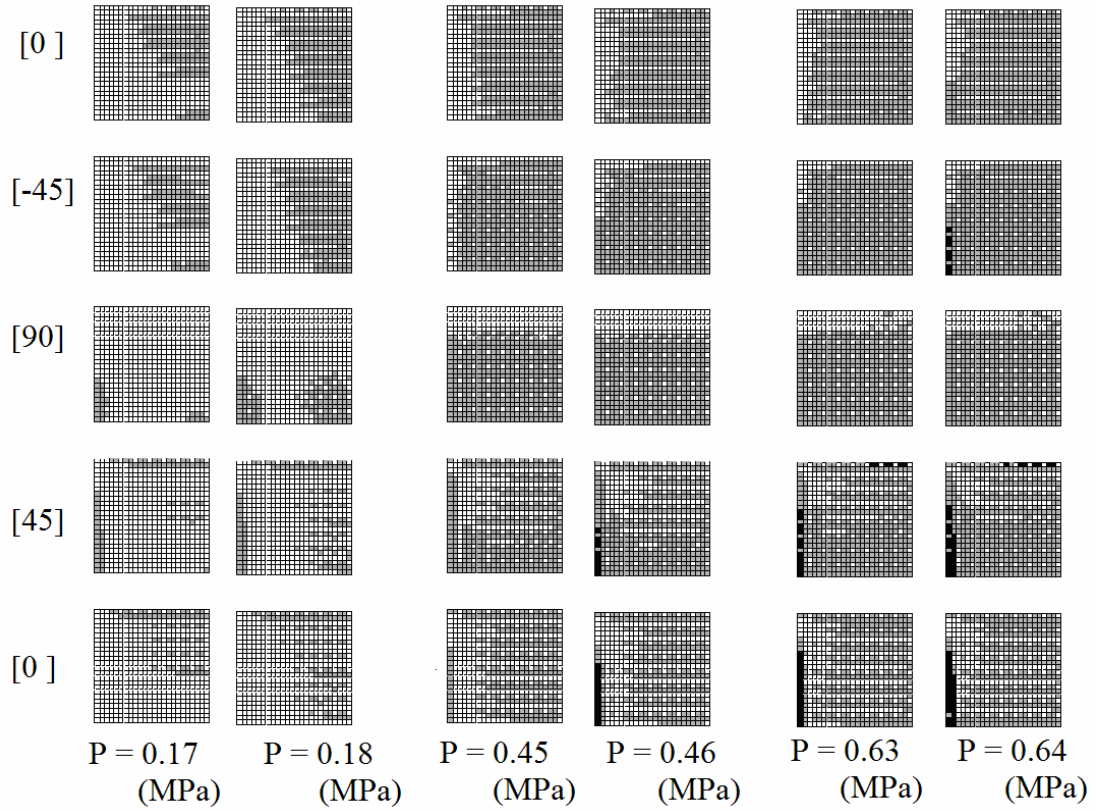
Figure 5-17: Failed regions for the E-Glass/Polyester panel near the computationally observed, drastic changes of the slope
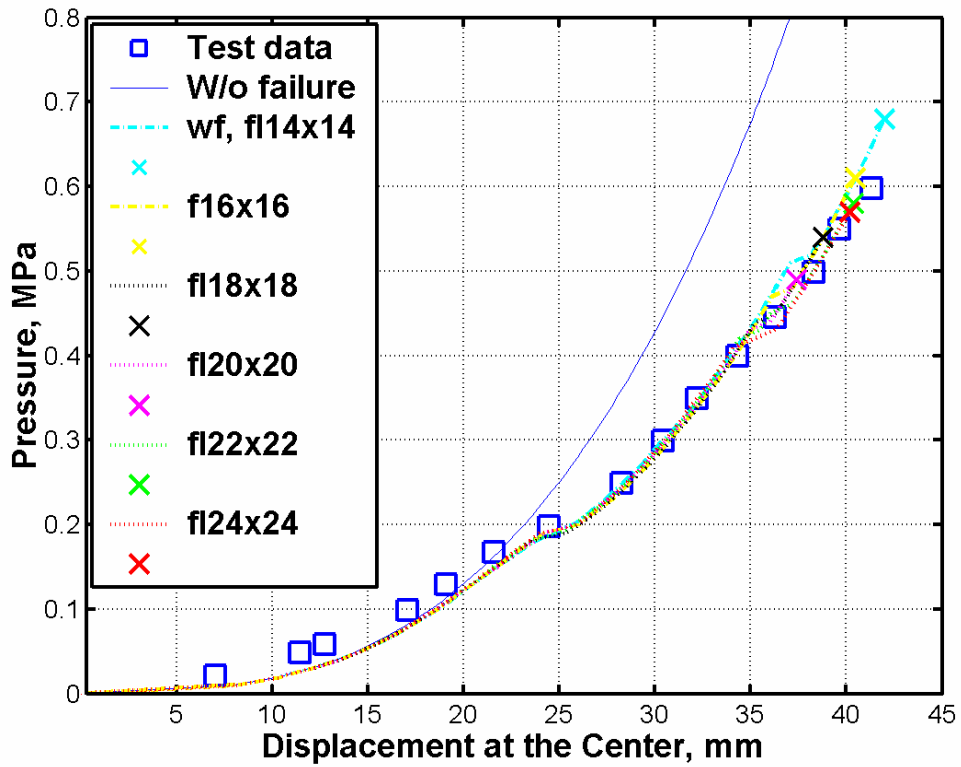
Figure 5-18: Pressure vs. displacement at the E-Glass/Polyester panel center to determine the structural collapse
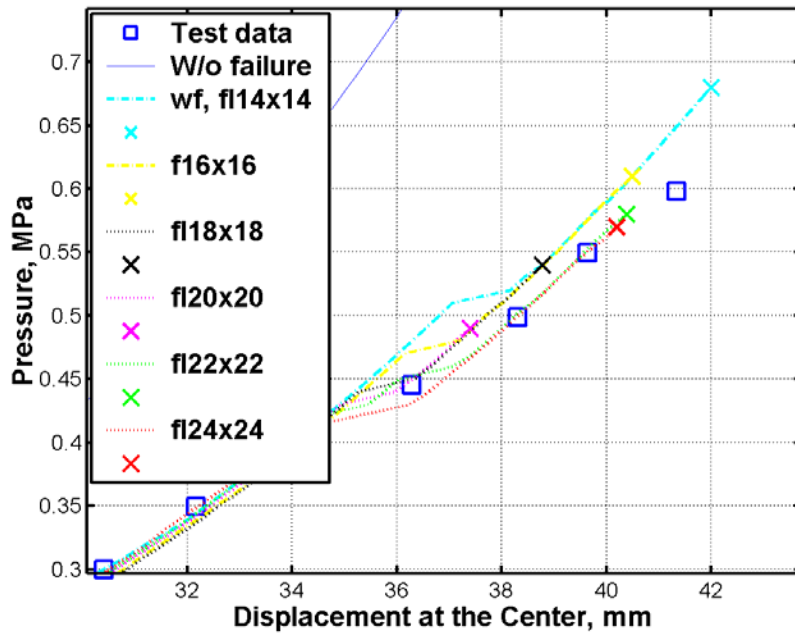
Figure 5-19: Pressure vs. displacement at the E-Glass/Polyester panel near the structural collapse

129
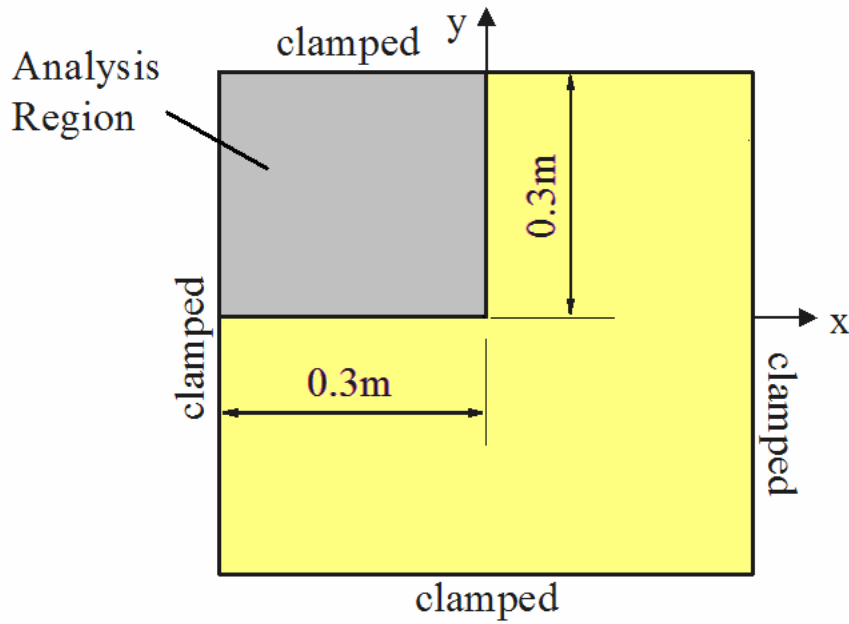
Figure 5-20: Analysis region for dynamic analyses of the E-Glass/Polyester panel under blast wave pressure loading
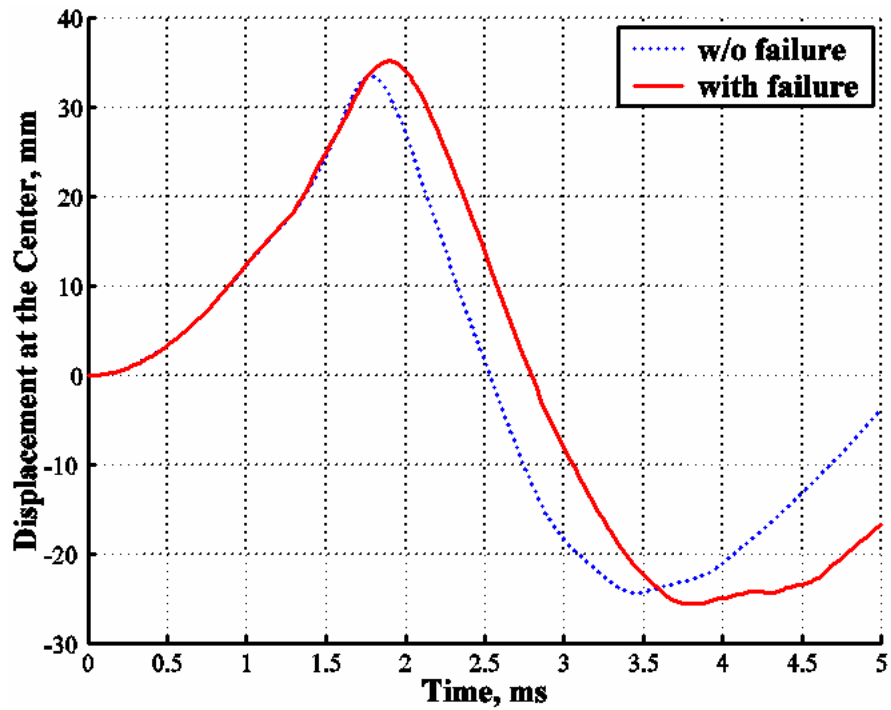
Figure 5-21: Displacement vs. time for the E-Glass/Polyester panel under blast wave pressure loading ($P_m = 0.2$ (MPa), $t_p = 1.8$ (msec), $\alpha = 0.35$)
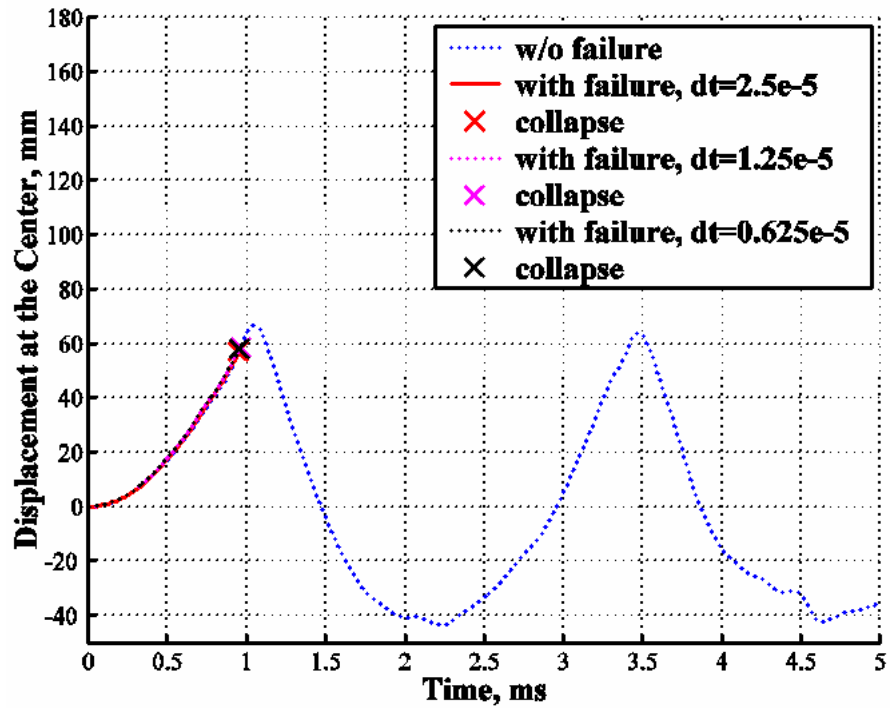
Figure 5-22: Displacement vs. time and structural collapse of the E-Glass/Polyester panel under blast wave pressure loading
($P_m = 1.0$ (MPa), $t_p = 1.8$ (msec), $\alpha = 0.35$)

@ 0.25 ms, 0 degree, layer 1   @ 0.50 ms, 0 degree, layer 1   @ 0.75 ms, 0 degree, layer 1   @ 0.9375 ms, 0 degree, layer 1
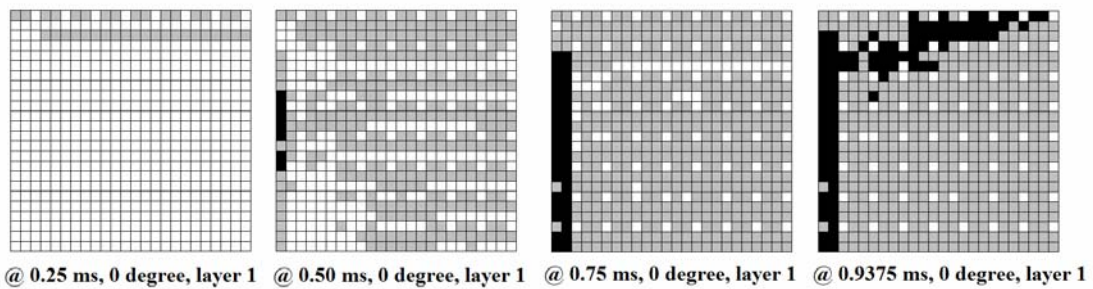
Figure 5-23: Failed regions at the layer number 1 of the E-Glass/Polyester panel along time (from 0.25 to 0.9375 msec)

131
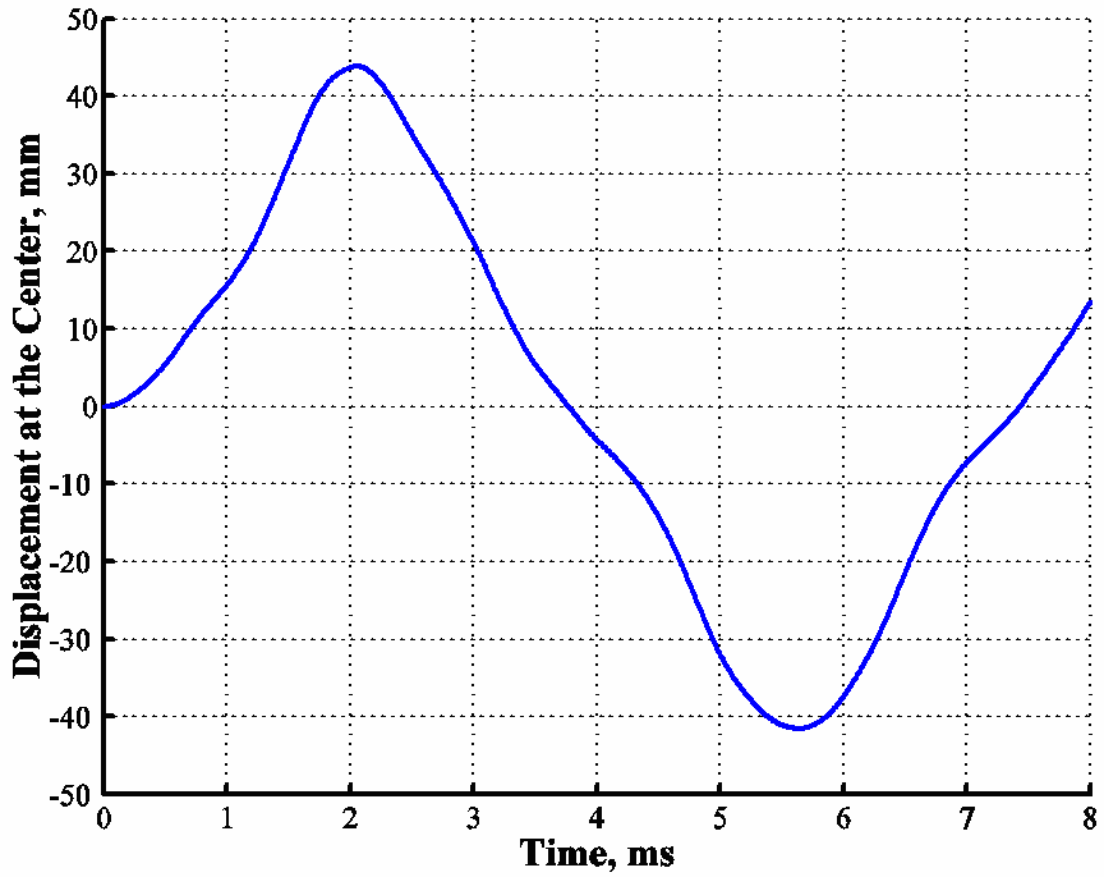
Figure 5-24: Displacement vs. time of the S2-Glass/Epoxy panel under blast wave pressure loading ($P_m = 1.065$ (MPa), $t_p = 1.3$ (msec), $\alpha = 1.7$)

@ 2.1 ms, layer 1, 0 degree   @ 2.1 ms, layer 2, 45 degree   @ 2.1 ms, layer 14, -45 degree   @ 2.1 ms, layer 15, 0 degree

@ 6.0 ms, layer 1, 0 degree   @ 6.0 ms, layer 2, 45 degree   @ 6.0 ms, layer 14, -45 degree   @ 6.0 ms, layer 15, 0 degree
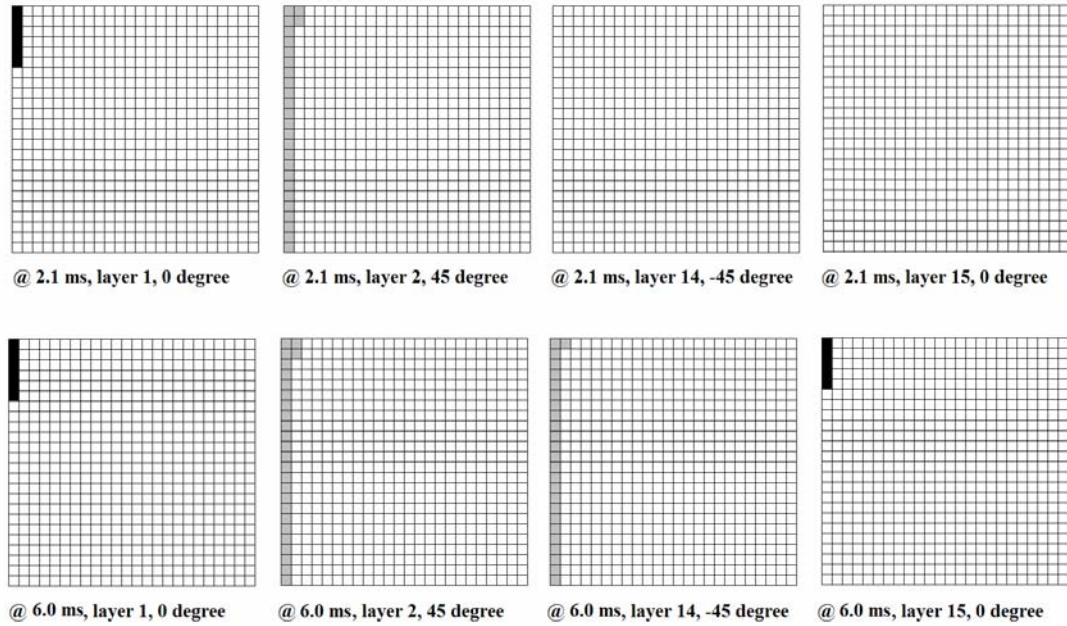
Figure 5-25: Failed regions at the top and bottom two layers of the S2-Glass/Epoxy panel near the first peak and trough
($P_m = 1.065$ (MPa), $t_p = 1.3$ (msec), $\alpha = 1.7$)
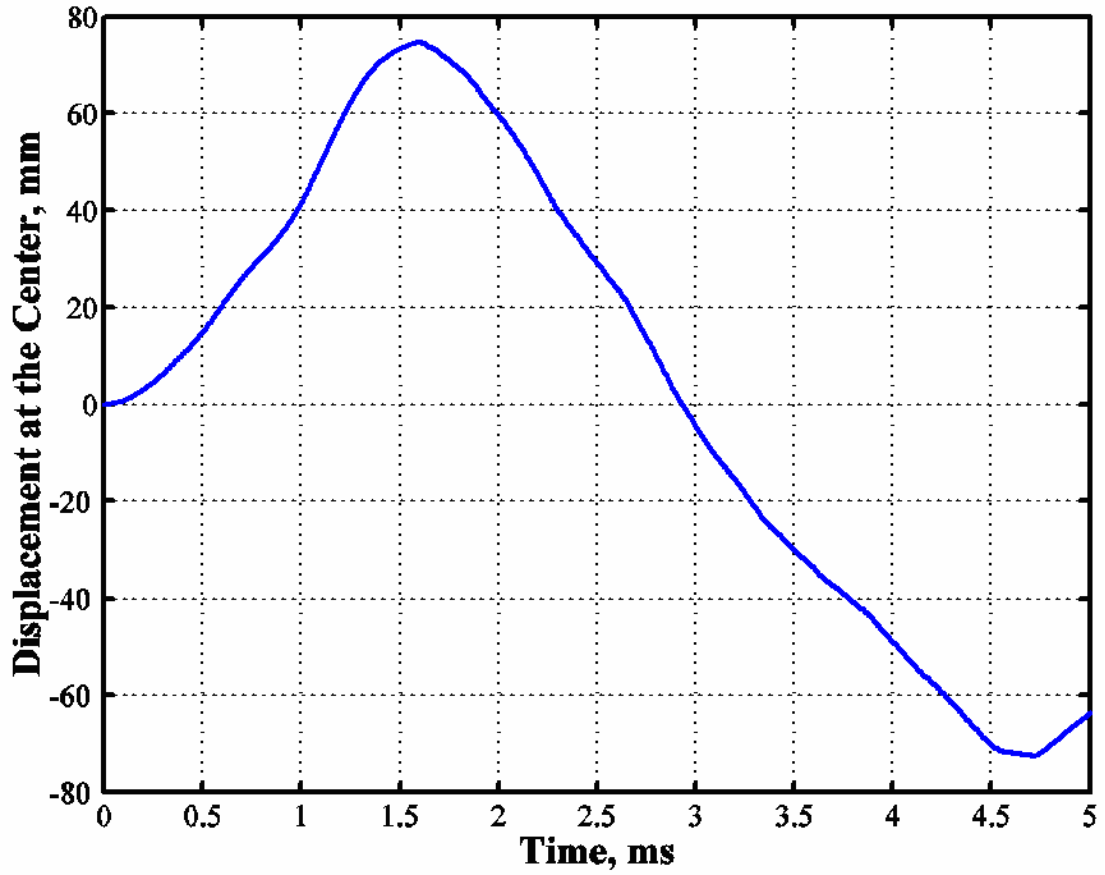
Figure 5-26: Displacement vs. time of the S2-Glass/Epoxy panel under blast wave pressure loading ($P_m = 3.1$ (MPa), $t_p = 1.2$ (msec), $\alpha = 2.15$)
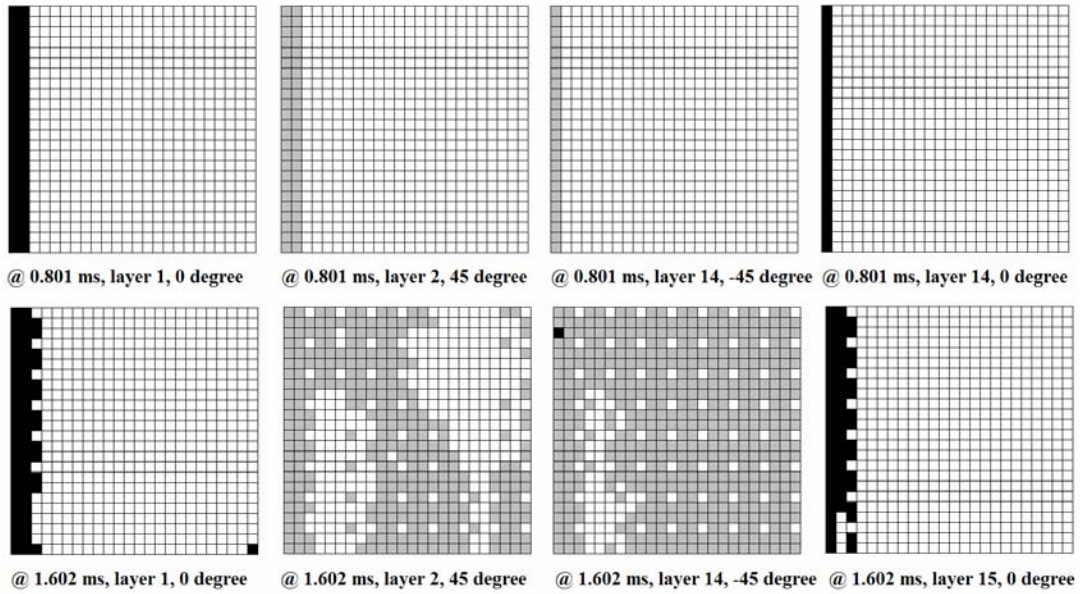
Figure 5-27: Failed regions at the top and bottom two layers of the S2-Glass/Epoxy panel near the first peak and trough
$(P_m = 3.1 \text{ (MPa)}, \; t_p = 1.2 \text{ (msec)}, \; \alpha = 2.15)$
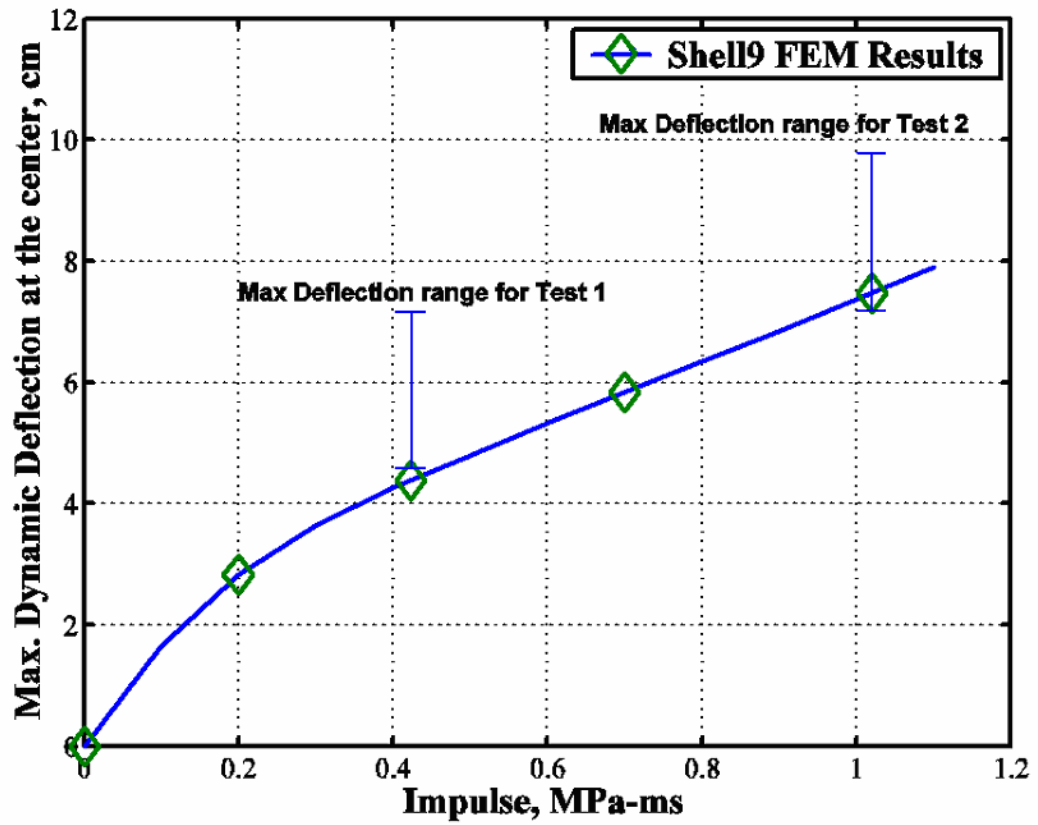
Figure 5-28: Maximum dynamic deflection at the first peak vs. impulse on the S2-Glass/Epoxy panel
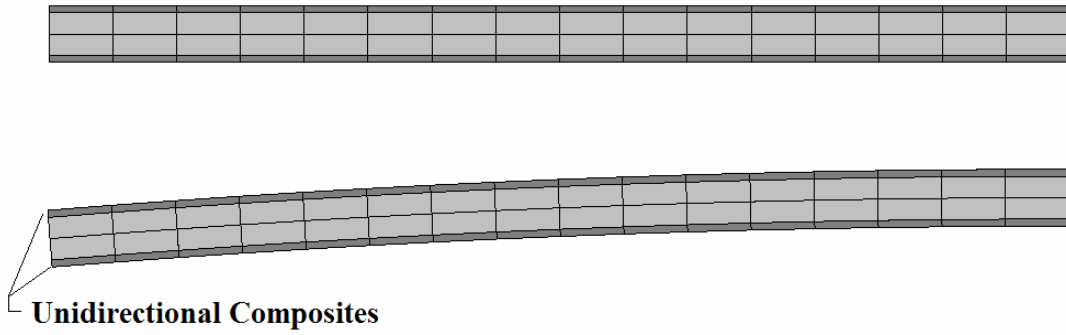
Figure 5-29: Flat and arched (h/L=0.2) Aluminum Nitride ceramic panels wrapped by unidirectional composites (Graphite/Epoxy)
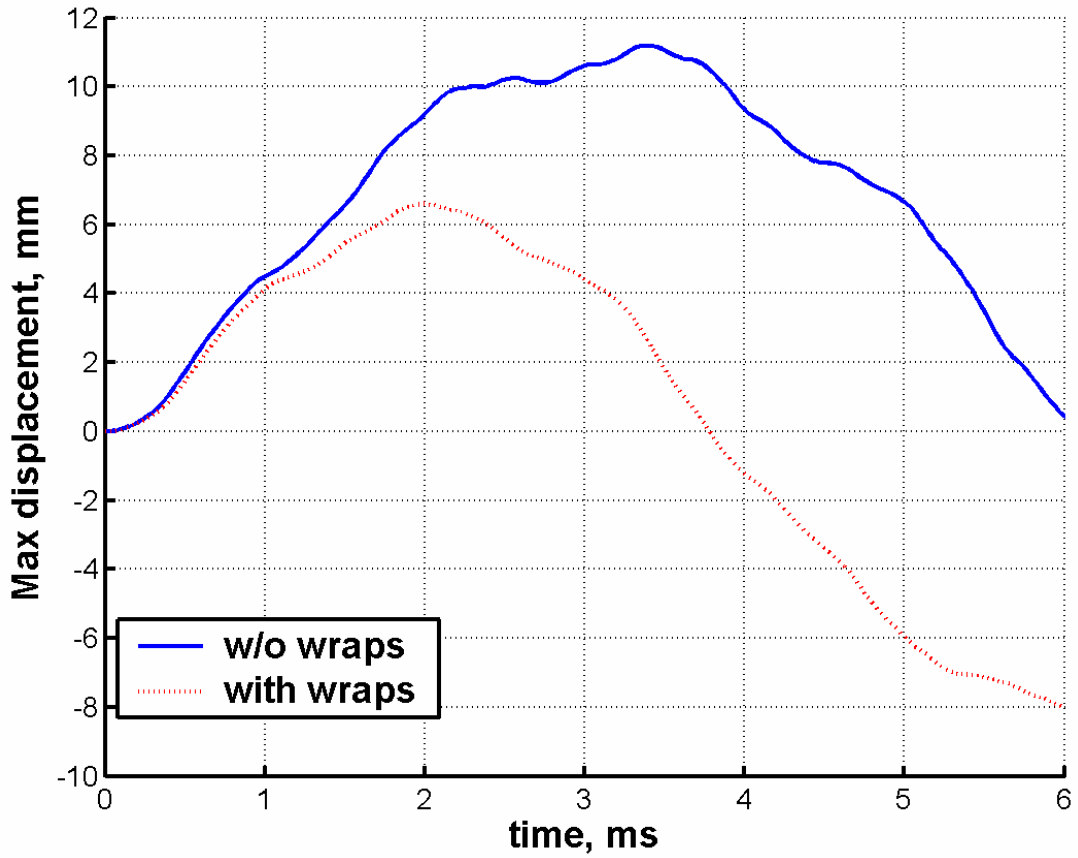
Figure 5-30: Maximum displacement at the center vs. time for the clamped flat Aluminum Nitride panels with and without wrapping, and failed region
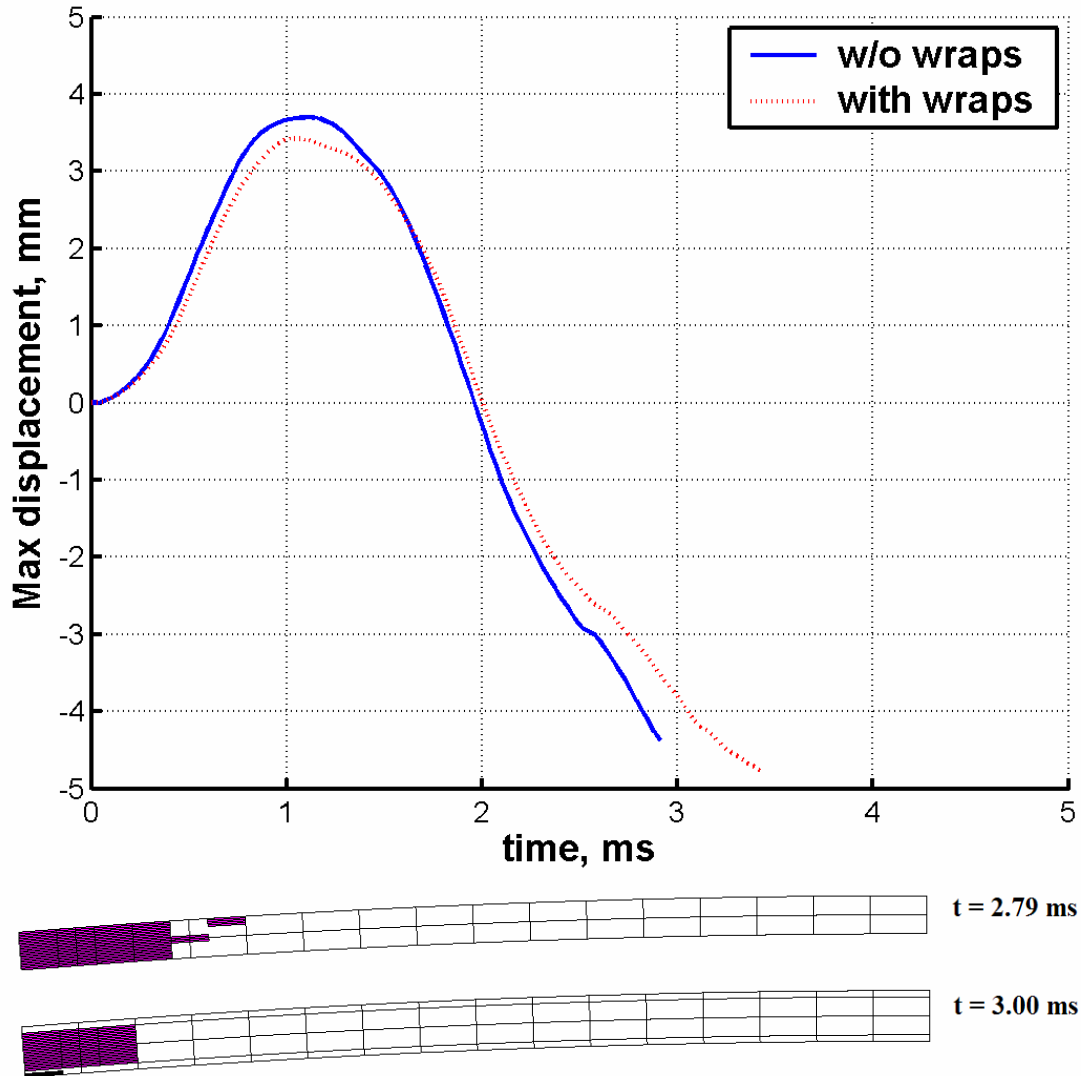
Figure 5-31: Maximum displacement at the center vs. time for the clamped arched Aluminum Nitride panels with and without wrappings, and failed region
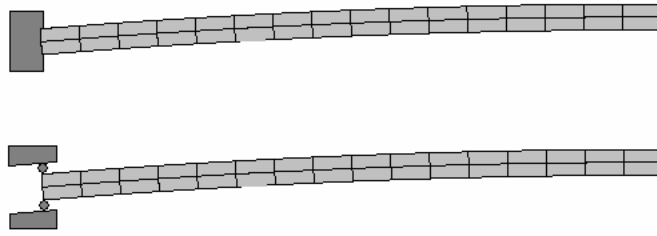
Figure 5-32: Boundary conditions with and without sliding at the edge of the arched Aluminum Nitride panels
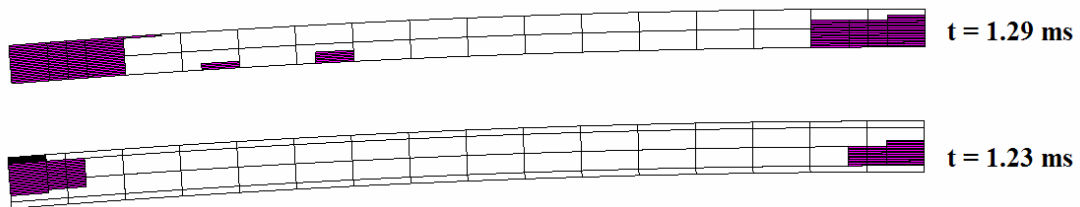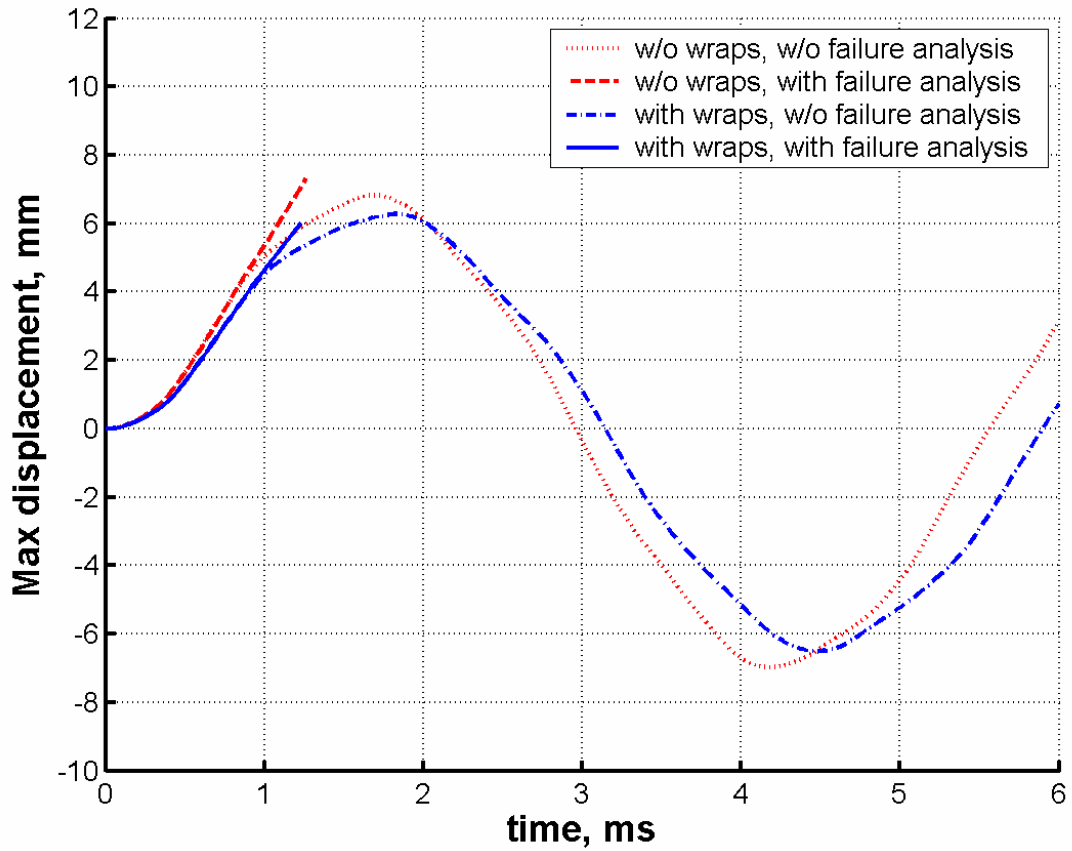
Figure 5-33: Maximum displacement at the center vs. time for the clamped arched Aluminum Nitride unwrapped and wrapped panels, and failed region
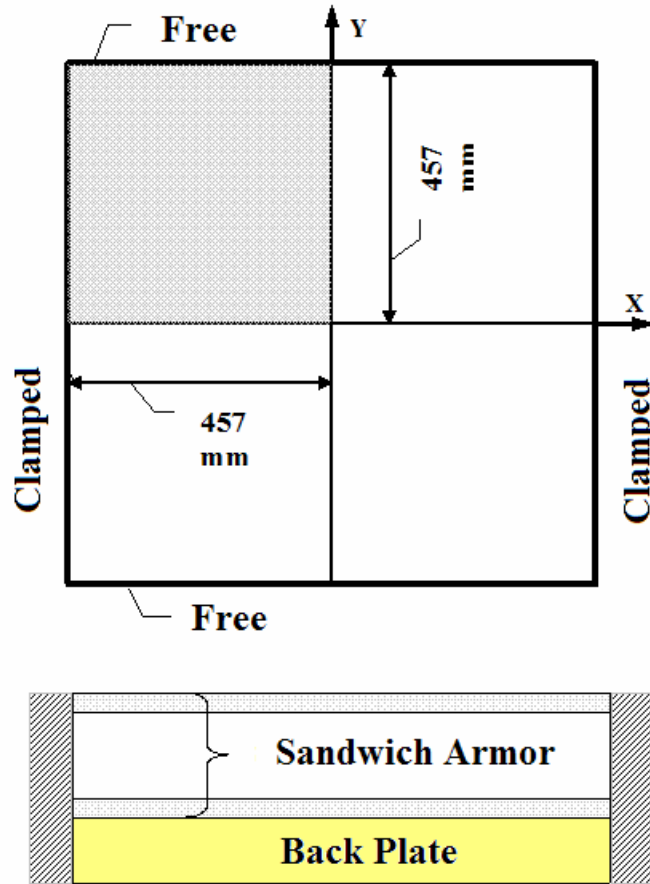
Figure 5-34: Geometry and analysis region (shaded area in the top view) of sandwich armor with a back plate, and boundary conditions
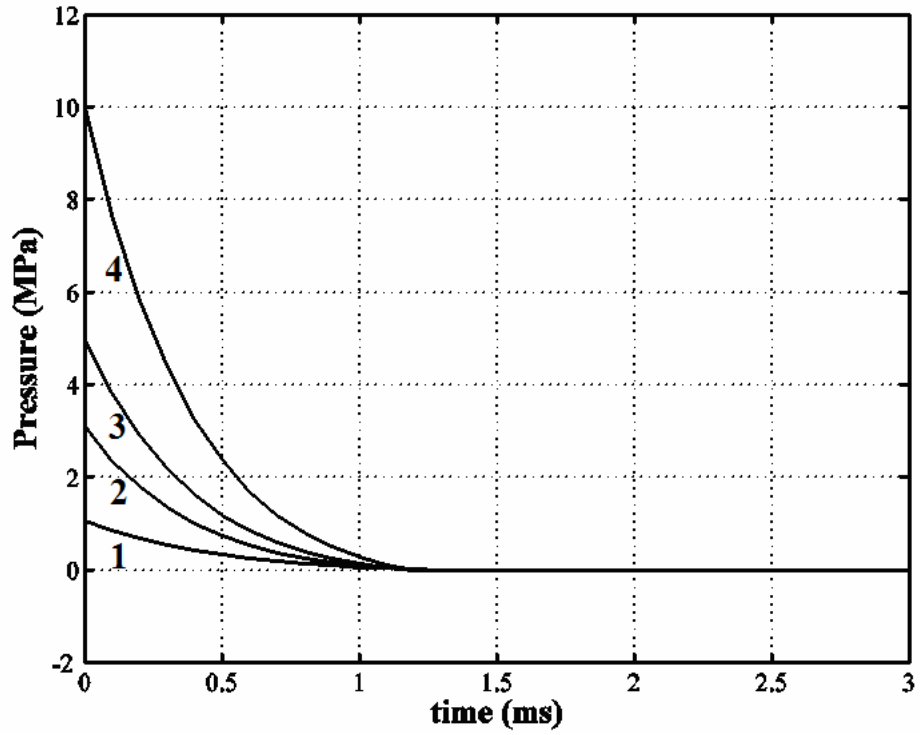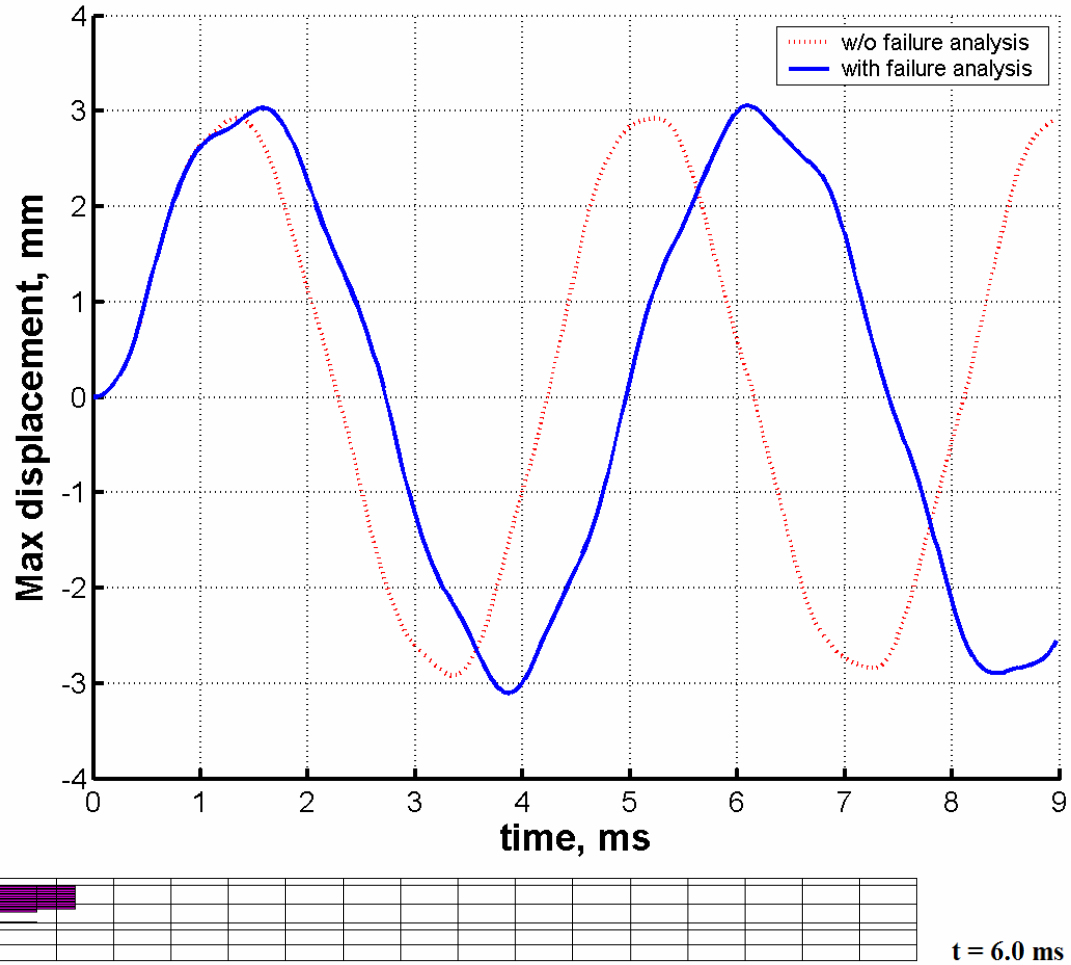
Figure 5-35: Four blast wave profiles

Figure 5-36: Max dynamic deflection at the panel center for a clamped-free panel with blast loading case I ($P_m = 1.065$ (MPa), $t_p = 0.0013$ (sec), $\alpha = 1.70$)
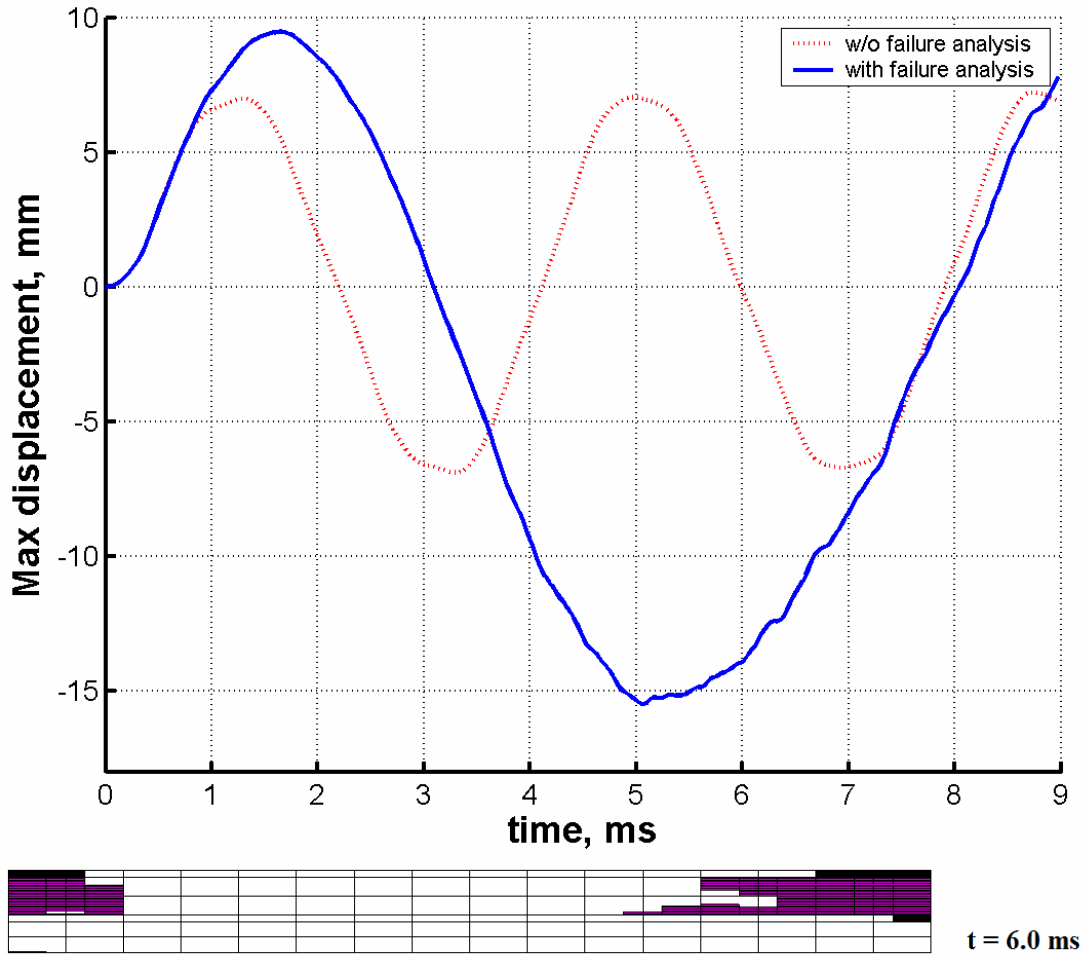
Figure 5-37: Max dynamic deflection at the panel center for a clamped-free panel with blast loading case II ($P_m = 3.1$ (MPa), $t_p = 0.0012$ (sec), $\alpha = 2.15$)
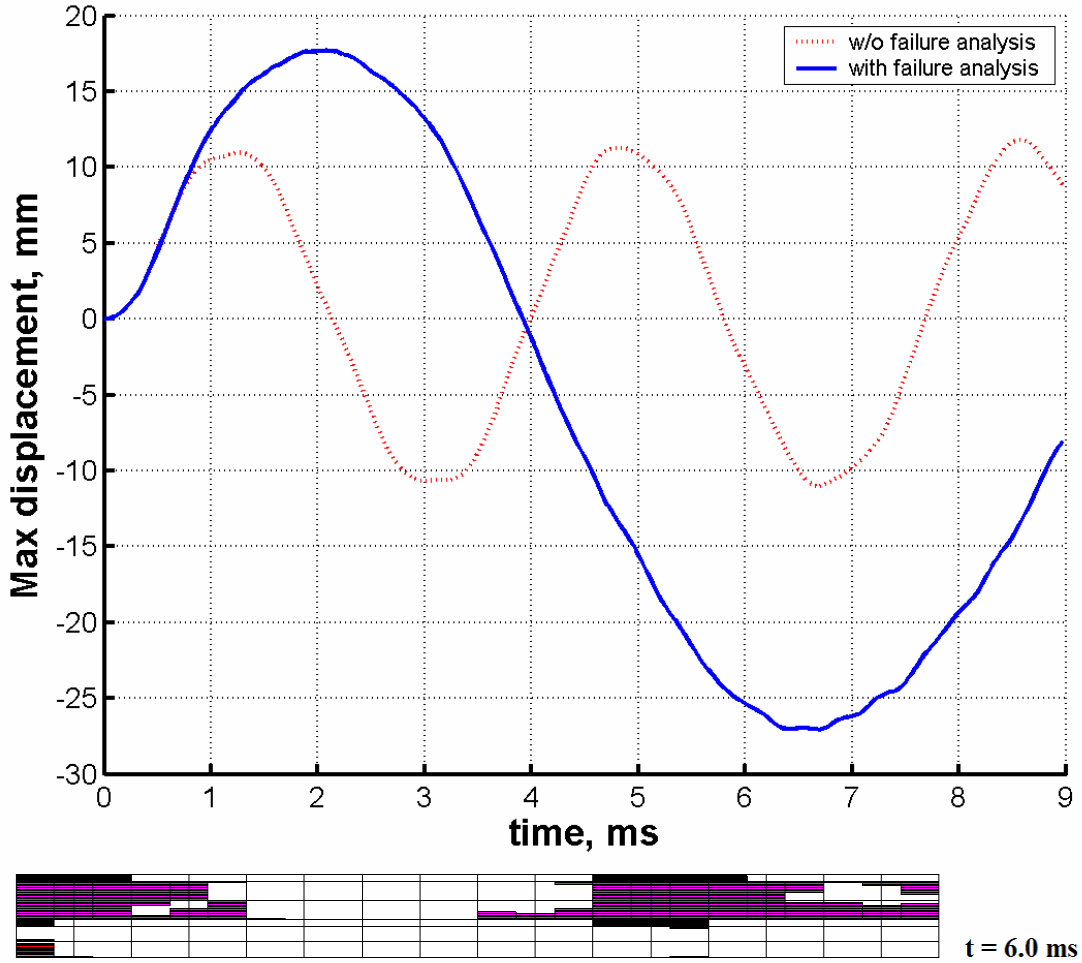
Figure 5-38: Max dynamic deflection at the panel center for a clamped-free panel with blast loading case III ($P_m = 5.0$ (MPa), $t_p = 0.0012$ (sec), $\alpha = 2.15$)
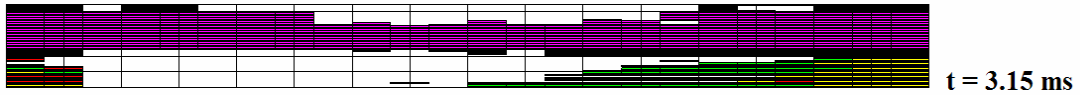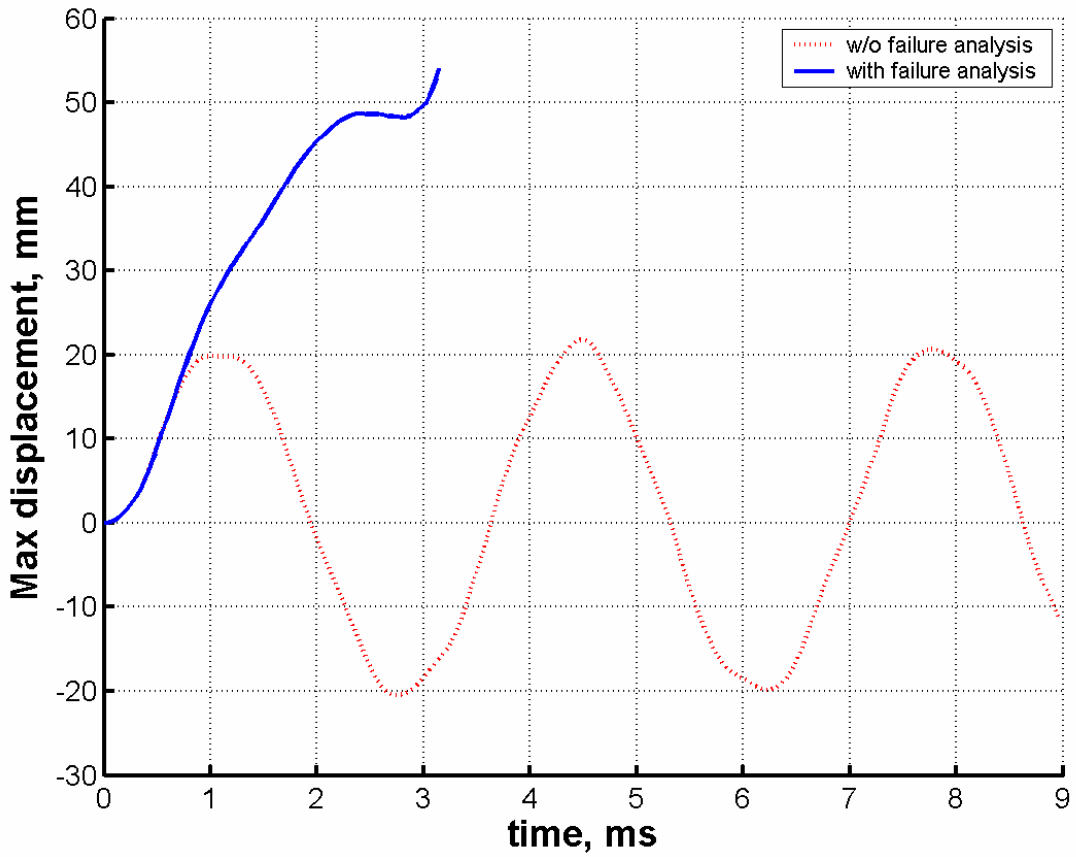
Figure 5-39: Max dynamic deflection at the panel center for a clamped-free panel with blast loading case IV ($P_m = 10.0$ (MPa), $t_p = 0.0012$ (sec), $\alpha = 2.15$)
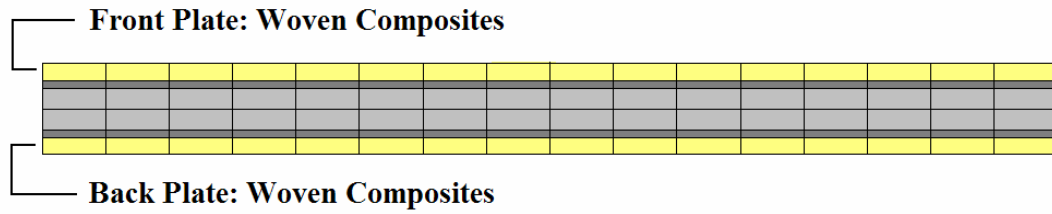
Figure 5-40: Configuration of wrapped sandwich armor with front and back woven composite plates

Figure 5-41: Max dynamic deflection at the panel center for a clamped-free (clamped at the front and back plates) panel subjected to blast loading case I ($P_m = 1.065$ (MPa), $t_p = 0.0013$ (sec), $\alpha = 1.70$)
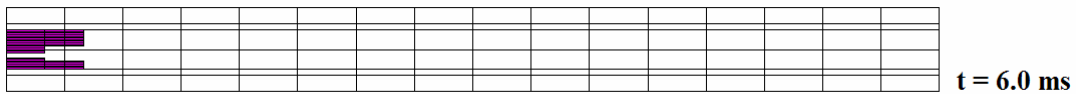
Figure 5-42: Max dynamic deflection at the panel center for a clamped-free (clamped at the front and back plates) panel subjected to blast loading case II ($P_m = 3.1$ (MPa), $t_p = 0.0012$ (sec), $\alpha = 2.15$)
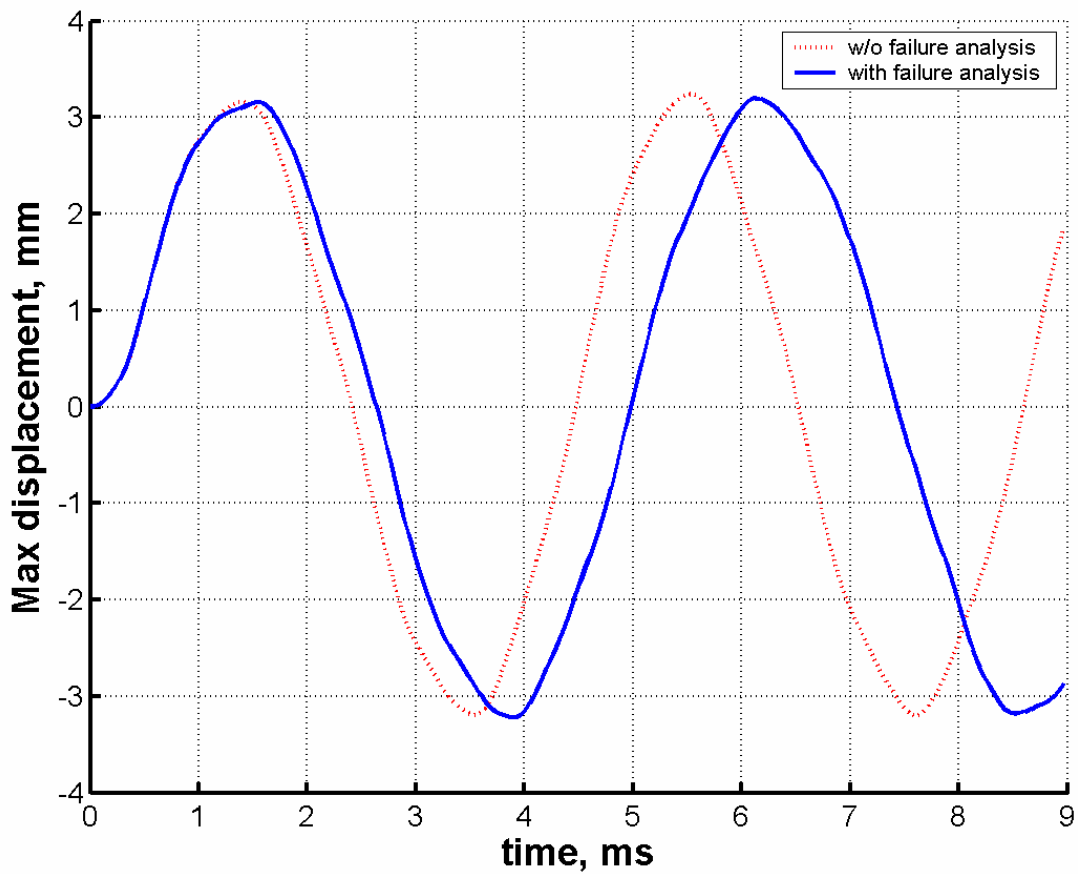
Figure 5-43: Max dynamic deflection at the panel center for a clamped-free (clamped at the front and back plates) panel subjected to blast loading case II ($P_m = 5.0$ (MPa), $t_p = 0.0012$ (sec), $\alpha = 2.15$)
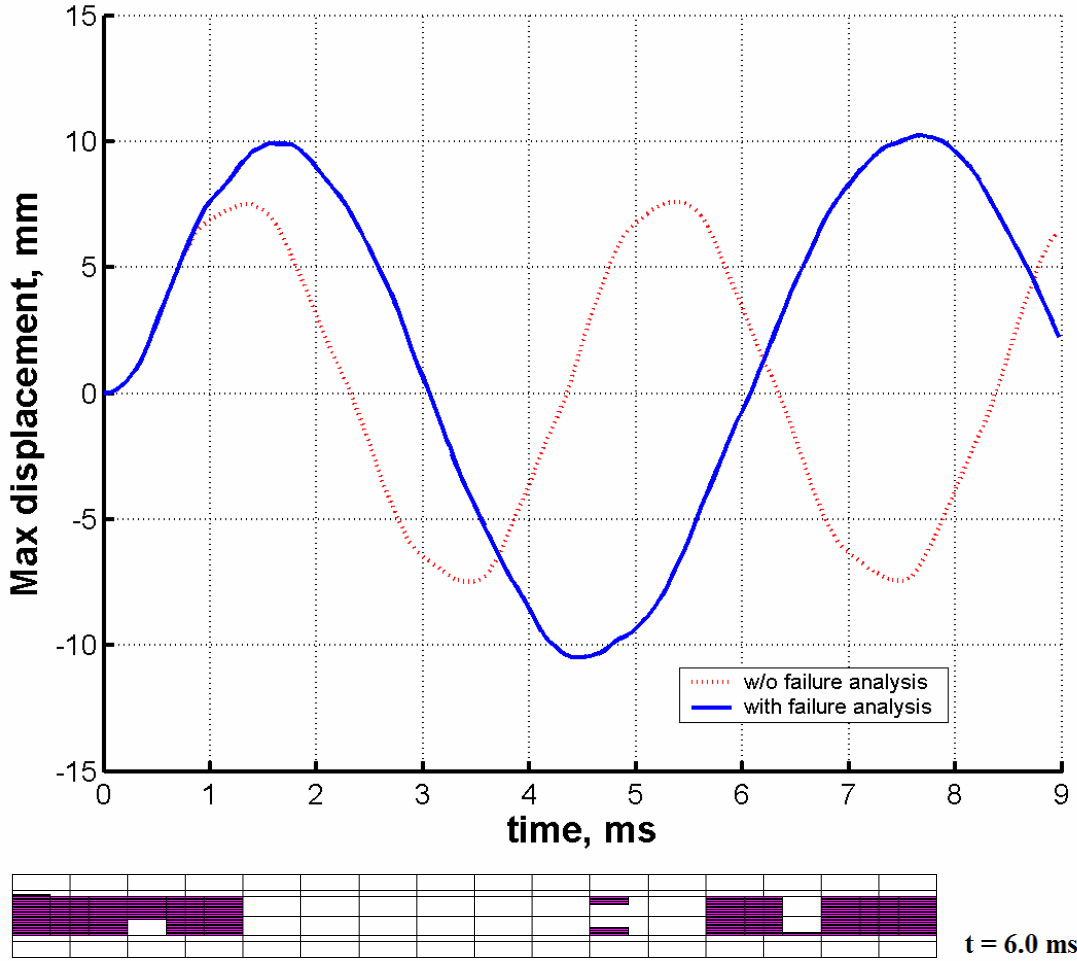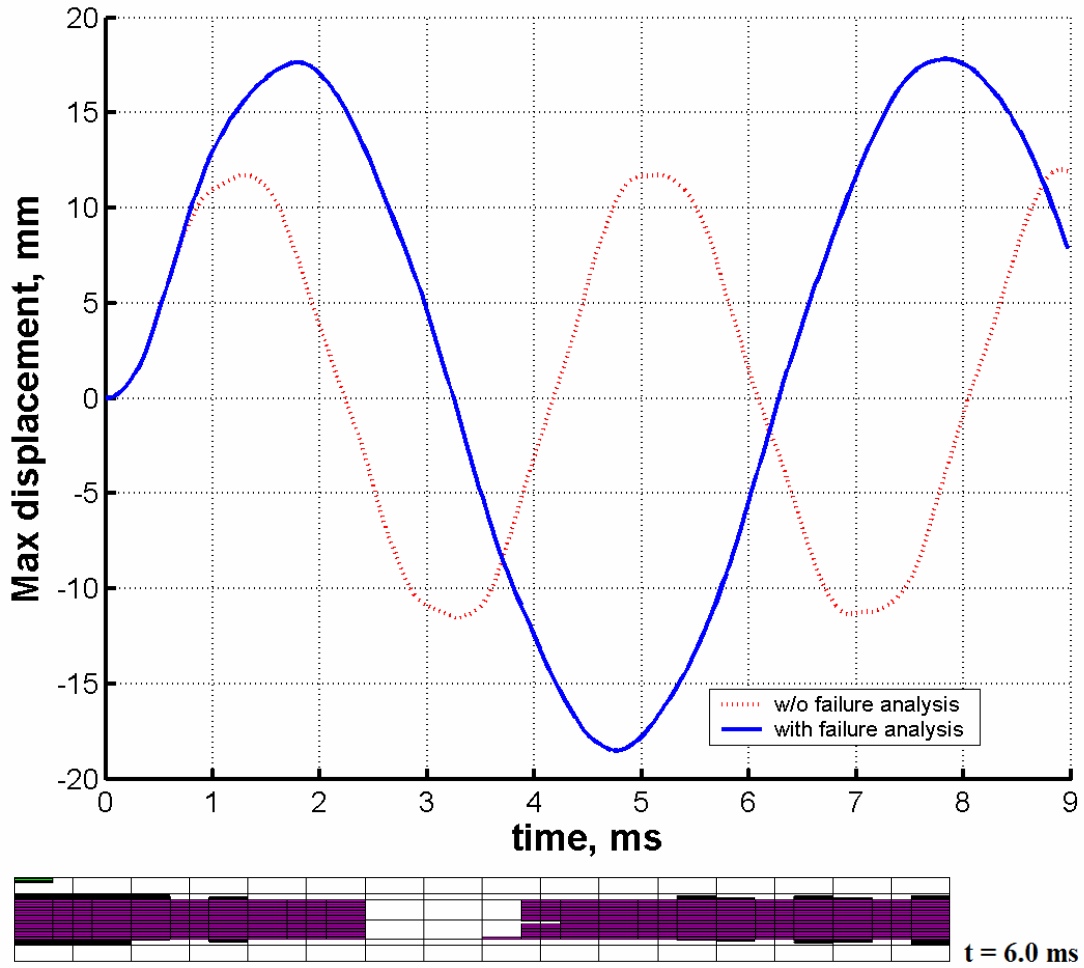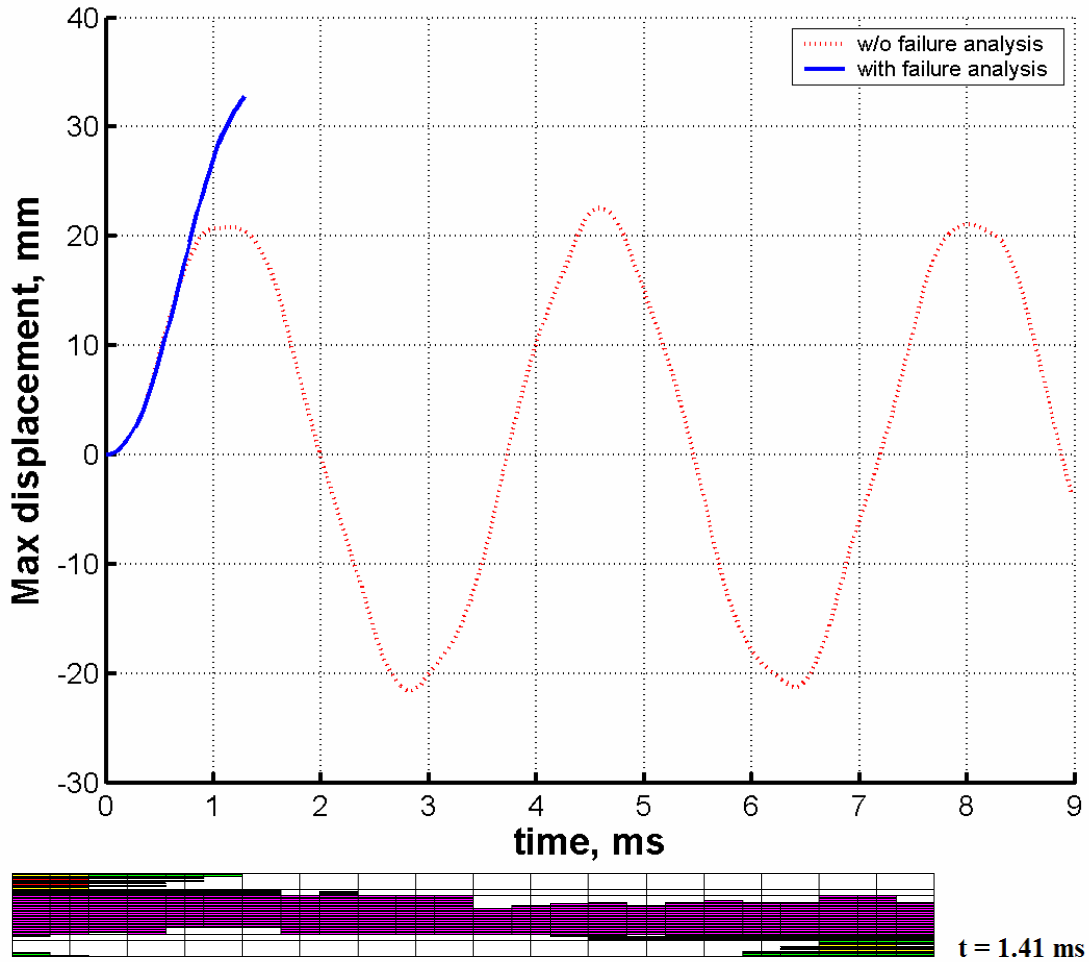
Figure 5-44: Max dynamic deflection at the panel center for a clamped-free (clamped at the front and back plates) panel subjected to blast loading case II ($P_m = 10.0$ (MPa), $t_p = 0.0012$ (sec), $\alpha = 2.15$)

Bibliography

1. L. M. Taylor, E. Chen, and J. S. Kuszmaul, "Microcrack-induced Damage Accumulation in Brittle Rock under Dynamic Loading", *Computer Methods in Appl. Mech. and Engng*, Vol. 55, 1986, pp. 301-320

2. A. M. Rajendran and J. L. Kroupa, "Impact Damage Model for Ceramic Materials", *J. Appl. Phys*, Vol. 66:8, 1989, pp. 3560-3565

3. F. L. Addessio and J. N. Johnson, "A Constitutive Model for the Dynamic Response of Brittle Materials", *J. Appl. Phys*, Vol. 67:7, 1990, pp. 3275-3286

4 A. M. Rajendran and D. J. Grove, "Modeling the Shock Response of Silicon Carbide, Boron Carbide and Titanium Diboride", *Int. J. Impact Engng*, Vol 18:6, 1996, pp. 611-631

5. A. M. Rajendran and D. J. Grove, "Computational Modeling of Shock and Impact Response of Alumina", *CMES*, Vol 3:3, 2002, pp. 367-380

6 H. D. Espinosa, "Experimental Observations and Numerical Modeling of Inelasticity in Dynamically Loaded Ceramics", *Journal of Hard Materials*, Vol 3, 1992, pp. 285-313

7 P. D. Zavattieri, P. V. Raghuram, H. D. Espinosa, "A Computational Model of Ceramic Microstructures Subjected to Multi-axial Dynamic Loading", *Journal of the Mechanics and Physics of Solids*, Vol 49, 2001, pp. 27-68

8 G. R. Johnson and T. J. Holmquist, "A Computational Constitutive Model for Brittle Materials Subjected to Large Strains, High Strain Rates, and High Pressures", *Shockwave and High-Strain-Rate Phenomena in Materials*, edited by M. A. Meyers, L.E. Murr and K. P. Staudhammer, Marcel Dekker Inc., New York, 1992, pp. 1075-1081

9 G. R. Johnson and T. J. Holmquist, "Response of Boron Carbide Subjected to Large Strains, High Strain Rates, and High Pressures", *J. Appl. Phys*, Vol. 85:12, 1999, pp. 8060-8073

10 T. J. Holmquist, D. W. Templeton and K. D. Bishnoi, "Constitutive Modeling of Aluminum Nitride for Large Strain, High-Strain Rate, and High-Pressure Applications", *Int. J. Impact Engng*, Vol. 25, 2001, pp. 211-231

11 T. J. Holmquist and G. R. Johnson, "Response of Silicon Carbide to High Velocity Impact", *J. Appl. Phys*, Vol. 91:9, 2002, pp. 5858-5866

12 E. P. Fahrenthold, "A Continuum Damage Model for Fracture of Brittle Solids under Dynamic Loading", *J. Appl. Mech*, Vol. 58, 1991, pp. 904-909

13 C. H. M. Simha, S. J. Bless and A. Bedford, "Computational Modeling of the Penetration Response of a High-Purity Ceramic", *Int. J. Impact Engng*, Vol. 27, 2002, pp. 65-86

14 C. H. Simha, *High Rate Loading of a High Purity Ceramic – One Dimensional Stress Experiments and Constitutive Modeling*, University of Texas, Ph.D. dissertation, 1998

15 A. M. Rajendran, "A Review of Ceramic Constitutive Models for Dynamic Loading", 4th Inter. Conference on Constitutive Laws for Engineering Materials: Experiment, Theory, Computation and Applications, Rensselaer Polytechnique Institute, 1999, pp. 188-191s

16 H. C. Heard and C. F. Cline, "Mechanical Behavior of Polycrystalline BeO, Al_2O_3 and AlN at High Pressure", *J. Materials Science*, Vol. 15, 1980, pp. 1889-1897

17 J. Lankford, "Compressive Strength and Microplasticity in Polycrystalline Alumina", *J. Materials Science*, Vol. 12, 1977, pp. 791-796

18 J. Lankford, "Utilization of the Split Hopkinson Pressure Bar under Hydrostatic Confining Pressure to Characterize the Compressive Behavior of Ceramics and Ceramic Composites", AMD 197, AMSE, NEW YORK, 1994, pp. 1-12

19 W. Chen, *Dynamic Failure Behavior of Ceramics under Multiaxial Compression*, California Institute of Technology, Ph.D. dissertation, 1995

20 W. Chen and G. Ravichandran, "Dynamic Compressive Failure of a Glass Ceramic under Lateral Confinement", *J. Mech. Phys. Solids,* Vol. 45, 1997, pp. 1303-1328

21 W. Chen and G. Ravichandran, "Failure Mode Transition in Ceramics under Dynamic Multiaxial Compression", *Int. J. Fracture*, Vol. 101, 2000, pp. 141-159

22 S. S. Sarva, *Dynamic Failure Mechanisms in Armor Grade Ceramics (The effect of lateral confinement and membrane restraint),* Ph.D. dissertation, University of California, 2003

23 H. Park, A Nonlinear Solid Shell Element Formulation for Analysis of Composite Panels under Blast Wave Pressure Loading, Ph.D. dissertation, University of Maryland, 2003

24 J. E. Slater, "Selection of a Blast-Resistant GRP Composite Panel Design for Naval Ship Structures", *Marine Structures*, Vol. 7, 1994, pp. 417-440

25 C. F. Yen, T. Cassin, J. Patterson and M. Triplett, "Progressive Failure Analysis of Composite Sandwich Panels under Blast Loading", *Structures under Extreme Loading Conditions,* PVP-Vol. 361, ASME, 1998, pp. 203-215

26 J. O. Hallquist, "DYNA3D Theoretical Manual for DYNA2D" Livermore Software Tech. Corp., Rev. 2, 1993

27 Meunier, M. and Shenoi, "Dynamic Analysis of Composite Sandwich Plates with Damping Modelled using High-order Shear Deformation Theory", *Composite Structures*, Vol. 54, 2001, pp. 243-254

28 Z. Hashin, "Failure Criteria for Unidirectional Fiber Composites", *J. Appl. Mech.*, Vol. 47, 1980, pp. 329-334

29 A. Rotem and Z. Hashin, "Failure Modes of Angle Ply Laminates", *J. Composite Materials*, Vol. 9, 1975, pp. 191-206

30 F. Chang and K. Chang, "A Progressive Damage Model for Laminated Composites Containing Stress Concentrations", *J. Composite Materials*, Vol. 21, 1987, pp. 834-855

31 F. Chang and L. B. Lessard, "Damage Tolerance of Laminated Composites Containing an Open Hole and Subjected to Compressive Loadings: Part I – Analysis", *J. Composite Materials*, Vol. 25, 1991, pp. 2-41

32 K. Chang, S. Liu and F. Chang, "Damage Tolerance of Laminated Composites Containing an Open Hole and Subjected to Tensile Loadings", *J. Composite Materials*, Vol. 25, 1991, pp. 274-301

33 Z. Hashin, "Analysis of Stiffness Reduction of Cracked Cross-Ply Laminates", *Engng Fracture Mech.*, Vol. 25:5-6, 1986, pp. 771-778

34 G. S. Padhi, R. A. Shenoi, S. S. J. Moy and G. L. Hawkins, "Progressive Failure and Ultimate Collapse of Laminated Composite Plates in Bending", *Composite Structures*, Vol. 40:3-4, 1998, pp. 277-291

35 G. E. Andreev, *Brittle Failure of Rock Materials (Test Results and Constitutive Models)*, A. A. Balkema, 1995

36 W. F. Chen and D. J. Han, *Plasticity for Structural Engineers,* GAU LIH, 1995

37 G. S Desai and H. J. Siriwardane, *Constitutive Laws for Engineering Materials with Emphasis on Geologic Materials*, Prentice-Hall, 1984

38 D. E. Grady, "The Spall Strength of Condensed Matter", *Journal of the Mechanics and Physics of Solids*, Vol. 36, 1988, pp. 353-383

39 Z. Rosenberg, N. S. Brar and S. J. Bless, "Dynamic High-Pressure Properties of AlN Ceramic as Determined by Flyer Plate Impact", *J. Appl. Phys.*, Vol70, 1991, pp. 167-169

40 W. Pariseau, "Plasticity Theory for Anisotropic Rocks and Soils", *Proc. 10th Symp Rock Mech.*, Austin, 1968, pp. 267-295

41 R. Hill, *The Mathematical Theory of Plasticity*, Clarendon Press, Oxford, 1950

42 K. M. Reinicke and T. D. Ralston, "Plastic Limit Analysis with an Anisotropic Parabolic Yield Function", I*nt. J. Rock Mech. Min. Sci. & Geomech Abstr*, Vol. 14, 1977, pp. 147-154

43 S. T. S. Al-Hassani and A. S. Kaddour, "Strain Rate Effects on GRP, KRP and CFRP Composite Laminates", *Key Engng Materials*, Vol. 141-143, 1998, pp. 427-452

44 C. T. Sun and J. L. Chen, "A Simple Flow Rule for Characterizing Nonlinear Behavior of Fiber Composites", *J. Composite Materials*, Vol. 23, 1989, pp. 1009-1020

45 J. J. Rhiu and S. W. Lee, "A Nine-node Finite Element for Analysis of Geometrically Nonlinear Shells", *Int. J. Numer Methods Eng.*, Vol. 26, 1988, pp. 1945-1962

46 Y. H. Kim and S. W. Lee, "A Solid Element Formulation for Large Deflection Analysis of Composite Shell Structures", *Computers and Structures*, Vol. 30, 1988, pp. 269-274

47 S. Lee and T. Pian, "Improvement of Plate and Shell Finite Element by mixed Formulations", *AIAA Journal*, Vol. 16, 1978, pp. 29-34

48 H. C. Park and S. W. Lee, "A Local Coordinate System for Assumed Strain Shell Element Formulation", *Computational Mechanics*, Vol. 15, No. 5, 1995, pp. 473-484

49 C. H. Yeom and S. W. Lee, "An Assumed Strain Element Model for Large Deflection Composite Shells", *Int. J. Numer Methods Eng.*, Vol. 28, 1989, pp. 1749-1768

50 C. Cho, "An improved assumed strain shell element formulation including bubble function displacements", Ph.D. dissertation, Department of Aerospace Engineering, University of Maryland, 1996

51 H. Bin, *Postbuckling behavior of soft-core sandwich plates with composite facesheets*, M.S. thesis, University of Maryland, 1998

52 J. A. Scott, *The Design of a Parallel Frontal Solver*, Rutherford Technical Report, RAL-TR-1999-075, 1999

53 O. Orringer, *Frontal Analysis Program-User's Guide*, Massachusetts Institute of Technology, 1974

54 V. K. Decyk, "Benchmark Timings with Partcle Plasma Simulation Code", *Supercomputer*, Vol. V-5, 1988, pp. 27-33

55 H. S. Turkmen and Z. Mecitoglu, "Nonlinear Structural Response of Laminated Plates Subjected to Blast Loading", *AIAA J.*, Vol. 37:12, 1999, pp. 1639-1647

56 L. Librescu and A. Nosier, "Response of Laminated Composite Flat Panels to Sonic Boom and Explosive Blast Loadings", *AIAA J.,* Vol. 28:2, 1990, pp. 345-352